Inverse Partial Fluorescence Yield Spectroscopy

by

Andrew Achkar

A thesis
presented to the University of Waterloo
in fulfillment of the
thesis requirement for the degree of
Master of Science
in
Physics

Waterloo, Ontario, Canada, 2011

© Andrew Achkar 2011

I hereby declare that I am the sole author of this thesis. This is a true copy of the thesis, including any required final revisions, as accepted by my examiners.

I understand that my thesis may be made electronically available to the public.

Abstract

X-ray absorption spectroscopy (XAS) is a powerful probe of electronic and spatial structure that has been at the heart of many advances in physics, biology, chemistry, engineering and the earth sciences. Unfortunately, the existing experimental techniques are subject to fundamental limitations that complicate the interpretation of x-ray absorption spectra in many important cases. These limitations have motivated an effort to develop an alternative measure of the absorption cross-section that is not subject to the same set of limitations. In this thesis, a technique known as inverse partial fluorescence yield (IPFY) is described which addresses this problem. IPFY differs from existing approaches in a significant way — by using an energy-discriminating photon detector, one gains access to fluorescence information from both resonant and non-resonant x-ray emission processes.

We will show that the non-resonant emission is fundamentally related to the total absorption cross-section of a material through an inverse relation. This will be proven by extension of the general theory of fluorescence yield for the case of a thick, homogeneous specimen. We will also demonstrate the utility of IPFY with measurements of NiO, $NdGaO_3$, $La_{1.475}Nd_{0.4}Sr_{0.125}CuO_4$, and stainless steel 304 at soft and intermediate x-ray energies. These experiments will highlight some essential features of IPFY spectroscopy and demonstrate how it can be an invaluable tool when the other experimental techniques fail to provide reliable spectra. We will also demonstrate how one can exploit the geometry dependence of IPFY to quantitatively determine the composition of a sample and the total x-ray absorption coefficient. Additionally, we will consider the special cases of multilayers and powder specimens, where the theory of fluorescence yield requires approximations and is not as well-behaved as in thick, homogenous specimens.

Ultimately, these experiments and theoretical developments will be used to support the claim that IPFY is a bulk sensitive measure of the total x-ray absorption coefficient. Moreover, we will show that IPFY is not affected by saturation effects, is insensitive to surface contamination layers and provides reliable spectra even for strongly insulating materials. These properties make IPFY a suitable spectroscopic technique for studying XAS in a wide range of materials.

Acknowledgements

First and foremost, I must acknowledge the tremendous support and guidance of my supervisor David Hawthorn. Without his dedicated efforts, this work would not have been possible. I must also acknowledge the continual efforts of Tom Regier towards advancing IPFY spectroscopy. His work on designing and building a new endstation optimized for IPFY spectroscopy is a testament to his dedication. I would also like to acknowledge Hiroki Wadati for valuable discussions and for his interest in demonstrating IPFY as a useful form of spectroscopy. My collaborators at Cornell, Kyle Shen, Eric Monkman and Daniel Shai, have also been very supportive and have helped me challenge the conventional wisdom about FY-based spectroscopy.

I cannot express how much I appreciate the love and support that my parents have dedicated towards enabling me to follow any path of my choosing. Without their tireless efforts, I would never be where I am now. The same appreciation extends to my sister who, despite constantly interpreting my research using absurd references to the sharks in the movie Austin Powers: International Man of Mystery, remains in her heart extremely supportive and always engaged. She makes me laugh and always helps me to relax when I am overly stressed. The support I get from my cousins, aunts and uncles, no matter what continent they find they themselves on, is always astounding. To my two grandmothers who have experienced more than I can imagine, thank you for your patience and your unwavering love as I try repeatedly to teach you about the composition of matter.

I must also acknowledge Halle's outstanding patience, spirit and dedication to supporting me throughout the writing of this thesis. Her encouraging sayings and lively music kept my motivation levels high, her guidance for all things artistic was indispensable and the delectable meals she prepared were always the highlight of my day.

Finally, I would like to thank my friends, near and far, who have each encouraged me to do my best in their own ways and taught me life lessons that will stay with me for a long time.

Dedication

I dedicate this thesis to my parents Marc and Nada.
Your unwavering love and support has enabled me to follow my dreams.

Table of Contents

List of Tables xv

List of Figures xvii

List of Abbreviations xix

List of Symbols xxi

1 Introduction **1**

1.1 Overview 1

1.2 X-ray absorption 4

1.2.1 Attenuation 4

1.2.2 Transition probability 5

1.2.3 Spectroscopic notation 6

1.2.4 X-ray absorption spectra 8

1.3 Importance of $\mu_{\text{tot}}(E)$ 10

2 Experimental Techniques **13**

2.1 Transmission 13

2.2 Fluorescence yield 14

2.3 Electron yield 16

2.4 Experimental limitations 18

2.4.1 Thickness and pinhole effects 18
2.4.2 Saturation effects 19
2.4.2.1 Electron yield saturation 19
2.4.2.2 Fluorescence yield saturation 20
2.4.3 Surface effects 24

3 Principles of Inverse Partial Fluorescence Yield 27
3.1 Partial fluorescence yield 27
3.1.1 Resonant PFY 27
3.1.2 Non-resonant PFY 29
3.2 Inverse partial fluorescence yield 29
3.2.1 Approximations 30
3.2.2 Geometry dependence 30
3.3 Implications 32

4 Experimental Demonstrations of IPFY 33
4.1 Measurement details 33
4.2 IPFY spectroscopy 34
4.2.1 NiO 35
4.2.1.1 X-ray fluorescence and PFY 35
4.2.1.2 IPFY in the XANES region 37
4.2.1.3 Geometry effects in PFY and IPFY 38
4.2.1.4 Verifying the validity of our approximations 41
4.2.2 $NdGaO_3$ 44
4.2.2.1 X-ray fluorescence and PFY 44
4.2.2.2 Correction for the energy dependence of $S_{j,k}(E_i)$ in IPFY 45
4.2.2.3 The XANES region of $NdGaO_3$: charging and saturation effects 48

4.3 Determining sample stoichiometry 51
4.3.1 Principles 51
4.3.2 Demonstration with $NdGaO_3$ IPFY data 52
4.4 Current experimental limitations 55
4.5 IPFY of $La_{1.475}Nd_{0.4}Sr_{0.125}CuO_4$ 57
4.6 IPFY of stainless steel for $E > 6.5$ keV 60
4.6.1 Measurement details 60
4.6.2 Results and discussion 61

5 Special Cases **65**
5.1 Multilayers 65
5.1.1 The two layer problem 67
5.1.1.1 Limit 1: thin top layer 68
5.1.1.2 Limit 2: Thick top layer 69
5.1.1.3 Top layer of intermediate thickness 69
5.1.1.4 Extending the two layer problem to more layers 71
5.2 Powder specimens 71

6 Conclusions **77**
6.1 Summary of results 78
6.1.1 Theoretical results 78
6.1.2 Experimental demonstrations 80
6.2 Future work 81

APPENDICES **83**

A Derivation of α, β and $\frac{\sin\alpha}{\sin\beta}$ **85**
A.1 Derivation 85
A.2 Uncertainties 88

References **89**

List of Tables

4.1 Experimental angles α, β and $\frac{\sin\alpha}{\sin\beta}$ 40
4.2 Characteristic x-ray emission lines for $NdGaO_3$ 45
4.3 Characteristic x-ray emission lines for SS304 62

List of Figures

1.1 Attenuation of light 5
1.2 Energy levels of core electrons 7
1.3 X-ray absorption mechanisms 9

2.1 Transmission geometry 13
2.2 Fluorescence yield geometry 15
2.3 Electron emission processes 16
2.4 Saturation effects in electron yield 19
2.5 Saturation effects in fluorescence yield 21
2.6 FY saturation effect calculation 22

4.1 SGM optical elements 34
4.2 NiO XRF and XES 36
4.3 NiO PFY, IPFY, and TEY 37
4.4 NiO PFY and IPFY with various geometries 39
4.5 NiO IPFY correction for geometry 41
4.6 Energy dependence of fit parameter b 43
4.7 XRF and XES of $NdGaO_3$ 46
4.8 IPFY analysis of $NdGaO_3$ 47
4.9 IPFY compared to NIST calculation for $NdGaO_3$ 48
4.10 Charging effect in $NdGaO_3$ 49

4.11 PFY and IPFY of $NdGaO_3$ at the Nd $M_{5,4}$ edge 51
4.12 Determination of stoichiometry with $NdGaO_3$ IPFY data 53
4.13 XRF of $La_{1.475}Nd_{0.4}Sr_{0.125}CuO_4$ 57
4.14 O K PFY of $La_{1.475}Nd_{0.4}Sr_{0.125}CuO_4$ 58
4.15 IPFY of $La_{1.475}Nd_{0.4}Sr_{0.125}CuO_4$ 59
4.16 XRF of SS304 61
4.17 IPFY in SS304 62

5.1 Multilayer geometry 66
5.2 Powder specimen geometry 73

A.1 Experimental geometry for derivation 86

List of Abbreviations

CLS	Canadian Light Source
CXRO	Center for X-ray Optics
EM	Electromagnetic
EXAFS	Extended x-ray absorption fine structure
EY	Electron yield
FY	Fluorescence yield
IPFY	Inverse partial fluorescence yield
MCP	Multichannel plate
NIST	National Institute of Standards and Technology
PFY	Partial fluorescence yield
SDD	Silicon drift detector
SGM	Spherical grating monochromator
SXRMB	Soft X-ray Microcharacterization Beamline
SSA	Solid sample analysis
TEY	Total electron yield
TFY	Total fluorescence yield
XAS	X-ray absorption spectroscopy
XAFS	X-ray absorption fine structure
XANES	X-ray absorption near edge structure
XES	X-ray emission spectrum
XLD	X-ray linear dichroism
XMCD	X-ray magnetic circular dichroism
XMLD	X-ray magnetic linear dichroism
XPS	X-ray photoemission spectroscopy
XRD	X-ray diffraction

List of Symbols

Symbol	Physical quantity
c	Speed of light in vacuum
e	Electron charge
m_e	Electron mass
r_e	Classical electron radius
$h, \hbar$	Planck constant, Reduced Planck constant
E, E_i, E_f	Photon energy, Incident photon energy, Fluorescence photon energy
ν	Photon frequency
$I, \mathit{\Phi}_0$	Photon intensity, Incident photon flux
μ	Linear x-ray absorption coefficient
σ	X-ray absorption cross-section
T_{if}	Transition probability from state $\|i\rangle$ to state $\|f\rangle$
M_{if}	Transition matrix element
$\epsilon_{i,f}$	Initial/final state energies
$\mathcal{H}_{\text{int}}$	Interaction Hamiltonian
$\rho(\epsilon_f)$	Density of states at the final state energy
E_{F}, E_v	Fermi energy, Vacuum level
n, ℓ	Principal quantum number, Azimuthal quantum number
s, m_s	Spin quantum number, Spin projection quantum number
j	Total angular momentum quantum number
$f(E)$	Complex atomic form factor
$n(E)$	Complex index of refraction
$\eta(E_f), \Omega$	Detector efficiency, Detector solid angle
$\omega(E_i, E_f)$	Fluorescence probability
α, α'	Angle of incidence measured from sample surface/norm
β, β'	Detection angle measured from sample surface/norm
λ_e	Electron escape depth
λ_x	X-ray penetration depth

Chapter 1

Introduction

1.1 Overview

The 20th century has seen tremendous advances in the study of condensed matter due to Röntgen's remarkable discovery of x-rays.[1] Between 1903 and 1915, characteristic x-rays were observed by Barkla, x-ray diffraction was discovered by von Laue, the first x-ray spectrometer was built by Bragg (father and son) and the characteristic x-ray energies were shown to correspond to atomic numbers by Moseley.[2, 3, 4, 5, 6] Nearly simultaneously, Niels Bohr formed his model for the structure of the atom which has revolutionized our fundamental understanding of matter.[7, 8] The early work of these pioneers has developed into rich avenues of research that rely on such techniques as **x-ray photoemission spectroscopy** (XPS) and **x-ray diffraction** (XRD).[9, 10] One important field born from these efforts and the work of Maurice de Broglie is that of **x-ray absorption spectroscopy** (XAS).[11]

Matter absorbs x-rays with a probability that depends on the photon energy $E = h\nu$ and on the electronic configuration of the atoms being investigated.[6, 12, 13, 14] For free atoms, sharp discontinuities in the absorption probability occur at energies corresponding to the excitation energies of inner-shell electrons. These discontinuities are referred to as **edge steps**. Edge steps occur due to an increase in the atomic cross-section of the atom when the photon energy is increased above the transition energies of core electrons.[15, 16, 6] When atoms are instead placed in a lattice, complex absorption features appear both near and far above absorption edges.[17] These features are now understood to occur due to multi-body interactions of electrons with nearby atoms.[14] Well above an absorption edge, XAS spectra of solids contain oscillations that arise from quantum interference effects of emitted

photoelectrons creating multiple scattering waves that interfere and modify the absorption probability matrix of the absorbing atom.[18, 19, 20] This spectral region is now referred to as the **extended x-ray absorption fine structure** (EXAFS). In the **x-ray absorption near edge structure** (XANES), the absorption is instead dominated by strong scattering and local atomic resonances which provide direct information about the oxidation state and local bonding environment of the absorbing atom.

EXAFS and XANES measurements, collectively referred to as the **x-ray absorption fine structure** (XAFS), or simply XAS, are now commonly used to study the structural and electronic properties of materials across many disciplines of the natural sciences. With XAS, the photon energy can be tuned to energies corresponding to electron transitions between an unoccupied state and an inner-shell level for most electronic configurations, providing *element-specific* control during the measurement. In addition, a Fourier transform analysis of the EXAFS is a useful measure of the distance between the central atom and its nearest neighbours.[18, 19]

Before synchrotron sources of light were available, x-ray spectroscopy was performed using x-ray tubes in small laboratories. X-ray tubes operate on the principle that electrons are accelerated and collide with a target material.[12, 21] Through a series of inelastic scattering processes, the electrons are slowed down and a broad spectrum of x-rays is emitted from the target. Additionally, core-holes can be created by the incident electrons and result in the emission of characteristic x-rays. Hence, the energy spectrum made by x-ray tubes is typically broad with a few peaks corresponding to these characteristic x-rays.

The utility of such a source of x-rays to spectroscopy is rather limited. Firstly, the photon flux achievable with such tubes is at best 10^{10} photons per second. Secondly, while it is possible to monochromate the x-rays using crystals or by the application of various filters for spectroscopic purposes, such experiments are painstakingly long to perform. Synchrotron light can achieve nearly 10^9 times more flux than light from x-ray tubes.[14] Combined with major advances in x-ray optics and a high level of motorized parts at synchrotron beamlines, XAS measurements that would have taken months to collect in a lab can now be performed in a matter of minutes. As a result, synchrotron-based XAS has propelled the field of materials science forward in an unprecedented way over the past few decades. Biologists, chemists, earth scientists, engineers and condensed matter physicists have all reaped the benefits of being able to study the XAFS of novel materials with synchrotron radiation.

Generally, XAS spectra can be measured in three ways: transmission, electron yield (EY) and fluorescence yield (FY).[13, 14, 22, 23] Transmission is a mode wherein the incident x-ray beam carries sufficient flux to transmit fully through a sample and be detected

behind the sample. This is perhaps the simplest technique, at least conceptually, as it bears a direct measure of the x-ray absorption cross-section of a material via the Beer-Lambert law. However, transmission XAS requires that samples be sufficiently thin that *thickness effects* be negligible.[24, 25, 26] Moreover, the thickness must be known precisely and the thickness should not vary significantly over the surface of the x-ray beam spot. As these conditions are frequently too restrictive, researchers have developed electron and fluorescence yield methods that rely on the detection of by-products of the absorption process.

When a core hole is created by the absorption of an incident photon, the atom is briefly in an excited state ($\tau \sim 10^{-15}$ seconds).[14] The primary decay channels available to this atom are to either emit a characteristic x-ray (fluorescence x-ray) or eject one or more Auger electrons with the excess kinetic energy. The probability of either occurrence depends on the atomic shell involved and the atomic number Z of the atom.[27, 28, 29] For fluorescence yield, an x-ray detector such as a photodiode, channelplate or channeltron is typically used to detect the **total fluorescence yield** (TFY) that escapes the sample and reaches the detector.[30][1] Using an energy sensitive photon detector, such as a **silicon drift detector** (SDD), it is also possible to measure the **partial fluorescence yield** (PFY). In the case of Auger electron emission, the electron carries sufficient kinetic energy to cause subsequent excitations in nearby atoms, leading to a cascade of low energy secondary electrons comprised of both elastically and inelastically scattered electrons. Those electrons originating from sufficiently close to the surface of the material can escape into the atmosphere (typically vacuum) and be detected using a channelplate or channeltron detector. If the sample is electrically grounded and conductive, a drain current can flow into the sample and fill the vacancies left behind by this electron cascade. Because of the simplicity of this measurement scheme, the drain current is frequently used to measure the **total electron yield** (TEY).

While TEY and TFY measures are related to the absorption process, they are indirect measures and are not, *in general*, directly proportional to the x-ray absorption cross-section. Thankfully, there are useful limits in which these measures become approximately proportional to the cross-section. These scenarios will be discussed in sections 2.3 and 2.4.2.2 for EY and FY, respectively. However, even within these limits there are additional considerations that can result in loss of proportionality to the cross-section. For instance, electron yield measurements can often be distorted due to surface contamination or surface charging in insulators. Materials that oxidize easily may reveal big differences in their electron yield and fluorescence yield spectra, since the former is surface sensitive and the

[1] Gas ionization chambers can be used as well, but these require more maintenance and are generally much larger.

latter is bulk sensitive.[13] In such cases, it may be possible to discern that the electron yield is unreliable and conclude that the only straightforward alternative is a fluorescence yield measurement. Despite its bulk-sensitivity, fluorescence yield (FY) can produce erroneous results as well. For concentrated samples, the relationship between the FY and the absorption coefficient is non-trivial and saturation effects (often termed "self-absorption effects") become important. These effects can be minimized in the case of normal incidence and grazing detection, but never fully eliminated.

Attempts to account for saturation effects have been previously described (see Refs. [31] and [32]), but these approaches are not always viable for the reasons outlined in section 2.4.2.2. Both techniques make simplifying assumptions which are only valid is specific scenarios and are therefore limited in their general applicability to XAS. Moreover, even after correction for saturation effects, the resonant FY spectra can still contain systematic errors which complicates the determination of the absorption cross-section. Consequently, there is an experimental need for an alternative measure of the x-ray absorption cross-section that is not subject to limitations imposed by saturation effects and surface sensitivity.

In this thesis, I describe an alternative measure of XAS called **inverse partial fluorescence yield** (IPFY) that is bulk-sensitive, free of saturation effects, and provides a measurement that is directly proportional to the **total x-ray absorption coefficient**, $\mu_{\text{tot}}(E)$. IPFY is a form of partial fluorescence yield that relies on the detection of fluorescence photons resulting from *non-resonant* transitions and is inversely related to $\mu_{\text{tot}}(E)$. Moreover, IPFY does not suffer from saturation effects present in resonant fluorescence yield measurements. I will further demonstrate how a simple geometrical factor in the expressions describing this measurement technique can be exploited to accurately determine $\mu_{\text{tot}}(E)$ over a wide energy range, capturing both the EXAFS and XANES spectral regions of XAS measurements.

1.2 X-ray absorption

1.2.1 Attenuation

The attenuation of light through a homogeneous material is known empirically to obey the Beer-Lambert law.[12, 13, 14, 33] A traveling electromagnetic (EM) wave with initial intensity I_0 will experience an exponential decay of its intensity as it traverses through a material.[2] We can see why this is if we assume that a material attenuates the EM wave

[2]The intensity of a traveling electromagnetic wave is given as the magnitude of the Poynting vector $I_0 = |\boldsymbol{S}| = \epsilon_0 c|\boldsymbol{E}|^2$, where the electric field is defined as $\boldsymbol{E}(\boldsymbol{r}, t) = \boldsymbol{\epsilon}_p E_0 e^{i(\boldsymbol{k}\cdot\boldsymbol{r}-\omega t)}$. Here $\boldsymbol{k}$ is the wavevector,

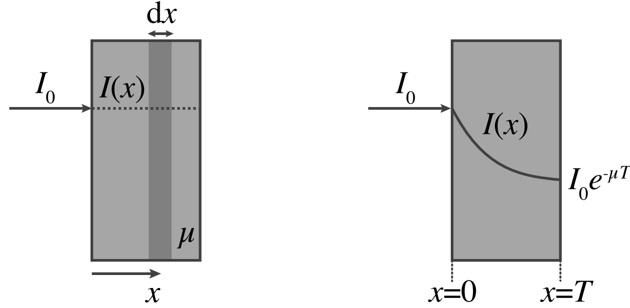

Figure 1.1: The attenuation of light as it traverses through a homogenous material

intensity linearly by a factor μ over a narrow thickness of sample dx. This assumption leads to the simple differential equation $-\mathrm{d}I(x) = I(x)\mu\mathrm{d}x$ whose solution is given by Eq. (1.1). Figure 1.1 demonstrates this relationship.

$$I(x) = I_0 e^{-\mu x} \tag{1.1}$$

The quantity μ is known as the **linear x-ray absorption coefficient** or linear attenuation coefficient. The **x-ray absorption cross-section** σ^{abs} is directly related to the linear attenuation coefficient by the relationship $\mu = \rho_{\text{a}}\sigma^{\text{abs}}$, where ρ_{a} is the atomic number density.[13] For a material composed of multiple elements, the total x-ray absorption coefficient is given by the sum over the various atomic contributions

$$\mu_{\text{tot}} = \sum_j \rho_{a,j}\sigma_j^{\text{abs}}. \tag{1.2}$$

1.2.2 Transition probability

The field of x-ray absorption spectroscopy relies on the fact that the cross-section σ^{abs} depends explicitly on photon energy, $E = h\nu$. The incident electromagnetic wave acts as a time-dependent perturbation of the sample that gives rise to transitions of core electrons from an initial state $|i\rangle$ to a final state $|f\rangle$. The probability of a transition occurring is given by Fermi's Golden Rule [Eq. (1.3)]

$$T_{if}(h\nu) = \frac{2\pi}{\hbar}|M_{if}|^2\delta(\epsilon_i - \epsilon_f - h\nu)\rho(\epsilon_f), \tag{1.3}$$

$\boldsymbol{\epsilon}_p$ is the unit polarization vector, ω is the angular frequency, t is time, E_0 is the amplitude of the electric field, ϵ_0 is the permittivity of free space and c is the speed of light in vacuum.

where M_{if} is a transition matrix element, ϵ_i and ϵ_f are the energy levels of the initial and final states, and $\rho(\epsilon_f)$ is the density of the final state.[13, 14, 20, 33] For the x-ray absorption process[3] the transition matrix element is given by

$$M_{if} = \langle f|\mathcal{H}_{\text{int}}|i\rangle, \tag{1.4}$$

and the interaction Hamiltonian is taken to be

$$\mathcal{H}_{\text{int}} = \frac{e}{m_e}\boldsymbol{p}\cdot\boldsymbol{A}, \tag{1.5}$$

where e/m_e is the electron charge/mass, $\boldsymbol{p}$ is the electric dipole moment and $\boldsymbol{A}$ is the vector potential. The vector potential is related to the electric field of the EM wave by $\boldsymbol{E} = -\partial\boldsymbol{A}/\partial t$, which makes it clear that the transitions are driven by the electric field of the incident photons.[4] The absorption cross-section thus has an explicit dependence on photon energy and can be defined as

$$\sigma^{\text{abs}}(E) = \frac{T_{if}(E)}{\Phi_0}, \tag{1.6}$$

where division by Φ_0 is to normalize the transition probability to the incident photon flux.

1.2.3 Spectroscopic notation

For a free atom irradiated with x-rays, sharp discontinuities in the transition probability occur at well-defined energies corresponding to the difference in electron binding energies. These discontinuities are called **edge steps**. The edge steps are labeled K, L, M, N, O, and P indicating the core shell of the initial state. For instance, absorption at the K edge corresponds to an electron transitioning from an initial state with principal quantum number $n = 1$.[13]

Transitions between states can also involve a change in the azimuthal quantum number ℓ and/or the magnetic quantum number m_ℓ. Changes in spin s or the spin projection quantum number m_s are not allowed for linearly polarized light, although $m_s = \pm 1$ is allowed for circularly polarized light. The rules governing transitions are generally referred to as *dipole selection rules* and are summarized for linearly polarized light in Eq. (1.7).

[3] X-ray absorption is a first order transition, whereby the transition from $|i\rangle$ to $|f\rangle$ is direct and does not involve any intermediate steps. In second order transitions, the system can pass through a series of virtual intermediate states $|n\rangle$ and a second order term is needed in the matrix element.[13]

[4] The vector potential is quantized in order to reflect the quantum nature of the interactions.

These rules occur by inspection of the nonvanishing matrix elements in T_{if} under the *dipole approximation.*[13][5]

$$\begin{aligned} \Delta l &= \pm 1 \\ \Delta m_\ell &= 0, \pm 1 \\ \Delta s &= 0 \\ \Delta m_s &= 0 \end{aligned} \tag{1.7}$$

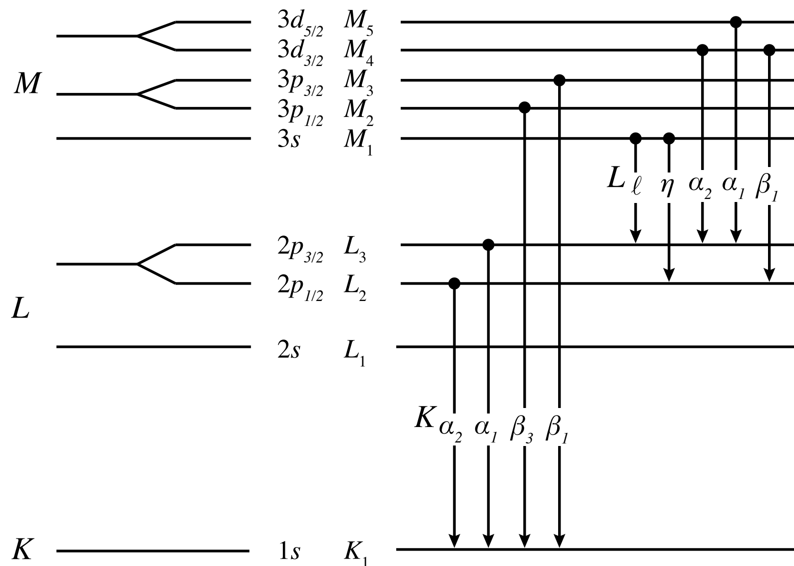

Figure 1.2: A schematic representation of the energy levels of core electrons up to $n = 3$ and a selection of characteristic x-ray emission lines illustrating the conventional x-ray spectroscopic nomenclature. (Figure adapted from diagrams in Refs. [6, 12, 13])

In addition to the edge labels denoting the energy levels, a numerical subscript is usually added to indicate the subshell of the initial state. For instance, the K edge corresponds to an initial $1s$ state while the L_3, L_2 and L_1 edges correspond to initial $2p_{3/2}$, $2p_{1/2}$ and $2s$

[5]The dipole approximation simplifies the transition matrix by assuming that the absorbing atomic shell is small relative to the x-ray wavelength and hence that the electric field is constant over the volume of the atom.

states, respectively. Figure 1.2 illustrates the levels and the nomenclature. Here we follow the conventional labelling of electronic states when the spin-orbit effect is present: the first number indicates the core level or n, the letter indicates the subshell or ℓ and the subscript indicates the total angular moment quantum number $j = s + \ell$.

Transitions from higher energy states to lower energy states, as in the decay of an excited atom to its normal state, can emit characteristic x-rays. The emission lines follow the nomenclature indicated in Fig. 1.2. In this case, the K, L and M indicate the n of the final state rather than the initial state. The subscripts for the main emission lines follow the Siegbahn notation.[15]

1.2.4 X-ray absorption spectra

In order to appreciate the features of x-ray absorption spectra for solid matter, we will first consider a simple one-electron picture of the absorption process for an isolated atom as it contains much of the essential physics. In this system, the initial and final states are the atomic Rydberg levels. If the photon energy is set below that of the lowest energy transition, the probability of absorption is zero. As the photon energy is increased, one possible transition channel is opened and the absorption increases discontinuously. Between this energy and the vacuum level E_{v} (the ionization potential of the atom), the excited electron can transition to any of the available states with transition rates defined by T_{if}. Above E_{v}, all the possible states merge to form a continuum of states into which the electron can transition into. This leads to a spectrum that has a series of resonances below the ionization potential and then an edge step at the ionization potential, as depicted in Figure. 1.3(a).

The picture of x-ray absorption in a solid is not considerably different. Instead of a series of unoccupied Rydberg states, solids have band structure and an associated density of states (DOS), $\rho(E)$.[13] In a semiconductor, for example, states below the Fermi level, E_{F}, are occupied and hence cannot be channels for electronic transitions because of Pauli's exclusion principle. Between E_{F} and E_{v} exist a number of unoccupied states also associated with the DOS. This material-specific DOS alters T_{if} from the simple picture of Rydberg states in an isolated atom, resulting in near-edge band resonances commonly referred to as XANES. The calculation of the XANES structure requires careful consideration of the electronic configuration of the initial and final states.[14]

Above E_{v}, the incident photon has sufficient energy to ionize the atom and the density of unoccupied states becomes a continuum that resembles the purely atomic continuum. Hence, above E_{v} the absorption spectrum converges to the atomic absorption. However, the

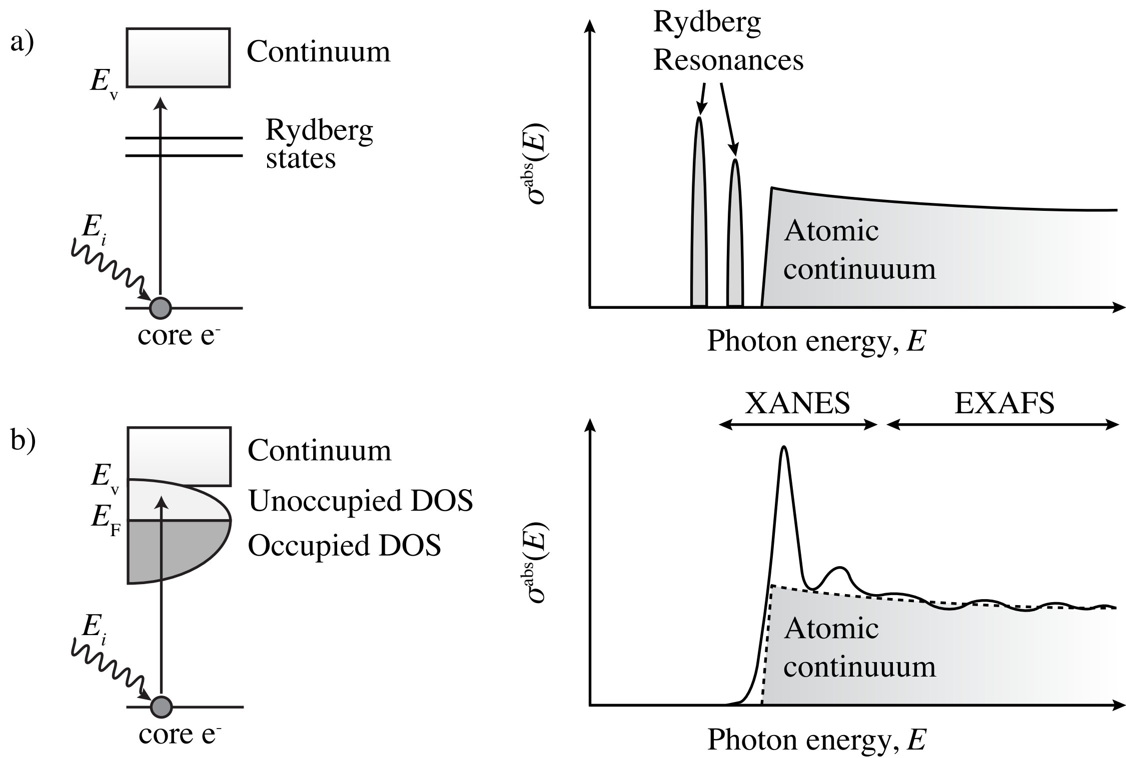

Figure 1.3: A schematic representation of the x-ray absorption mechanism and resulting absorption spectrum for a) a one-electron atomic system and b) for a general solid. (Figure adapted from Ref. [13])

ejected photoelectrons, treated quantum mechanically as waves, interact with the neighbouring atoms as they travel through the solid. These interactions lead to multiple scattering effects that are felt as wave interference at the original absorbing atom and modifies the transition matrix.[19] In x-ray absorption spectra, this effect appears above the near-edge structure as a periodic variation in the x-ray absorption from the atomic value, commonly referred to as EXAFS. A Fourier transform analysis of EXAFS data can often be used to accurately determine nearest neighbour bonding distances and coordination.[18, 19]

The fine structure contained in the DOS of solids can also give rise to transition probabilities that depend on the polarization of the incident photons. These so-called *dichroism* effects arise in a number of forms: x-ray linear dichroism (XLD), x-ray magnetic linear dichroism (XMLD) and x-ray magnetic circular dichroism (XMCD).[13] XLD typically oc-

curs when the charge distribution around the absorbing atom is anisotropic, typically due to a non-cubic crystal structure. Cubic systems can nevertheless exhibit dichroism through the XMLD effect. In XMLD, some type of magnetic order (eg. antiferromagnetic order) breaks the cubic symmetry and introduces a charge anisotropy. XMCD relies on the fact that the density of occupied states for magnetically ordered materials depends on the spin orientation. In this case, the interaction of right or left circularly polarized photons with the magnetic material will give rise to different transition probabilities. Magnetic dichroism spectroscopy is a rich field of research with many interesting applications.[34] However, in this thesis, we shall only briefly mention dichroism effects and focus generally on the total x-ray absorption coefficient, which in principle includes dichroism effects.

1.3 Importance of $\mu_{\mathbf{tot}}(E)$

Many avenues of research utilize XANES and EXAFS measurements to determine information about the electronic structure and coordination of atoms in a lattice. Perhaps somewhat overlooked, however, is that XAS could also be a powerful tool in the determination of sample stoichiometry. The energy dependence of the x-ray absorption coefficient and the magnitude of the edge jumps are directly related to the atomic densities of the elements contained in a sample [Eq. (1.2)]. Because of the difficulties associated with correcting TEY and TFY spectra for saturation and surface effects (see section 2.4), this information is seldom used. However, with an accurate measurement of $\mu_{\text{tot}}(E)$, it would be possible to utilize the data to non-destructively determine the stoichiometry of a sample without the need for a different experimental setup.

Additionally, XAS is often used to determine the optical properties of matter such as the complex atomic form factor, f, and correspondingly the complex index of refraction n. The $\text{Im}\{f\}$ is related to the x-ray absorption cross-section by the relation

$$\text{Im}\{f(E)\} = \frac{E\sigma(E)}{2hcr_e}, \tag{1.8}$$

where h is Planck's constant and r_e is the classical electron radius.[35] The $\text{Re}\{f(E)\}$ can be determined via the optical theorem by performing a Kramers-Kronig transformation and therefore the form factor $f(E)$ can be fully determined.[13, 35] The index of refraction can be obtained from the complex form factor via

$$n(E) = 1 - \frac{r_e}{2\pi}\lambda^2 \sum_j \rho_{a,j} f_j(E) \tag{1.9}$$

where $\rho_{a,j}$ is the atom number density of atom j and λ is the wavelength.

These determinations of $f(E)$ and $n(E)$ can be extremely valuable in modelling of resonant scattering or understanding the optical properties of materials.[14] One difficulty with the conventional approach is that TEY or TFY data is used as an input for the cross-section in $\mathrm{Im}\{f(E)\}$. The optical theorem depends on having a true measure of σ or $\mu_{\mathrm{tot}}(E)$. As explained in section 2.4, TEY and TFY are generally not proportional to σ because of saturation and surface effects. Hence, some difficulties arise in the interpretation of calculations based on these inputs.

First, in order to obtain σ from TEY or TFY spectra, one has to normalize the spectra above and below an absorption edge to tabulated x-ray absorption coefficients to obtain a quantitative measure of σ.[36, 13] This normalization is often subject to systematic errors, either because the XAS spectra do not extend far enough above the EXAFS, or because of errors inherent to the tabulated values which are largest near absorption edges. Second, there is typically an energy dependent background to the XAS related to absorption edges at lower energy which must be subtracted from the XAS in order to isolate σ for the element of interest. This subtraction can also introduce an arbitrary systematic error to the calculation. Finally, all of these correction steps depend on knowledge of the sample stoichiometry, which is not always known precisely.

An experimental technique that could provide a measure that is directly proportional to $\mu_{\mathrm{tot}}(E)$ would be extremely valuable in both determining sample stoichiometry and as an input to calculations of the atomic form factor. While EY and resonant FY measurements have been commonly used for this purpose, there are cases where these fail to truly represent $\mu_{\mathrm{tot}}(E)$. The following chapters are devoted to the development of a technique called inverse partial fluorescence yield that addresses this limitation. I will first develop the theoretical background of EY and FY needed to understand their limitations. I will then extend the theory of FY with the goal of deriving an expression defining the IPFY. I will then demonstrate that IPFY obeys this theoretical framework using experimental results. The advantages of IPFY over TEY, TFY and resonant PFY will also be demonstrated experimentally. Finally, I will consider the special cases of multilayers and powder specimens, where the theory of fluorescence yield requires approximations and is not as well-behaved as in thick, homogenous samples.

Chapter 2

Experimental Techniques

2.1 Transmission

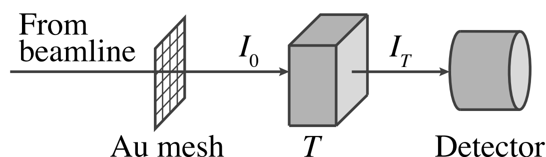

Figure 2.1: The transmission geometry. The incident flux is measured using a gold mesh (depicted) or an ionization chamber and the transmitted intensity is measured using a photon sensitive detector.

Conceptually, the simplest way to measure XAS is in the transmission geometry (Fig. 2.1). If the x-ray penetration depth exceeds the thickness of the sample at all energies of interest, then the ratio of the initial intensity to the transmitted intensity is a direct measure of $\mu(E)$. Eq. (1.1) is used to solve for $\mu(E)$ in Eq. (2.1) for a sample of thickness T.

$$\mu(E) = -\frac{1}{T} \ln \left(\frac{I_T(E)}{I_0(E)} \right) \tag{2.1}$$

To perform the experiment requires a measure of the photon flux or intensity prior to reaching the sample (typically after the last optical element) and directly behind the sample. The incident intensity is often recorded using the drain current from a gold mesh

with $\sim$85% transmission or using a gas ionization chamber. The drain current from a Au mesh is a measure of the total electron yield of Au far from its absorption edges which is related to the photon flux. The concept of electron yield is detailed in section 2.3. The transmitted intensity is recorded either with a photodiode or channelplate detector located in the beam direction. Having measured all the unknowns, it is a straightforward to deduce $\mu(E)$ from a transmission experiment. Unfortunately, transmission experiments are often not possible or are subject to limitations (see section 2.4.1) and alternative measures of $\mu(E)$ are required.

2.2 Fluorescence yield

When a core hole is created by absorption of an incident photon, the atom is temporarily in an excited state and will rapidly decay ($\tau \sim 10^{-15}$ s) by emission of a fluorescence photon or ejection of one or more Auger electrons.[14] Fluorescence yield (FY) relies of the detection of the emitted fluorescence photons. The number of fluorescence photons can be related to the number of core holes created by consideration of the experimental geometry. Here I follow the standard development presented in Refs. [31, 32, 22, 37] with slightly different notation consistent with Ref. [38] and only considering the primary fluorescence contribution.[1]

We consider a homogeneous bulk sample of thickness d in the experimental geometry considered in Fig. 2.2, where the angle of incidence is α and the angle of detection is β. The incident photons have energy E_i, the fluorescence photons have energy E_f and the measured intensity at the detector will in general depend on both. For clarity's sake, we will only consider the contribution from one element/core state at present. In this case, we can write the normalized differential intensity contribution from a thin layer with thickness dz at a depth z as

$$\frac{\mathrm{d}I(E_i, E_f)}{I_0(E_i)} = \eta(E_f)\frac{\Omega}{4\pi}\omega(E_i, E_f)\frac{\mu(E_i)}{\sin\alpha}e^{-\left(\frac{\mu(E_i)}{\sin\alpha}+\frac{\mu(E_f)}{\sin\beta}\right)z}\mathrm{d}z. \tag{2.2}$$

Here $\eta(E_f)$ is the detector efficiency, Ω is the solid angle made by the detector, $\omega(E_i, E_f)$ is the probability that an incident photon of energy E_i will lead to a fluorescence photon of energy E_f rather than emission of one or more Auger electrons, and $\mu(E_i)$ and $\mu(E_f)$

[1] Ref. [37] works out the fluorescence intensity in the case of primary and secondary fluorescence. However, in the cases of interest here, secondary fluorescence will be negligible as the fluorescence probability is already quite low.

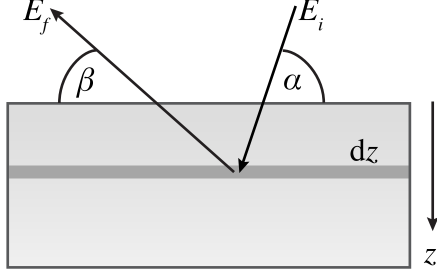

Figure 2.2: The fluorescence yield geometry. The angles α and β measured relative to the sample surface.

are the total linear attenuation coefficients of the material at energies E_i and E_f. The exponential terms in Eq. (2.2) account for the attenuation of the incident and emitted intensity by the absorption of the material. Division by $\sin\alpha$ and $\sin\beta$ accounts for the fact that the depth z is measured perpendicular to the sample surface, whereas the paths traversed by the photons are not.

We integrate Eq. (2.2) for a sample of thickness d and explicitly account for all contributions from different atoms/core states denoted by X (eg. X = Ni $2p_{3/2}$, Ni $2p_{1/2}$, O $1s$, $\ldots$). X dependence is explicitly added for the $\omega(E_i, E_f)$ term and the $\frac{\mu(E_i)}{\sin\alpha}$ term outside the exponential as these are atom specific, while the terms in the exponential are the *total* linear x-ray absorption coefficients. This integration is straightforward and leads to

$$\begin{aligned}\frac{I(E_i, E_f)}{I_0(E_i)} &= \eta(E_f)\frac{\Omega}{4\pi}\sum_X \int_0^d \omega_X(E_i, E_f)\frac{\mu_X(E_i)}{\sin\alpha} e^{-\left(\frac{\mu(E_i)}{\sin\alpha}+\frac{\mu(E_f)}{\sin\beta}\right)z} \mathrm{d}z. \\ &= \eta(E_f)\frac{\Omega}{4\pi}\sum_X \frac{\omega_X(E_i, E_f)\mu_X(E_i)}{\mu(E_i)+\mu(E_f)\frac{\sin\alpha}{\sin\beta}}\left[1 - e^{-\left(\frac{\mu(E_i)}{\sin\alpha}+\frac{\mu(E_f)}{\sin\beta}\right)d}\right]. \end{aligned} \tag{2.3}$$

The term in square brackets is 1 if $\left(\frac{\mu(E_i)}{\sin\alpha}+\frac{\mu(E_f)}{\sin\beta}\right) d \gg 1$, which is satisfied for samples that are thick relative to the penetration lengths of the incident and fluorescence photons. Hence, in the case of thick, homogenous samples, we can define the TFY as

$$\frac{I(E_i, E_f)}{I_0(E_i)} = \eta(E_f)\frac{\Omega}{4\pi}\sum_X \frac{\omega_X(E_i, E_f)\mu_X(E_i)}{\mu(E_i)+\mu(E_f)\frac{\sin\alpha}{\sin\beta}}. \tag{2.4}$$

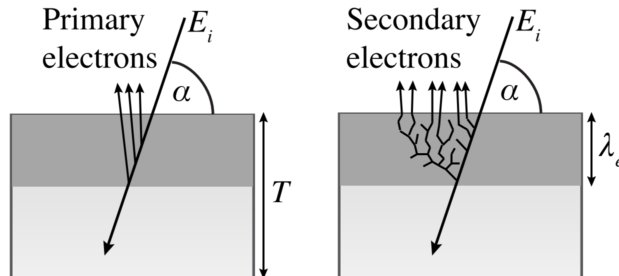

Figure 2.3: Schematic representation of electron emission processes.

2.3 Electron yield

In addition to the radiative decay channel leading to fluorescence, excited atoms can also decay non-radiatively by ejecting electrons. These electrons can interact with other atoms and produce a cascade of electrons escaping from the sample. The theoretical description of these interactions can quickly become rather complex and a number of approximations are necessary to describe the electron yield. The most common measurement of XAS by electron yield is in the total electron yield mode, for which all electrons that escape from a sample per unit time are counted.

In order to model TEY, we must consider all the channels that can lead to the escape of an electron from a sample. Firstly, if the photon energy is below the lowest transition energy of the core electron, no absorption will take place. However, if the photon energy is above the transition energy, it is possible to directly eject photoelectrons. The ejection of a photoelectron may be accompanied by the emission of one or more Auger or Coster-Kronig electrons.[23] Those electrons that manage to directly escape to the vacuum are termed *primary electrons*. However, many electrons will interact with other atoms before reaching the vacuum. This will lead to the ejection of additional low energy electrons originating from the valence band of the other atoms. The electrons resulting from these interactions are termed *secondary electrons*. These mechanisms are illustrated in Fig. 2.3.

A complete description of EY is beyond the scope of this thesis. There have been numerous papers and texts devoted to this.[9, 17, 23, 39] Here we shall summarize a general TEY expression and the assumptions that went into its derivation.[23, 39, 40] The main assumptions can be summarized as:

1. Primary electrons contribute a small fraction of the total yield and can be neglected.

2. The fluorescence probability is low and hence all the energy deposited at a depth z is transferred into secondary electron generation.

3. The secondary electron concentration at a depth z is given by $\epsilon^{-1}(-\mathrm{d}E/\mathrm{d}z)$ where ϵ is the effective energy required to create one secondary electron and $E(z)$ is the energy of an electron at depth z.

4. Refraction and specular reflection at the vacuum/sample interface are negligible.

5. The probability that a secondary electron escapes from a depth z is given by $P_s(z) = P_s(0)e^{-z/\lambda_e}$, where λ_e is the characteristic **electron escape depth** and $P_s(0)$ is the electron escape probability at the surface (typically assumed to be between 1/2 and 1)

If all these conditions are met, then the TEY is largely described by the secondary electron yield, which has the following form

$$\begin{aligned} Y(E) &= P_s(0)E\epsilon^{-1}\int_0^{\mu(E)T\csc\alpha} e^{-(1+\frac{1}{\mu\csc\alpha\lambda_e})z}\mathrm{d}z \\ &= P_s(0)E\epsilon^{-1}\frac{\mu(E)\csc\alpha}{\mu(E)\csc\alpha+\frac{1}{\lambda_e}}\left[1-e^{-T(\mu(E)\csc\alpha+\frac{1}{\lambda_e})}\right] \end{aligned} \quad (2.5)$$

Then, if $T \gg \lambda_e$ and $\frac{1}{\mu\csc\alpha} \gg \lambda_e$, Eq. (2.5) simplifies to $Y(E) \propto \mu(E)E$.[23, 39] This relationship does not hold generally for all materials and all experimental conditions, but has been found to be appropriate in certain cases and has helped to make TEY an essential measurement technique at almost all soft x-ray XAS beamlines.

The measurement of the TEY is typically done in one of two ways: detection with a channelplate detector or measurement of the drain current into the sample.[9, 13, 17] Detection with a channelplate requires that a detector be placed near the surface of the sample to count the number electrons escaping from the sample. The channelplate only collects a small fraction of the ejected electrons based of its solid angle and its detection efficiency. The drain current technique relies on electrically grounding the sample. As electrons escape, a current flows into the sample to fill the vacancies. The drain current approach is favoured at synchrotrons as it is a reliable measure of the TEY and is simple to implement.

2.4 Experimental limitations

The prior discussion of the transmission (section 2.1), fluorescence yield (section 2.2) and electron yield (section 2.3) measurement techniques has focused on developing the framework for understanding the physics of the measurement. Such theoretical descriptions are necessary in order to appreciate the conditions required for successful measurements using these techniques as well as understanding their limitations. Here, we will discuss how these techniques can lead to erroneous results and specify of how such failures of the measurement can occur.

2.4.1 Thickness and pinhole effects

In the transmission geometry, one obvious requirement is that the x-rays can penetrate fully through the sample. For soft x-rays, this can be a challenging condition as the penetration depth of soft x-rays for transition metals is on the order of 1000 Å or 0.1 μm. Transmission experiments with soft x-rays thus require ultrathin samples. Aggravating this situation are thickness effects.[24, 25, 26] Thickness effects arise from additional contributions to the detected x-ray intensity. For instance, x-ray fluorescence and Bragg scattering can both contribute additional counts on the detector placed behind the sample. The effect is amplified by increasing the sample thickness. The general criterion to minimize the thickness effect is to use the thinnest possible sample.

Additionally, variations in the sample thickness can lead to attenuation that depends also on the spatial position of the beam spot. This problem is sometimes referred to as a *pinhole effect*, referring to the fact that an unusually thin portion of the sample can act like a pinhole with less attenuation than expected for the mean sample thickness. Very thin samples are more sensitive to small thickness variations, so one would generally try to avoid thin samples to minimize pinhole effects.

The accuracy of a quantitative measure of the x-ray absorption coefficient is strongly affected by the precision to which the sample thickness is known. The criteria coming from the thickness and pinhole effects are in direct competition. On the one hand, to minimize thickness effects requires the use of very thin samples. On the other hand, very thin samples are subject to pinhole effects that can increase the uncertainty in the measured intensity. Moreover, the relative uncertainty in a measurement of the thickness of very thin sample is significantly worse than the uncertainty in the measurement of a thicker sample.

Consequently, the choice of sample thickness for a transmission experiment is not always trivial. Optimally, the thinnest sample is used so long as the relative uncertainty in its

thickness remains small. Unfortunately, growing thin materials is not always an option, and appropriate samples may simply not be available. In cases where thin samples are available, careful consideration of the sample thickness and its uniformity must be observed in order to reliably determine $\mu_{\text{tot}}(E)$.

2.4.2 Saturation effects

Signal saturation effects can occur for electron yield and fluorescence yield measurements. Saturation refers to a loss of proportionality to the x-ray absorption coefficient. Here we will address the physical origin of signal saturation in electron yield and fluorescence yield, the effect of saturation in experimental spectra, and comment on attempts to account for these effects.

2.4.2.1 Electron yield saturation

In deriving the relationship between TEY and $\mu(E)$, $Y(E) \propto \mu(E)E$, the condition $\frac{1}{\mu \csc \alpha} \gg \lambda_e$ was necessary. In effect, this condition states that the penetration length of the x-rays measured perpendicular to the surface, λ_x, must be much greater than the electron escape depth, λ_e. If this limit is violated experimentally such that $\lambda_x < \lambda_e$, nearly all photons are absorbed within the electron escape depth and therefore all generated electrons will escape — a complete loss of proportionality to $\mu(E)$ occurs. These two cases are illustrated in Fig. 2.4.

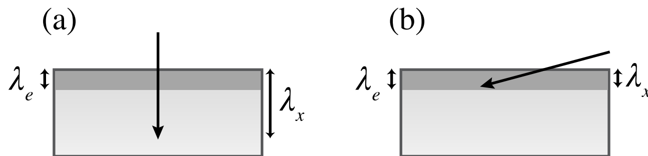

Figure 2.4: Schematic representation of saturation effect limits. (a) Normal incidence. $\lambda_x \gg \lambda_e$, so saturation effects are small. (b) Grazing incidence. $\lambda_x < \lambda_e$ and a complete loss of proportionality to $\mu(E)$ occurs.

Since measurement at either limit is physically difficult to realize, a typical experiment lies somewhere in between these two limits where the measurement is neither fully saturated nor entirely free of some degree of saturation. Nakajima *et al.* have studied the electron

yield saturation effect at the L edge of Fe, Co and Ni using soft x-rays and have shown that the degree of saturation depends on the ratio λ_e/λ_x and the angle of incidence α.[41] The effect is essentially negligible if $\lambda_e/\lambda_x = 0.003 \ll 1$ and measurements are performed far from grazing incidence ($\alpha > 30°$). However, even at a modest value of $\lambda_e/\lambda_x = 0.02$, a non-negligible saturation factor exists at all measurement angles. Since λ_x varies significantly as a function of photon energy across an absorption edge, the ratio λ_e/λ_x is not fixed for a given measurement, and so the size of the saturation effect depends on photon energy (maximized at absorption peaks).[2]

Nakajima *et al.* also present an elegant method to account for electron yield saturation effects and correct the recorded spectra.[41] Their technique relies on accurate knowledge of the electron escape depth and x-ray absorption length of Fe, Co and Ni. They determined λ_e using TEY data measured for different thicknesses of these metals which were grown as thin wedges. They also performed transmission measurements to determine the x-ray absorption length.

Unfortunately, this approach is not typically viable as it requires thin wedge-shaped samples which are challenging to grow and are not generally available. As a result, one does not normally have an accurate measure of λ_e and must instead rely on a crude estimate. In that case, the correction scheme of Nakajima *et al.* can be subject to considerable error and is not truly appropriate. Consequently, the correction of electron yield saturation effects is rather limited in practice. While one can use the approach to obtain a sense for the magnitude of the saturation effect, it is not generally well suited for cases where a reliable measure of $\mu_{\text{tot}}(E)$ are needed.

2.4.2.2 Fluorescence yield saturation

Saturation effects in fluorescence yield measurements occur due to the absorption of incident photons into the sample and a *lack* of absorption for fluorescence photons exiting the sample.[31, 32] This is often termed a *self-absorption effect*, but I will explain shortly why this terminology is more confusing than simply a *saturation effect*. To get a sense for this phenomenon, we will consider two limiting cases of FY detection and qualitatively consider the behaviour in between.

To maximize the saturation effect, a grazing incidence and normal takeoff geometry is used [see Fig. 2.5(a)]. In this case, nearly all photons are absorbed close to the surface of the sample. If the geometry is selected such that photons emitted normal to the sample

[2] The electron escape depth also varies with photon energy, but this variation is less important than the variation of the x-ray penetration depth.[17]

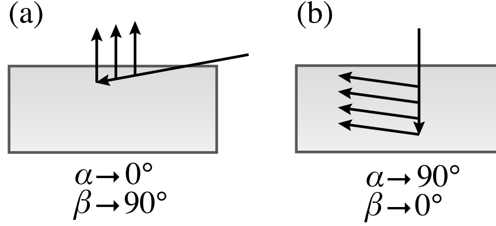

Figure 2.5: (a) Grazing incidence, normal takeoff geometry. (b) Normal incidence, grazing takeoff geometry. Saturation effects are maximized in (a), since nearly all fluorescence photons can escape without much absorption. In (b), the FY becomes approximately proportional to $\mu_Y(E)$. This figure has been adapted from Ref. [32].

surface are detected, then nearly all fluorescence photons can escape from the sample. The number of photons detected then are related to the photon flux and not to the absorption of the material – signal saturation has occurred. In this sense, it is actually a *lack of absorption* of the fluorescence photons that gives rise to the saturation of the measured signal, opposite to the implied meaning of the phrase *self-absorption effect*.

In the normal incidence, grazing takeoff geometry [see Fig. 2.5(b)], photons travel a large distance into the sample and an even larger distance to escape from the sample. These photons are then effectively attenuated by the absorption of the sample and the detected photon intensity is nearly proportional to the absorption coefficient. Figure 2.6 illustrates saturation effects in the XANES region of Co metal across the Co L_3 and L_2 edges.[32] The saturation effect is largest for minimal $\frac{\sin\alpha}{\sin\beta}$ ($\alpha = 5.71°$) and smallest for maximal $\frac{\sin\alpha}{\sin\beta}$ ($\alpha = 89.42°$).

To put saturation effects into a practical and theoretical framework, let us consider the simple case of absorption at the L_3 edge of pure Ni as an example. The TFY is given by Eq. (2.4). Assuming that we have the ability to isolate different emission lines, we can obtain a measure of the partial fluorescence yield, and measure only the fluorescence due to the Ni L_3 absorption, so that the sum in Eq. (2.4) is dropped and only one term remains. The PFY is then then given by

$$\frac{I(E_i, E_f)}{I_0(E_i)} = \eta(E_f)\frac{\Omega}{4\pi}\frac{\omega_{\mathrm{Ni}_{L_\alpha}}(E_i, E_f)\mu_{\mathrm{Ni}_{L_3}}(E_i)}{\mu(E_i) + \mu(E_f)\frac{\sin\alpha}{\sin\beta}}. \tag{2.6}$$

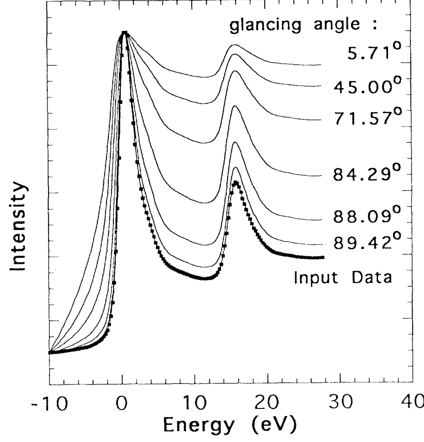

Figure 2.6: Simulation of the saturation effect at the Co L_3 and L_2 edges. An electron yield spectrum was used as an input to represent the non-distorted x-ray absorption coefficient. Calculations to show the effect of saturation at various angles are shown. From top to bottom the value of $\frac{\sin\alpha}{\sin\beta}$ increases and the saturation effect decreases. (Reprinted figure with permission from Ref. [32]. Copyright (1993) by the American Physical Society.)

For grazing incidence and normal takeoff, $\frac{\sin\alpha}{\sin\beta} \rightarrow 0$ and Eq. (2.6) becomes

$$\begin{aligned} \frac{I(E_i, E_f)}{I_0(E_i)} &\approx \eta(E_f)\frac{\Omega}{4\pi}\frac{\omega_{\mathrm{Ni}_{L_\alpha}}(E_i, E_f)\mu_{\mathrm{Ni}_{L_3}}(E_i)}{\mu(E_i)} \\ &\approx \eta(E_f)\frac{\Omega}{4\pi}\omega_{\mathrm{Ni}_{L_\alpha}}(E_i, E_f) \end{aligned} \tag{2.7}$$

since $\mu(E_i)$, the total absorption coefficient, is given approximately by $\mu_{\mathrm{Ni}_{L_3}}(E_i)$ for pure Ni.[3] Hence, this demonstrates that the measured FY signal bears very little proportionality to $\mu(E_i)$ in the grazing incidence, normal takeoff geometry.

Similarly, if we consider normal incidence and grazing takeoff, then $\frac{\sin\alpha}{\sin\beta} \gg 1$ and

[3]This assumes that the absorption due to M levels in Ni, μ_{other}, is small compared to $\mu_{\mathrm{Ni}_{L_3}}(E_i)$ near the L_3 edge. This is not strictly true, as the absorption tail coming from the Ni M levels contribute an energy dependent background about one order of magnitude smaller than the absorption due to the L_3 absorption edge.[36] However, this approximation is often made to illustrate the extreme case of the saturation effect.

$\mu(E_f)\frac{\sin\alpha}{\sin\beta} \gg \mu(E_i)$ so Eq. (2.6) becomes

$$\begin{aligned} \frac{I(E_i,E_f)}{I_0(E_i)} &\approx \eta(E_f)\frac{\Omega}{4\pi}\frac{\omega_{\mathrm{Ni}_{L_\alpha}}(E_i,E_f)\mu_{\mathrm{Ni}_{L_3}}(E_i)}{\mu(E_f)\frac{\sin\alpha}{\sin\beta}} \\ &\propto \omega_{\mathrm{Ni}_{L_\alpha}}(E_i,E_f)\mu_{\mathrm{Ni}_{L_3}}(E_i). \end{aligned} \tag{2.8}$$

So, in this limiting case, the FY signal becomes proportional to $\mu_{\mathrm{Ni}_{L_3}}(E_i)$.

Of course, this simplification relied on our ability to measure the PFY. In the case of a TFY measurement, this simple analysis becomes slightly more complicated. While the denominator can be simplified in the same way, each fluorescence contribution has a different probability ω_X of occurring, so the final simplified expression is given as

$$\frac{I(E_i,E_f)}{I_0(E_i)} \propto \sum_X \omega_X(E_i,E_f)\mu_X(E_i), \tag{2.9}$$

which unfortunately does not readily simplify to $\mu_{\mathrm{tot}}(E_i)$ since the $\omega_X(E_i,E_f)$ are not known precisely. Moreover, because measuring in this limit introduces a very large denominator, the measured fluorescence flux decreases, and the signal to noise ratio of the measurement is diminished.

In typical fluorescence yield measurements, neither limit is readily achievable and detection occurs somewhere in between, where neither of the above simplifications are valid and saturation effects are generally always present, albeit to varying degrees. Eisebitt *et al.* [32] and Tröger *et al.* [31] have developed approaches to correct soft x-ray FY spectra for saturation effects in the XANES and EXAFS regions. However, their techniques rely on assumptions which limit their utility towards XAS measurements performed over wide energy ranges.

Eisebitt *et al.* use a method which assumes that $\mu_{\mathrm{other}}(E_i)$ can be treated as a constant, which is only valid over a narrow energy range such as in a XANES measurement. They also assume that this constant is given by $\mu_{\mathrm{tot}}(E_f)$, which is only valid if one can measure the resonant PFY independent of other fluorescence contributions. Hence, their approach does not apply to TFY, which is currently the predominant mode of fluorescence detection implemented at XAS beamlines. Additionally, their approach effectively makes the assumption that the fluorescence probability ω_X of the level of interest X is independent of incident photon energy. However, their measurement across the Co L_3 edge corresponds to the detection of resonant x-ray emission processes, for which this assumption is not valid.[42] Consequently, their correction technique is not strictly appropriate in regions where ω_X depends on energy, such as in the region below the absorption maximum.

Tröger *et al.* demonstrate a method to correct the experimental EXAFS amplitude for saturation effects by estimating the magnitude of the saturation effect using tabulated values of the x-ray absorption coefficient for free atoms.[43] Their analysis assumes the sample stoichiometry is known and does not take into account the uncertainty associated with the tabulated calculations, which can be considerable at soft x-ray energies.[35] Moreover, they simply drop the largest order correction term coming from background absorption during their analysis. They estimated that this simplification would contribute an error between 5% to 10% to their final determination of the EXAFS amplitudes, but could not accurately include it to strictly account for background absorption.

As a result of these simplifying assumptions, the determination of $\mu_{\mathrm{tot}}(E)$ from resonant PFY can be subject to systematic errors even after accounting for saturation effects using the methods of Eisebitt *et al.* and Tröger *et al.* In practice, it is difficult to assess the success of these corrections, particularly if an accurate measure of the x-ray absorption coefficient is not available. Moreover, these approaches are not generally appropriate for XAS measurements that span over wide energy ranges or for spectra collected in the TFY mode. Hence, saturation effects remain a very real concern in many cases and limit the utility of resonant PFY or TFY towards the determination of $\mu_{\mathrm{tot}}(E)$.

It should be noted that saturation effects in FY are not so problematic for species which are in dilute concentration. This is due to the fact that the linear absorption coefficient of a dilute element, μ_{dilute}, will be considerably smaller than the contributions of other concentrated elements so that $\mu_{\mathrm{dilute}} \ll \mu_{\mathrm{tot}}$. In this case, the approximate cancelation of μ_{dilute} and μ_{tot} does not occur and saturation effects can be said to be negligible.

2.4.3 Surface effects

Electron yield measurements are inherently sensitive to surface contamination effects. The information depth of electron yield is primarily determined by the electron escape depth of secondary electrons, which is typically on the order of ~ 50 Å for metals and semiconductors.[44, 45] Because of this surface sensitivity, XAS practitioners often attempt to cleave their samples prior to measurement to expose a fresh surface. Otherwise, surface contamination (often in the form of oxidation) can lead to erroneous conclusions about the bulk properties of the material, particularly if the surface contamination is comprised of the same elements as in the bulk but with a different valence. While cleaving will expose a surface that has not been in extended contact with air, it may expose a surface that is particularly weak (eg. due to vacancies or inhomogeneities) which has properties that are not representative of the bulk properties of the material. Moreover, cleaving is not

always possible, such as with powders or materials that do not have a preferred cleaving plane. Hence, while the surface sensitivity of TEY can be a benefit for systems that can be prepared cleanly, it can also hinder the interpretation of XAS measurements in many scenarios.

In addition to surface contamination, it is possible for surface charging effects to exist in insulating materials.[46, 47, 48, 49] These effects arise due to the considerably different properties of electron mobility in insulators which lead to strong electric fields at the surface of the sample.[46, 50] In insulators, the electron escape depth can reach up to a few hundred Å since electron-electron scattering is not as effective at low kinetic energies.[45] This has direct implications on the condition that $\lambda_x \gg \lambda_e$ for TEY to obtain its proportionality to $E\mu(E)$. Moreover, because of the low electrical conductance of insulators, filling in vacancies using an electrical ground is not always effective. As a result, measuring TEY by the standard drain current approach can be unreliable. This charging effect is exacerbated by increasing the thickness of the samples, as shown in Ref. [46], and can be mitigated by the use of very thin samples.

As a consequence of these surface effects, the interpretation of TEY data must be approached with a certain caution. The use of fluorescence yield is one common approach to checking that TEY spectra are representative of the bulk. However, FY spectra are typically distorted by saturation effects, so the comparison is not as instructive as one might hope. Varying the experimental geometry changes the information depth of the measurement, so this can be used as well to enhance the interpretation of the measurement. Nevertheless, there are scenarios (eg. thick, concentrated insulators) where surface effects combine with saturation effects to make both TEY and TFY measures unreliable, and where alternatives are desperately needed.

Chapter 3

Principles of Inverse Partial Fluorescence Yield

3.1 Partial fluorescence yield

In section 2.2, we developed an expression for the TFY. The IPFY expression follows directly from Eq. (2.4), but it relies on the extraction a partial fluorescence yield. Using an energy-sensitive photon detection scheme, it is possible to extract a single PFY term since characteristic x-rays produced by electrons filling in different core hole states have unique emission energies.[6, 16] The PFY from a given atomic core state Y, is then simply defined as

$$\frac{I(E_i, E_f)}{I_0(E_i)} = \eta(E_f)\frac{\Omega}{4\pi}\frac{\omega_Y(E_i, E_f)\mu_Y(E_i)}{\mu(E_i) + \mu(E_f)\frac{\sin\alpha}{\sin\beta}}. \tag{3.1}$$

In a material that has multiple core states, either arising from different elements or simply because of the different energy levels of the atom, the particular selection of Y can have a significant impact on Eq. (3.1). The key differentiating factor, it turns out, is whether the x-ray emission from core state Y is *resonant* or *non-resonant*.

3.1.1 Resonant PFY

In general, if one selects an atomic core state Y such that the emission energy is near the absorption edge energy, resonant processes in both $\omega(E_i, E_f)$ and $\mu_Y(E_i)$ lead to strong

saturation effects which distort the PFY. We can illustrate this crucial aspect of Eq. (3.1) with a specific example.

Consider an XAS measurement of NiO across the Ni L_3 edge (855 eV). Absorption at the Ni L_3 edge corresponds to exciting an electron in the $2p_{3/2}$ state into an unoccupied state and leaving behind a $2p_{3/2}$ core hole. Electrons lying in $3d_{5/2}$, $3d_{3/2}$ and $3s$ states can then transition into this core hole producing Ni L_{α_2}, Ni L_{α_1} and Ni L_ℓ emission lines, respectively. The PFY arising from the Ni L_α emission line (the Ni L_{α_2} and Ni L_{α_1} lines are not distinguishable) can be written as

$$\frac{I(E_i, E_f)}{I_0(E_i)} = \eta(E_f)\frac{\Omega}{4\pi}\frac{\omega_{\mathrm{Ni}_{L_\alpha}}(E_i, E_f)\mu_{\mathrm{Ni}_{L_3}}(E_i)}{\mu_{\mathrm{tot}}(E_i) + \mu_{\mathrm{tot}}(E_f)\frac{\sin\alpha}{\sin\beta}}. \tag{3.2}$$

Note here that I have explicitly included the "tot" subscript to $\mu_{\mathrm{tot}}(E_i)$ and $\mu_{\mathrm{tot}}(E_f)$, where $\mu_{\mathrm{tot}}(E) = \mu_{\mathrm{Ni}_{L_3}}(E) + \mu_{\mathrm{other}}$ and μ_{other} is the sum of the absorption coefficients which have edge steps at a lower energy than the Ni L_3 edge.[1]

Across the Ni L_3 edge, the absorption coefficient jumps due to $\mu_{\mathrm{Ni}_{L_3}}(E)$ while μ_{other} gradually decreases. The fluorescence photons emit from the Ni $L_{\alpha_{1,2}}$ transition at an energy of 851.5 eV, slightly lower than the absorption edge. With these considerations, Eq. (2.6) can be written as

$$\frac{I(E_i, 851.5\text{ eV})}{I_0(E_i)} \propto \frac{\omega_{\mathrm{Ni}_{L_\alpha}}(E_i, 851.5\text{ eV})\mu_{\mathrm{Ni}_{L_3}}(E_i)}{\mu_{\mathrm{Ni}_{L_3}}(E_i) + \mu_{\mathrm{other}}(E_i) + \mu_{\mathrm{tot}}(851.5\text{ eV})\frac{\sin\alpha}{\sin\beta}}. \tag{3.3}$$

There are two essential features of Eq. (3.3) which must be noted. Firstly, the term $\omega_{\mathrm{Ni}_{L_\alpha}}(E_i, 851.5\text{ eV})$ is not simple to calculate. The probability to emit a photon at 851.5 eV when E_i is near the Ni L_3 absorption edge depends strongly on E_i and the local electronic configuration of the Ni atom. Secondly, in both the numerator and denominator, the term $\mu_{\mathrm{Ni}_{L_3}}(E_i)$ appears. This term increases drastically in the XANES region of the absorption edge. As a result, $\mu_{\mathrm{Ni}_{L_3}}(E_i)$ can become considerably larger than the other terms in the denominator and the $\mu_{\mathrm{Ni}_{L_3}}(E_i)$ terms approximately cancel one another. This cancellation results in loss of proportionality to $\mu_{\mathrm{tot}}(E)$, and appears in resonant PFY spectra as a strong saturation effect.

[1] In NiO, this theoretically consists of the Ni M_1 edge (111.8 eV), the Ni $M_{2,3}$ edge (68.1 eV) the Ni $M_{4,5}$ edge (3.6 eV), the O K edge (532 eV), the O L_1 edge (23.7 eV) and the O $L_{2,3}$ edge (7.1 eV).[35]

3.1.2 Non-resonant PFY

If one instead selects Y such that the emission energy is well separated from the absorption edge energy (ie. a *non-resonant* process), the form of Eq. (3.1) changes considerably. Following along with our earlier example of NiO x-ray absorption across the L_3 edge, but instead choosing the PFY arising from the O K_α emission, we find that

$$\frac{I(E_i, 524.9 \text{ eV})}{I_0(E_i)} \propto \frac{\omega_{\text{O}_{K_\alpha}}(E_i, 524.9 \text{ eV})\mu_{\text{O}_K}(E_i)}{\mu_{\text{Ni}_{L_3}}(E_i) + \mu_{\text{other}}(E_i) + \mu_{\text{tot}}(524.9 \text{ eV})\frac{\sin\alpha}{\sin\beta}}. \tag{3.4}$$

The situation in Eq. (3.4) is quite different than that found in Eq. (3.3). In this case, the incident photon energy $E_i \sim 855$ eV is substantially higher than $E_f = 524.9$ eV. Consequently, the probability of fluorescence occurring depends only weakly on E_i, and $\omega_{\text{O}_{K_\alpha}}(E_i, 524.9 \text{ eV})$ can be treated as approximately constant. Moreover, $\mu_{\text{O}_K}(E_i)$ has no absorption edge around E_i, so it is a smoothly varying function of energy. Hence, the saturation problem that exists with resonant PFY – by approximate cancellation of $\mu_{\text{Ni}_{L_3}}$ in the numerator and $\mu_{\text{tot}}(E)$ in the denominator – is not present in the case of non-resonant x-ray emission.

Additionally, inspection of Eq. (3.4) reveals that the denominator will increase more than the numerator across the L_3 absorption edge. Hence, this expression predicts that one should see a *decrease* in the detected non-resonant PFY intensity when the total x-ray absorption coefficient *increases.*

3.2 Inverse partial fluorescence yield

A simple inversion of Eq. (3.1) for *non-resonant* PFY defines the inverse partial fluorescence yield:

$$\text{IPFY} = \frac{I_0(E_i)}{I(E_i, E_f)} = \frac{1}{\eta(E_f)\frac{\Omega}{4\pi}\omega_Y(E_i, E_f)\mu_Y(E_i)}\left(\mu(E_i) + \mu(E_f)\frac{\sin\alpha}{\sin\beta}\right). \tag{3.5}$$

Inspection of Eq. (3.5) indicates that by careful consideration of the pre-factors, IPFY has the potential to be a measure of $\mu_{\text{tot}}(E)$. I will show that by either making some simple approximations or by exploiting the geometry dependence of IPFY, one can derive $\mu_{\text{tot}}(E)$ from an IPFY measurement.

3.2.1 Approximations

The first approximation one can make is that $\omega_Y(E_i, E_f) \approx \omega_Y$. As mentioned earlier, if E_f is considerably lower than E_i, the fluorescence probability is nearly independent of E_i. This is simply because the core electron is readily ejected into the continuum and imparting slightly different amounts of kinetic energy to this electron has little bearing on whether the atom will subsequently decay radiatively instead of non-radiatively. Conversely, if E_i and E_f are similar, it is possible for the core electron to be transferred into empty atomic states rather than the continuum. These transitions between atomic states have different fluorescence probabilities than transitions between the continuum and core hole states.[28]

The second approximation that one can make is that $\mu_Y(E_i) \approx \mu_Y$. If the energy range of the measurement is narrow and the energy dependence of $\mu_Y(E_i)$ over this range is small, then this approximation is reasonable. Clearly, this approximation is material and case specific, but in practice can often be acceptable. See section 4.2.1.4 for a detailed analysis of the validity of this approximation.

Implementing both of these approximations, we find that IPFY can be expressed as

$$\text{IPFY} = \frac{I_0(E_i)}{I(E_i, E_f)} \approx \frac{1}{\eta(E_f)\frac{\Omega}{4\pi}\omega_Y \mu_Y} \left(\mu(E_i) + \mu(E_f) \frac{\sin\alpha}{\sin\beta} \right). \tag{3.6}$$

The term outside the brackets can then be treated approximately as a constant. Consequently, IPFY from a non-resonant emission and over a narrow energy range is *linearly proportional* to $\mu_{\text{tot}}(E)$.

3.2.2 Geometry dependence

Over a wide energy range, the approximation that $\mu_Y(E_i) \approx \mu_Y$ made in section 3.2.1 does not hold. Additionally, the quantum efficiency of the $I_0(E_i)$ measurement made by the gold grid can vary significantly if the energy range is wide. Fortunately, it is possible to account for both energy dependencies by measuring IPFY with two different experimental geometries.

First, the I_0 measurement from the grid is written as $I_{\text{Grid}}(E_i) = I_0(E_i)\nu_{\text{Grid}}(E_i)$ to separate the energy dependence resulting from $\nu_{\text{Grid}}(E_i)$, the quantum efficiency of the grid, from the energy dependence of $I_0(E_i)$, the true incident photon intensity. The IPFY expression Eq. (3.5) is then modified by replacing I_0 with I_{Grid}

$$\text{IPFY} = \frac{I_{\text{Grid}}(E_i)}{I(E_i, E_f)} = \frac{I_0(E_i)\nu_{\text{Grid}}(E_i)}{I(E_i, E_f)}. \tag{3.7}$$

It follows from Eq. (3.7) that

$$\begin{aligned}\text{IPFY} &= \frac{\nu_{\text{Grid}}(E_i)}{\eta(E_f)\frac{\Omega}{4\pi}\omega_Y(E_i,E_f)\mu_Y(E_i)}\left(\mu(E_i)+\mu(E_f)\frac{\sin\alpha}{\sin\beta}\right) \\ &= A(E_i)\left(\mu(E_i)+\mu(E_f)\frac{\sin\alpha}{\sin\beta}\right) \qquad (3.8)\end{aligned}$$

For simplicity, we will refer to the energy dependent factor outside the brackets as $A(E_i)$.[2] Now, consider that we have two measurements of IPFY recorded with different experimental geometries. We will denote the first set of angles by j and the second set by k. If we calculate IPFY_j - IPFY_k from Eq. (3.8), we find that

$$\text{IPFY}_j - \text{IPFY}_k = A(E_i)\mu(E_f)\left(\frac{\sin\alpha_j}{\sin\beta_j} - \frac{\sin\alpha_k}{\sin\beta_k}\right). \qquad (3.9)$$

Note that the $\mu(E_i)$ terms cancel in this subtraction.[3] Rearranging Eq. (3.9), we find that

$$\begin{aligned}A(E_i) &= \frac{1}{\mu(E_f)}\frac{\text{IPFY}_j - \text{IPFY}_k}{\frac{\sin\alpha_j}{\sin\beta_j} - \frac{\sin\alpha_k}{\sin\beta_k}} \\ &= \frac{1}{\mu(E_f)}S_{j,k}(E_i). \qquad (3.10)\end{aligned}$$

We define the term $S_{j,k}(E_i)$ as shown in Eq. (3.10) for notational convenience. Now, Eq. (3.10) gives an explicit way to determine $A(E_i)$ experimentally by varying the geometry. Substituting Eq. (3.10) into Eq. (3.8) leads to

$$\text{IPFY} = S_{j,k}(E_i)\left(\frac{\mu(E_i)}{\mu(E_f)} + \frac{\sin\alpha}{\sin\beta}\right). \qquad (3.11)$$

Since it is possible to determine $S_{j,k}(E_i)$ purely from experimental data, we can effectively rearrange Eq. (3.11) and find that

$$\frac{\mu(E_i)}{\mu(E_f)} = \frac{\text{IPFY}}{S_{j,k}(E_i)} - \frac{\sin\alpha}{\sin\beta}. \qquad (3.12)$$

[2]We have dropped the dependence on E_f because in practice one selects a single emission energy and keeps it fixed. Consequently, E_i is the only effective variable in the factor outside the brackets in Eq. (3.8)

[3]This requires that $\mu(E_i)$ does not have a geometry dependence. In the XANES region, dichroism effects can modify $\mu(E_i)$. However, far from absorption peaks, the absorption is typically not geometry dependent and the cancellation is valid.

3.3 Implications

Equations (3.6) and (3.12) have significant implications. Over a narrow energy range, IPFY is approximately linearly proportional to $\mu_{\text{tot}}(E)$, without the need for any correction techniques or analysis. Over a wide energy range, however, one may exploit the angle dependence of IPFY to obtain a measure of XAS that is *directly proportional* to $\mu_{\text{tot}}(E)$ without any complicated offsets or scaling parameters.[4] $S_{j,k}(E_i)$ is easily obtained experimentally, $\frac{\sin\alpha}{\sin\beta}$ is calculated based on the experimental setup (see Appendix A) and $\mu(E_f)$ can be taken from tabulated data or calculations. Due to the reliance on photon detection with IPFY, bulk sensitivity in the measurement is preserved.

Moreover, it is clear from Eqs. (3.6) and (3.12) that there are *no saturation effects* associated with this measure of $\mu_{\text{tot}}(E)$. This is because a non-resonant Y is selected in the derivation of this expression, so approximate cancellation of $\mu(E_i)$ and $\mu_Y(E_i)$ never occurs. Compared to TEY, TFY or resonant PFY which require non-trivial corrections for saturation effects,[5] this measure of $\mu_{\text{tot}}(E)$ relies on a simple analysis with inputs that come entirely from experimental data.

[4] The same analysis is possible in a narrow energy range and can be applied to account for small variations in $\mu_Y(E_i)$ and $\nu_{\text{Grid}}(E_i)$.

[5] As covered in sections 2.4.2.1 and 2.4.2.2, these techniques make assumptions about the sample stoichiometry, the escape depth of electrons in the material or about the behaviour of μ_{other}.

Chapter 4

Experimental Demonstrations of IPFY

4.1 Measurement details

The experimental work detailed in this chapter was performed at the Canadian Light Source's High Resolution Spherical Grating Monochromator (SGM) 11ID-1 beamline and the Soft X-ray Microcharacterization Beamline (SXRMB) 06B1-1. The Canadian Light Source (CLS) is a third-generation 2.9 GeV synchrotron. It uses a linear accelerator to accelerate electrons to 200-250 MeV at which point they are inserted into a booster ring to increase the electron energy up to 2.9 GeV. At 2.9 GeV, the electrons are injected into a storage ring. It should be noted that at this energy the electrons are ultra relativistic ($v/c \approx 0.999999985$) and lose energy in the form of Bremsstrahlung radiation. Experimental beamlines are attached to the storage ring. They are designed either to use the Bremsstrahlung radiation directly or to utilize undulators to obtain finer control over the properties of the produced photons.

The SGM beamline uses a 45mm planar undulator to produce highly directional and horizontally polarized radiation from the electrons in the storage ring. Using a series of mirrors, spherical gratings and a variable exit slit (see Fig. 4.1), x-rays can be monochromated to a resolution characterized by $E/\Delta E > 5000$ over an energy range of 250 eV to 1500 eV and typically obtaining a photon flux of $10^{11} - 10^{12}$ (photons/s/0.1%BW) with a storage ring current of 100 mA.[1]

[1] Normal operations are typically at a ring current of 250 mA, so flux is in practice better than specified. BW refers to the beam width, indicating that flux here is a measure of photons/s/length.

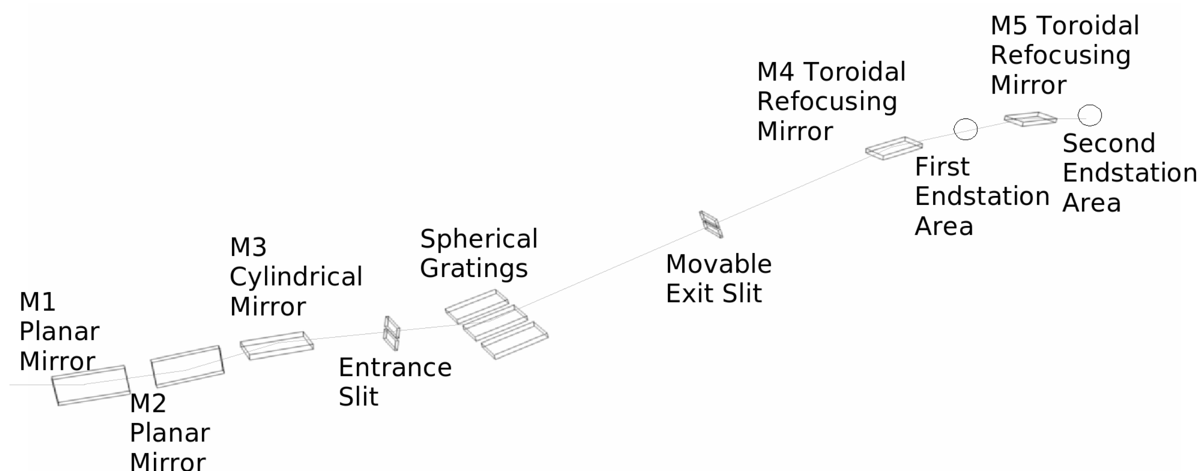

Figure 4.1: A schematic representation of optical elements at the SGM beamline.[51] (Figure reprinted with permission)

SGM features a solid sample analysis endstation (SSA) capable of collecting XAS spectra by the TEY, TFY and PFY techniques. TEY is measured in the drain current mode using a picoammeter, TFY is measured on a microchannel plate (MCP) detector and the PFY is measured using a silicon drift detector (SDD). Pressures in this chamber typically range between 10^{-7} Torr and 10^{-9} Torr. The SSA endstation at the SGM beamline was thus a suitable choice for the comparison of various experimental techniques at soft x-ray energies.

4.2 IPFY spectroscopy

To evaluate the merits of IPFY and to test the theoretical predictions made in Chapter 3, we will present XAS measurements of NiO and $NdGaO_3$ by means of TEY, PFY (resonant and non-resonant) and IPFY. As we have already developed theoretical expressions to illustrate the principles of IPFY spectroscopy using NiO as an example (see sections 3.1.1 and 3.1.2), we will begin by examining the experimental results for NiO.

4.2.1 NiO

We measured XAS at SGM on a single crystal of NiO at the Ni $L_{3,2}$ edge. This crystal was obtained from Princeton Scientific Corporation who specified that it was polished to a surface roughness less than 0.03 μm, had dimensions of 5 mm $\times$ 5 mm $\times$ 0.5 mm and was oriented such that the $\langle 100 \rangle$ direction was normal to the sample surface. NiO is an interesting case for benchmarking XAS using various techniques because it is insulating, has concentrated elements, and has well-separated resonant and non-resonant emission lines in the soft x-ray region.[34, 52, 53, 54]

4.2.1.1 X-ray fluorescence and PFY

In order to measure the PFY, an energy-discriminating silicon drift detector was used. The SDD allows us to measure an x-ray emission spectrum (XES) at each incident photon energy. As we collect an XES at each photon energy, our raw data is in the form of a matrix with x-ray emission on the vertical axis and incident photon energy on the horizontal axis. These will be presented as images which we will refer to as x-ray fluorescence (XRF) plots. PFY will refer to x-ray absorption data that has been extracted from an XRF dataset.

The left panel of Fig. 4.2 shows the XRF of NiO and the right panel shows the XES extracted from the the pre- and post-edge regions of the XRF. Figure 4.2 illustrates many important features that were discussed earlier in a purely theoretical framework:

1. We observe a number of x-ray emission lines[2] which can be classified as
   - Resonant:
     Ni L_{β_1} emission at 868.8 eV ($M_4 \rightarrow L_2$)
     Ni $L_{\alpha_{1,2}}$ emission at 851.5 eV ($M_{5,4} \rightarrow L_3$)
     Ni L_η emission at 762.0 eV ($M_1 \rightarrow L_2$)
     Ni L_ℓ emission at 742.7 eV ($M_1 \rightarrow L_3$)
   - Non-resonant:
     O K_{α_1} emission at 524.9 eV ($L_3 \rightarrow K$)
2. The resonant Ni L emission intensity is nearly zero before the L_3 absorption edge ($\sim$ 853.6 eV) and grows rapidly evolving into the complex x-ray absorption near edge structure (XANES).

[2] Broadened by $\sim$ 130 eV because of the limited energy resolution of the SDD detector.

3. The non-resonant O K emission is smoothly varying up until the absorption edge, at which point the emission intensity *decreases* with structure that appears inversely related to the increase in the absorption due to the Ni $L_{3,2}$ absorption edge.

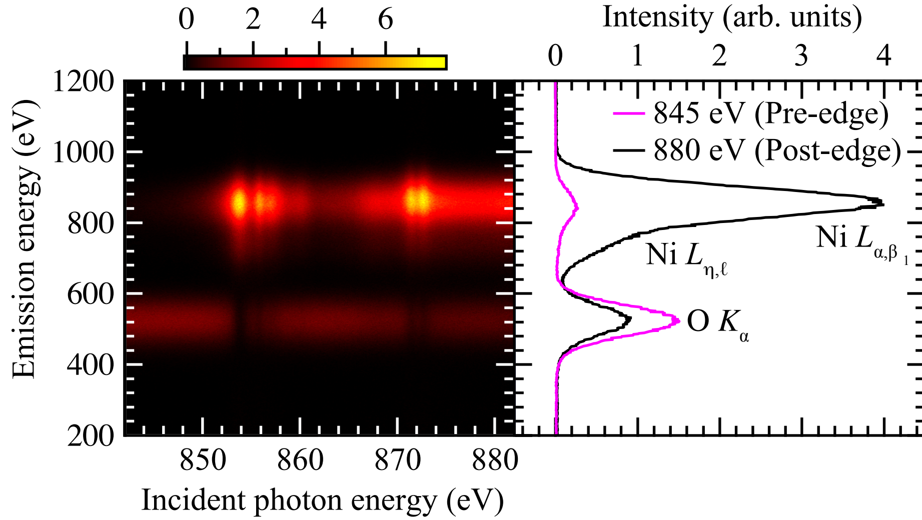

Figure 4.2: The normalized x-ray fluorescence of NiO across the Ni L_3 and Ni L_2 edges is shown in the left panel. The top band corresponds to the resonant Ni L_{α,β_1} and Ni $L_{\eta,\ell}$ emission processes. The bottom band corresponds to non-resonant O K_α emission. The right panel demonstrates the x-ray emission spectra of the pre- and post-edge regions at incident photons energies of 845 eV and 880 eV (extracted by averaging over 1 eV windows centered at these energies). This data was collected at normal incidence.

In Fig. 4.3(a), we show the extracted resonant and non-resonant PFY from the XRF data. Here we used 150 eV windows, approximately matched to the energy resolution of the SDD, centered at the Ni L resonant and O K non-resonant emission energies. Note that for the O K emission, this window does not pick up a significant contribution from any emission other than O. For the Ni L emission, this window includes some contribution from Ni $L_{\eta,\ell}$ emission. However, the Ni $L_{\eta,\ell}$ emission has structure that closely follows the resonant emission, so the effect of this averaging is found to be small. Here we can see that the resonant PFY has XANES-like structure, while the non-resonant PFY exhibits dips at positions corresponding to increases in $\mu_{\text{tot}}(E)$. This is consistent with the earlier interpretations of Eq. (3.3) for resonant PFY and Eq. (3.4) for non-resonant PFY. It follows from Eq. (3.6) that the inverse of the non-resonant PFY should be approximately

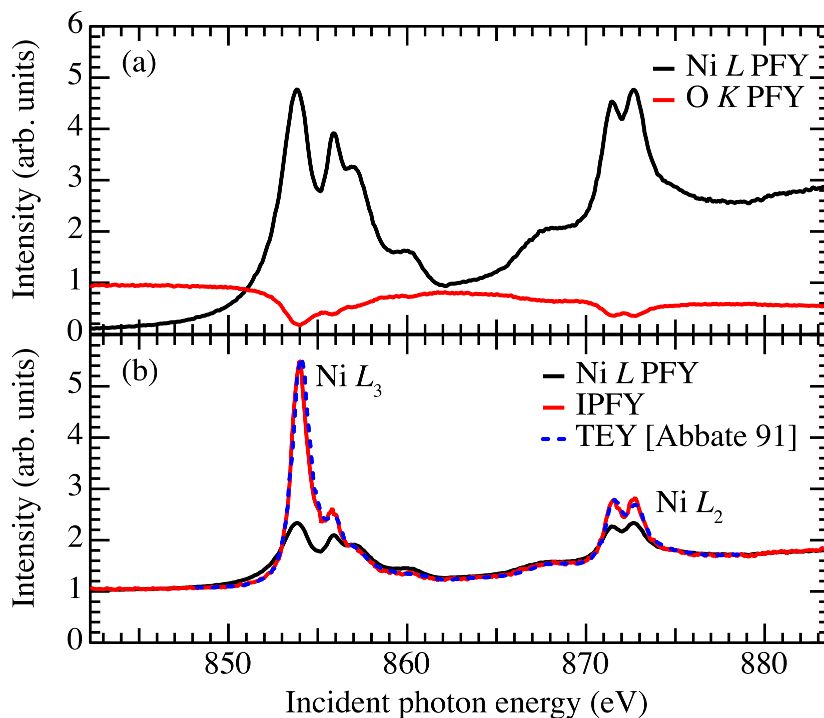

Figure 4.3: (a) The Ni L and O K PFY extracted from the XRF data in Fig. 4.2. The Ni L PFY shows XANES-like structure while the O K PFY exhibits dips that are inversely related to increases in $\mu_{\text{tot}}(E)$. (b) The IPFY is compared to the Ni L PFY and TEY data on NiO from literature.[52] The Ni L PFY shows a very strong saturation effect at the L_3 peak, whereas the IPFY and TEY data from literature are in excellent agreement.

linearly proportional to $\mu_{\text{tot}}(E)$ since the data here are collected over a narrow energy range. Inverting the non-resonant O K PFY from Fig. 4.3(a), we obtain the spectrum shown in red in Fig. 4.3(b).

4.2.1.2 IPFY in the XANES region

In Fig. 4.3(b) the inverse of the non-resonant O K PFY (ie. the IPFY) is compared to the Ni L PFY and TEY data from literature (known to accurately reflect the x-ray absorption for NiO).[52] The IPFY and TEY data are in excellent agreement, indicating that the IPFY is an accurate measure of the x-ray absorption coefficient over this narrow energy

range. In contrast, the Ni L PFY is in very poor agreement, demonstrating how strong saturation effects can be for elements with high concentrations such as Ni in NiO. The Ni L_3 XANES, where absorption is highest and the saturation effect is strongest, bears little proportionality to the x-ray absorption coefficient. Note that the experimental geometry in this measurement represents a general case which is neither at the limit of zero saturation nor total saturation ($\alpha = 90°, \beta = 41.6°$). It should also be noted that the spectra were scaled and offset to agree in the pre- and post-edge in Fig. 4.3(b).

One of the features of the IPFY [see Eq. (3.6)] is that the pre-factor and $\mu(E_f)\frac{\sin\alpha}{\sin\beta}$ should be approximately independent of E_i over a narrow energy range. This suggests that varying the experimental geometry should only modify the term $\mu(E_f)\frac{\sin\alpha}{\sin\beta}$. In contrast, with resonant PFY, it is expected that changing α and β will influence the magnitude of saturation effects. To test this hypothesis, we measured an XRF spectrum of NiO at six different angles of incidence. The XRF data is qualitatively similar to that shown in Fig. 4.2 and is not reproduced here. The extracted Ni L PFY and O K IPFY spectra from these XRF spectra, however, are shown in Fig. 4.4(a) and 4.4(b).

4.2.1.3 Geometry effects in PFY and IPFY

The resonant Ni L PFY shows strong saturation effects for all six geometries [Fig. 4.4(a)], in accordance with Eq. (3.3). For instance, the intensity of the main L_3 peak at 853.8 eV does not change considerably as the geometry is varied. However, the secondary L_3 peak and the L_2 peak exhibit drastic variations in intensity. This indicates that the signal has saturated at the L_3 peak, where the x-ray absorption cross-section is highest. Moreover, the general trend we observed agrees with our understanding of the saturation effect. As $\frac{\sin\alpha}{\sin\beta}$ decreases (highest for dark blue line, lowest for pink line), the impact of the $\mu(E_f)\frac{\sin\alpha}{\sin\beta}$ term in the denominator of Eq. (3.3) becomes smaller and competes less with the $\mu_{\text{tot}}(E_i)$ term, leading to increased cancellation and increased saturation.

The non-resonant O K IPFY spectra, on the other hand, exhibit much simpler behaviour as the geometry is varied—they are offset from one another due to the change in $\frac{\sin\alpha}{\sin\beta}$. The inset of Fig. 4.4(b) shows the linear dependence of the IPFY spectra on $\frac{\sin\alpha}{\sin\beta}$ at an incident photon energy of $E_i = 845$ eV. This comes directly from Eq. (3.6), which can

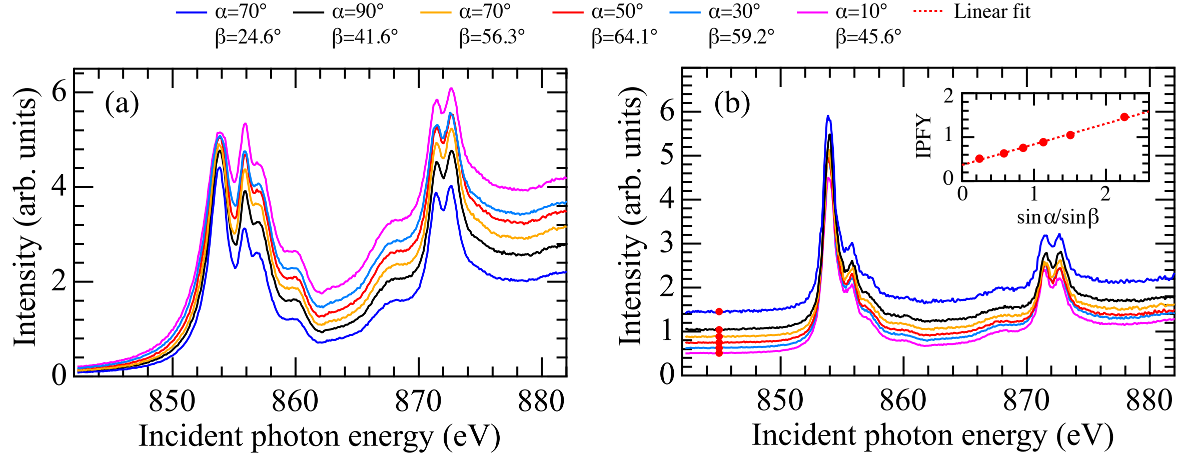

Figure 4.4: (a) The Ni L PFY measured at the indicated values of α and β. The saturation effect gets worse as the geometry is varied from a near normal incidence, grazing takeoff geometry (dark blue) towards a grazing incidence, 45° takeoff geometry (pink line). (b) The IPFY, extracted from the same XRF spectra at the same angles, are simply offset from one another. Notably, there are no strong distortions of the spectra as the geometry is varied. The inset shows the IPFY value at 845 eV as a function of $\frac{\sin\alpha}{\sin\beta}$, demonstrating that the offset depends linearly on $\frac{\sin\alpha}{\sin\beta}$.

be written as

$$\begin{aligned} \mathrm{IPFY}_j &\approx a + b\frac{\sin\alpha_j}{\sin\beta_j} \\ a &= \frac{\mu(E_i)}{\eta(E_f)\frac{\Omega}{4\pi}\omega_Y\mu_Y} \\ b &= \frac{\mu(E_f)}{\eta(E_f)\frac{\Omega}{4\pi}\omega_Y\mu_Y}, \end{aligned} \tag{4.1}$$

where j denotes the geometry of a given experiment. According to Eq. (4.1), a linear fit to the IPFY_j intensity as a function of $\frac{\sin\alpha_j}{\sin\beta_j}$ has an intercept of a and a slope of b. Re-arranging Eq. (4.1), we find that

$$\frac{\mathrm{IPFY}_j}{b} - \frac{\sin\alpha_j}{\sin\beta_j} \approx \frac{a}{b} \approx \frac{\mu(E_i)}{\mu(E_f)}. \tag{4.2}$$

The ratio $\frac{\sin\alpha}{\sin\beta}$ can be calculated generally according to Eq. (4.3), which is derived in Appendix A. In Eq. (4.3), the angles $\theta_s, \phi_s, \theta_d$ and ϕ_d define the azimuthal (θ) and polar (ϕ) rotation angles representing the norm of the sample (s) and the direction of the detector (d), respectively. At the SGM beamline's SSA endstation, the SDD position is given by $\theta_d = 42.5°, \phi_d = 25.8°$. The samples were mounted such that $\phi_s = 0$ and θ_d was varied between measurements by means of a motorized rotation stage. Table 4.1, shows the calculated angles and their estimated uncertainties [see Eqs. (A.15), (A.16) and (A.17)].

$$\frac{\sin\alpha}{\sin\beta} = \frac{\cos\theta_s}{\cos(\phi_d)\cos(\theta_d - \theta_s) + \sin(\phi_d)\tan(\phi_s)} \tag{4.3}$$

Table 4.1: Experimental angles α, β and $\frac{\sin\alpha}{\sin\beta}$ for the SDD at the SGM beamline's SSA endstation. Standard deviations are calculated assuming that $\theta_s, \phi_s, \theta_d$ and ϕ_d are known to within $\pm 0.5°$.

θ_s (°)	α (°)	β (°)	$\frac{\sin\alpha}{\sin\beta}$
-20 ± 0.5	70 ± 0.5	24.6 ± 0.7	2.26 ± 0.05
-10 ± 0.5	80 ± 0.5	33.2 ± 0.7	1.80 ± 0.03
0 ± 0.5	90 ± 0.5	41.6 ± 0.7	1.51 ± 0.02
10 ± 0.5	80 ± 0.5	49.4 ± 0.7	1.30 ± 0.01
20 ± 0.5	70 ± 0.5	56.3 ± 0.7	1.13 ± 0.01
30 ± 0.5	60 ± 0.5	61.5 ± 0.7	0.985 ± 0.009
40 ± 0.5	50 ± 0.5	64.1 ± 0.7	0.851 ± 0.008
50 ± 0.5	40 ± 0.5	63.2 ± 0.7	0.720 ± 0.008
60 ± 0.5	30 ± 0.5	59.2 ± 0.7	0.582 ± 0.008
70 ± 0.5	20 ± 0.5	53.0 ± 0.7	0.428 ± 0.009
80 ± 0.5	10 ± 0.5	45.6 ± 0.7	0.24 ± 0.01

Using the linear fit shown in the inset of Fig. 4.4(b), we apply Eq. (4.2) to the IPFY spectra collected for the six different experimental angles. This provides $\mu(E_i)/\mu(E_f)$, which we can scale using a tabulated value for $\mu(E_f)$ from Ref. [55] (ie. $\mu(E_f) = 3.14 \times 10^6$ m^{-1} for stoichiometric NiO with a density of 6.67 g/cm^3). Having applied this correction, we find that the spectra collapse onto a single curve (Fig. 4.5).[3]

[3] The discrepancies seen at the peaks of the Ni L_3 and L_2 edges can be attributed to x-ray magnetic linear dichroism in NiO. The Ni spins in NiO order antiferromagnetically in the (111) plane giving rise to the observed XMLD.[34]

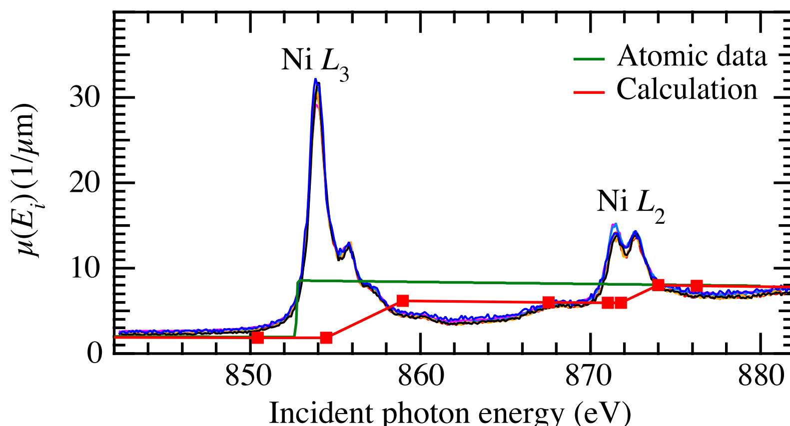

Figure 4.5: The IPFY spectra shown in Fig. 4.4(b) are corrected according to Eq. (4.2) and scaled to $\mu(E_f)$. The spectra collapse onto a single curve and the magnitude of the edge step agrees with tabulated atomic data and atomic calculations.[55, 35]

Moreover, the magnitude of the edge step agrees quantitatively with tabulated atomic data and calculations from Refs. [55] and [35], respectively.[4] Note that these tabulated values are representative of absorption due to free atoms excited into the continuum and completely miss the XANES structure observed experimentally for NiO.[5]

The success of this straightforward analysis illustrates the power of IPFY spectroscopy for measurements performed over narrow energy ranges, such as in XANES studies. Measurement of IPFY at a few angles (as few as two, but preferably more) enables the general determination of $\mu(E_i)/\mu(E_f)$ in the XANES region of most x-ray absorption edges. If sample stoichiometry is known, then a simple calculation of $\mu(E_f)$ from tables provides a measure of $\mu(E_i)$.

4.2.1.4 Verifying the validity of our approximations

Before moving on to the analysis of IPFY data over a wide energy range it would be useful to verify the appropriateness of the approximations used in this near-edge analysis. In

[4]The tables contained in these papers are conveniently made available electronically via the NIST and CXRO websites.[56, 57]

[5]In the case of the tabulated data, measurements on pure solid Ni and gaseous O have been extrapolated from outside the EXAFS region into the near-edge region. The calculations are based purely on the absorption due to free atoms.

deriving Eq. (4.2), we assumed that the variations with energy of $\mu_Y(E_i)$ and $\nu(E_i)$ were negligible over the covered energy range. It might be more appropriate actually to say that the *combined effect* of both variations should be negligible for the approximate IPFY expression to be valid.

Simple estimates for the individual variations can be made by using tabulated absorption data for O and Au, since both elements have no absorption edges in the 840 - 880 eV range. For O, we find that $\mu_{\mathrm{O}}(840\mathrm{eV}) \approx 0.0010\mu\mathrm{m}^{-1}$ and $\mu_{\mathrm{O}}(880\mathrm{eV}) \approx 0.0009\mu\mathrm{m}^{-1}$. For μ_{O} alone, the fractional change is $\sim$11%. The quantum efficiency of the Au grid, $\nu(E_i)$, is mostly determined by the absorption of Au, so a similar estimate can be made. For Au, we find that $\mu_{\mathrm{Au}}(840\mathrm{eV}) \approx 14\mu\mathrm{m}^{-1}$ and $\mu_{\mathrm{Au}}(880\mathrm{eV}) \approx 13\mu\mathrm{m}^{-1}$, corresponding to a fractional change of $\sim$7.7% for Au alone.

These numbers seem large individually. However, the $\mu_{\mathrm{Y}}(E_i)$ and $\nu(E_i)$ are not multiplicative—they appear as a fraction in the IPFY expression. Their combined effect must be estimated to get a true sense of the appropriateness of our approximations. In between 840 eV and 880 eV, both $\mu_{\mathrm{O}}(E_i)$ and $\mu_{\mathrm{Au}}(E_i)$ are smoothly varying functions. Because of the narrow energy range, these variables are well approximated by straight line. Hence, assuming that both of these variables vary approximately linearly between 840 eV and 880 eV, we can factor these variations into Eq. (4.2). Doing so, we find that $\mu(E_i)/\mu(E_f)$ now has the approximate form

$$\begin{aligned} \frac{\mu(E_i)}{\mu(E_f)} &\approx \frac{\mathrm{IPFY}_j}{b}\left(\frac{\mu_{\mathrm{O}}(E_i)}{\mu_{\mathrm{Au}}(E_i)}\right) - \frac{\sin\alpha_j}{\sin\beta_j} \\ \frac{\mu(E_i)}{\mu(E_f)} &\approx \frac{\mathrm{IPFY}_j}{b}\left(\frac{\frac{0.0009-0.001}{880-840}(E_i-840)+0.001}{\frac{13-14}{880-840}(E_i-840)+14}\right) - \frac{\sin\alpha_j}{\sin\beta_j}. \end{aligned} \tag{4.4}$$

The fractional change of the term in brackets is now a reasonable estimate for the deviation of the approximate IPFY expression over the considered energy range. In this simple approximation, we find that the variation is on the order of 3-4% between 840 eV and 880 eV. This is significantly less in magnitude than the individual fractional changes calculated for $\mu_{\mathrm{Y}}(E_i)$ and $\nu(E_i)$. This is because their energy dependencies nearly cancel one another out in this instance.

Of course, this is just one of many ways that one can estimate the error in the analysis. If instead of performing just a single line fit at $E_i = 845$ eV, we perform a line fit at all off-peak incident photon energies, we can directly measure the effects discussed above. Doing so, we find that there are gradual changes in the fit parameter b with energy. This energy dependence is related to the ratio $\frac{\mu_{\mathrm{Au}}(E_i)}{\mu_{\mathrm{O}}(E_i)}$, but also includes more complicated parameters

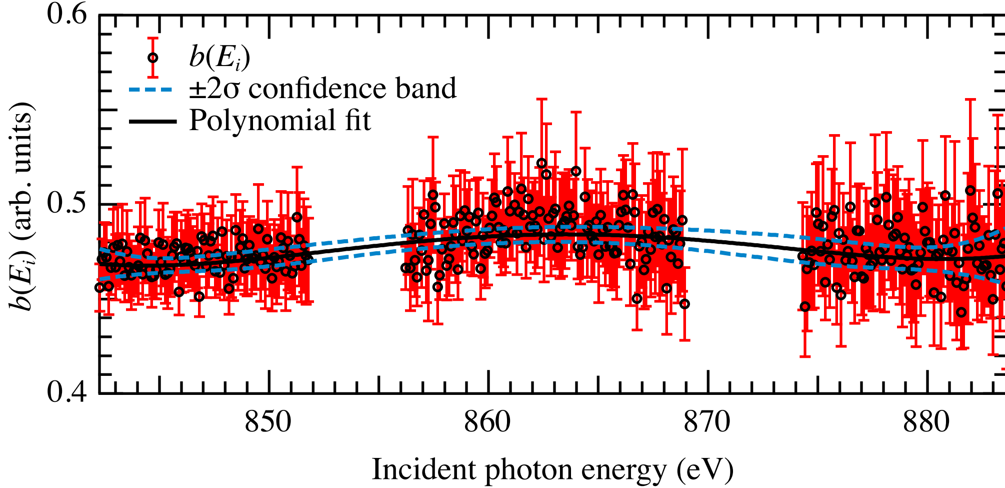

Figure 4.6: Linear fits based on Eq. (4.1) are performed for all off-peak E_i. The fit parameter $b(E_i)$ exhibits a gradual variation with energy. A polynomial fit (black) and $\pm 2\sigma$ confidence band (dashed blue) show that the variation of $b(E_i)$ is at most 5.5% for the entire energy range. The peak regions are left out of the analysis since the XMLD of NiO affects the peak intensities as the geometry is varied.

related to the true (ie. measured experimentally) quantum efficiency of the grid as well as the absorption of O in NiO. The energy dependence of $b(E_i)$ allows, in principle, for one to divide out all the energy dependence of the pre-factors. In practice, the parameter $b(E_i)$ is somewhat noisy, and a smoothing operation or a fit (linear or polynomial) is used to capture the mean value of $b(E_i)$.

Figure 4.6 illustrates the result of this analysis for the NiO IPFY. We see that the fractional error of $b(E_i)$ in the linear fit is on average $\frac{\sigma_{b(E_i)}}{b(E_i)} \sim 0.06/0.47 \times 100\% \approx 13\%$. This is due to the fact that each of the linear fits [Eq. (4.1)] is made with only 6 IPFY data points which are somewhat noisy. Note also that this line fit analysis is omitted in the peak regions since the peak intensities are subject to XMLD intensity variations. The black line shows the result of a 7th order polynomial fit and the dashed blue lines are the $\pm 2\sigma$ confidence bands (95.45% confidence interval) for the fit.[6] From this analysis we find that the fractional change between the extrema of $b(E_i)$ is at most 5.5%, in reasonable

[6]The order of the polynomial fit is selected to obtain the best fit as determined by χ^2 and a visual check of the energy dependence.

agreement with the crude estimate above.[7]

The result of correcting the IPFY_j spectra using this approach is limited to the 3-5% variation of $b(E_i)$ and hardly seems worthwhile when the agreement is sufficiently accurate (within experimental noise) to begin with. However, over a wider energy range, these effects can and do become considerable concerns. To illustrate these effects, we have measured the IPFY of $NdGaO_3$ and extended the measurements considerably above and below the Nd M_5 and M_4 edges.

Note that the above NiO data, the $NdGaO_3$ data described in section 4.2.2 and the relevant IPFY analysis techniques have been compiled into a manuscript which is currently under peer review for publication. A pre-print version of the manuscript is available on the arXiv.[58]

4.2.2 $NdGaO_3$

A single crystal of $NdGaO_3$ was studied by the IPFY, TEY and resonant PFY techniques. The single crystal was obtained from MTI Corporation. They specify that the surface was polished to a surface roughness better than 5 Å with dimensions of 10 mm $\times$ 10 mm $\times$ 0.5 mm and that the crystal was oriented such that the $\langle 100 \rangle$ direction was normal to the sample surface (verified by Laue diffraction). The primary objective of these measurements was to extend the energy range and study the impact of the non-negligible energy dependence in $\mu_Y(E_i)$ and $\nu(E_i)$.

4.2.2.1 X-ray fluorescence and PFY

For these measurements, we used wide energy steps of 1 eV and covered the energy range 800 eV to 1400 eV. In Fig. 4.7, we show the XRF of $NdGaO_3$ at normal incidence in the left panel and the XES spectra in the right panel. The XES spectra are accompanied with a multi-peak fit using a total of 10 gaussians (broadened by $\sim$ 133 eV due to the SDD resolution) at the characteristic x-ray emission energies for Nd, Ga and O between 400 and 1400 eV. The multi-peak fit shows that the sum of these gaussians matches the XES extracted at $E_i = 1350$ eV, where all characteristic x-rays contribute to the emission. The x-ray emission lines that contribute to this fit are summarized Table 4.2.[8]

In the present scenario, it is possible, in principle, to study the x-ray absorption across the Nd M_5 (995.1 eV), Nd M_4 (973.4 eV), Ga L_3 (1116.9 eV) and Ga L_2 (1145 eV) edges

[7] 5.5% is the fractional difference between the maximum in the upper confidence band and the minimum

Table 4.2: Characteristic x-ray emission lines for $NdGaO_3$ between 400 and 1400 eV.[15]

Emission line	Energy (eV)	Transition
O K_{α_1}	524.9	$L_3 \rightarrow K$
Nd M_ζ	753	$N_3 \rightarrow M_5$
Ga L_ℓ	957.2	$M_1 \rightarrow L_3$
Nd M_α	978	$N_{6,7} \rightarrow M_5$
Ga L_η	984.2	$M_1 \rightarrow L_2$
Nd M_β	997	$N_6 \rightarrow M_4$
Ga $L_{\alpha_{1,2}}$	1097.92	$M_{4,5} \rightarrow L_3$
Ga L_{β_1}	1124.8	$M_4 \rightarrow L_2$
Nd K_γ	1180	$N_{4,5} \rightarrow M_3$
Ga $L_{\beta_{3,4}}$	1197	$M_{2,3} \rightarrow L_1$

by use of the non-resonant O K PFY.[9] However, above 1100 eV, the signal to noise ratio of the IPFY arising from the O K emission becomes quite low and statistical noise begins to dominate. As a result, the following analysis focuses on the energy range 880 eV to 1100 eV, where noise levels remain appreciably low. This energy range is still large enough to justify a careful analysis of the energy dependence of the pre-factors in Eq. (3.5).

4.2.2.2 Correction for the energy dependence of $S_{j,k}(E_i)$ in IPFY

Figure 4.8(a) shows the IPFY of $NdGaO_3$ measured at three angles. Note that the XRF was qualitatively similar at all angles and is not reproduced here. As these spectra are collected over a wide energy range, we can now see that there is no longer a simple geometrical factor offsetting the IPFY_j. In order to account for this energy dependence, we take the approach

of the lower confidence band.

[8]In a few cases the emission lines are only separated by a few eV, and it is difficult to distinguish the lines in the resolution-broadened XRF data. In these cases, the relative intensities of the fit parameters are rather inaccurate and a high resolution spectrometer would be a more suitable instrument to identify the emission lines.

[9]It is also possible in principle to utilize the Nd M_ζ emission to study the Ga L edge absorption. This yields a reasonable measure of $\mu_{\text{tot}}(E)$(not shown), but the statistical noise renders the data impractical for use in a careful analysis.

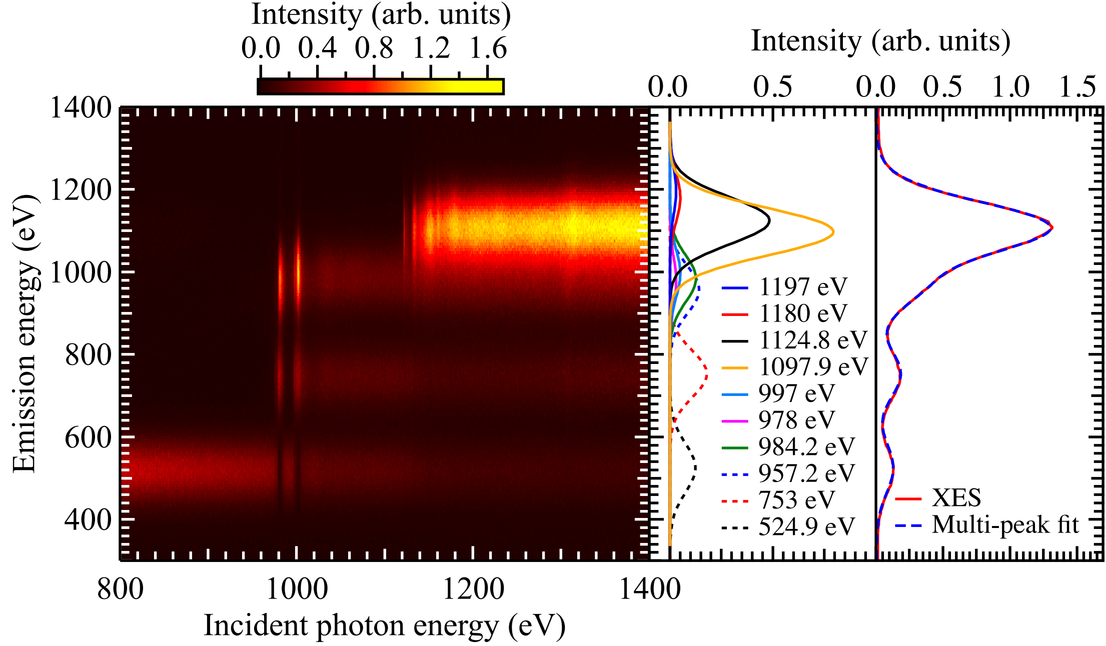

Figure 4.7: Left panel: X-ray fluorescence spectrum of $NdGaO_3$ across the Nd $M_{5,4}$ and Ga $L_{3,2}$ edges. The four easily distinguishable bands of emission arise from a total of 10 x-ray emission processes (Table 4.2). Right panel: A fit to the sum of these x-ray emission lines, broadened by ~ 133 eV.

outlined in section 3.2.2, in particular using Eq. (3.12). The factor $S_{j,k}$, defined as

$$S_{j,k}(E_i) = \frac{\mathrm{IPFY}_j - \mathrm{IPFY}_k}{\frac{\sin\alpha_j}{\sin\beta_j} - \frac{\sin\alpha_k}{\sin\beta_k}}, \tag{4.5}$$

is calculated [Fig. 4.8(b)] from the experimental IPFY data in Fig. 4.8(a). The IPFY_j are then divided by $S_{j,k}$ to eliminate the energy dependence of the pre-factors. Note that this division is done using the linear fit to $S_{j,k}$, which captures the energy dependence reasonably well, to avoid introducing additional noise to the final spectra. The result of this division is shown in Fig. 4.8(c).

We now see that the spectra are rigidly offset. This offset, according to Eq. (3.12), is simply $\frac{\sin\alpha}{\sin\beta}$. Thus, we subtract the appropriate $\frac{\sin\alpha}{\sin\beta}$ for each of the geometries, and find that the spectra collapse onto a single curve (within experimental noise) over a wide energy range [Fig .4.8(d)]. Note here that we have plotted $\mu(E_i)$ rather than $\mu(E_i)/\mu(E_f)$

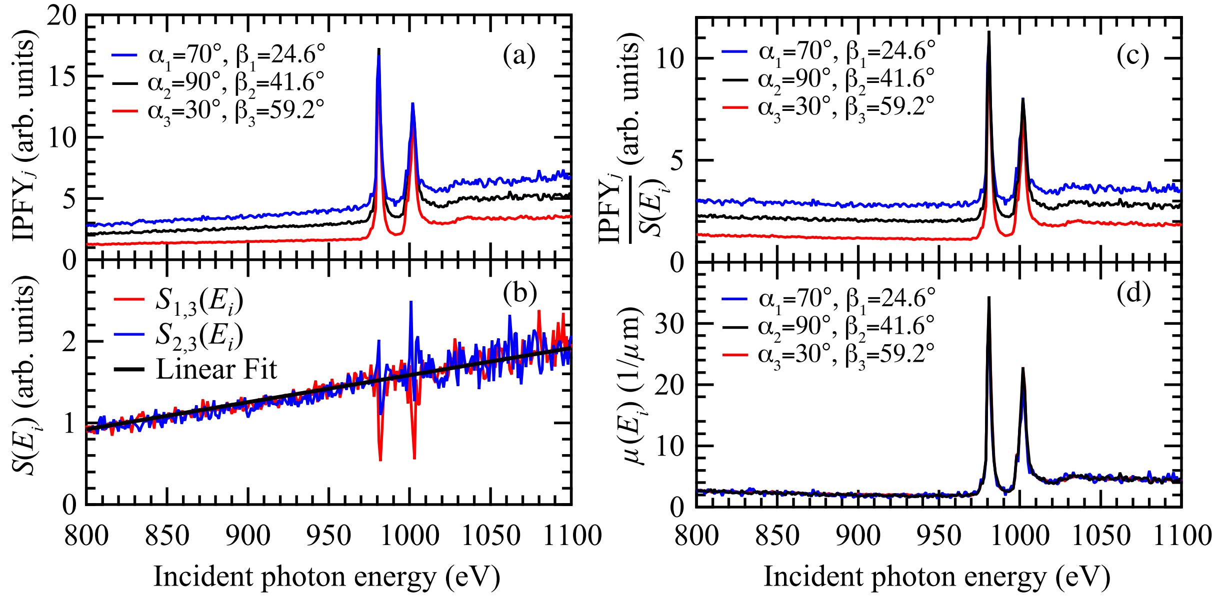

Figure 4.8: (a) The IPFY of $NdGaO_3$ across the Nd $M_{5,4}$ edges over a wide energy range and at the indicated angles. The spectra are not rigidly offset, instead exhibiting a slope. (b) The slope $S_{j,k}$ is evaluated according to Eq. (3.10). We see that the slope does not depend on which set of angles are selected (within experimental noise). A linear fit to $S_{j,k}$ is also shown. (c) The IPFY spectra after division by a linear to fit $S_{j,k}(E_i)$. The spectra are now rigidly offset by $\frac{\sin\alpha}{\sin\beta}$. (d) After subtracting $\frac{\sin\alpha}{\sin\beta}$ and scaling to $\mu(E_f)$ we find that the spectra all collapse onto a single curve.

by scaling to $\mu(E_f = 524.9 \text{ eV}) \approx 3.48659\ \mu\text{m}^{-1}$ for $NdGaO_3$ with a density of $\rho = 7.57$ g/cm^3.[35, 56]

In Fig. 4.9 we now compare this IPFY data, corrected for the energy dependence of the pre-factors, to the calculated value of the x-ray absorption coefficient for $NdGaO_3$ over this wide energy range.[35, 56] We find that the experimental data and the atomic calculations from NIST are in excellent agreement outside of the XANES region.

It should be mentioned that this analysis is somewhat sensitive to the functional form one uses to model the energy dependence of $S_{j,k}(E_i)$. This is understood simply since division by $S_{j,k}(E_i)$ has a strong impact on the shape of the x-ray absorption spectrum. At present, the experimental determination of $S_{j,k}(E_i)$ is rather noisy, which decreases the accuracy of this analysis step. However, this is a limitation of the experimental apparatus

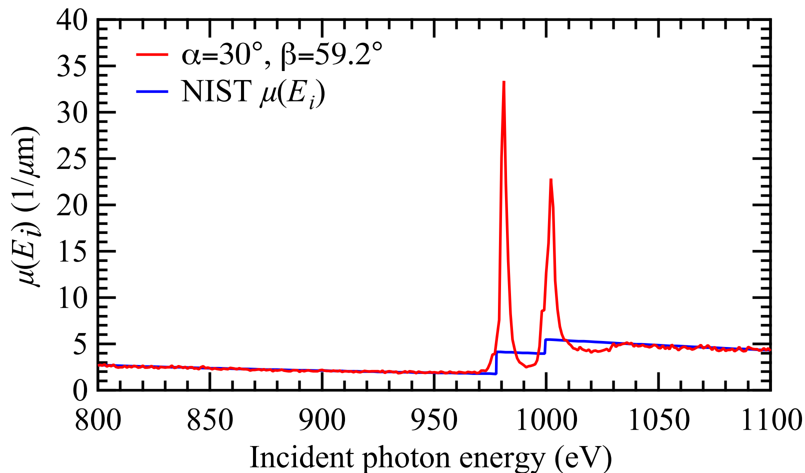

Figure 4.9: A quantitative comparison of the total x-ray absorption coefficient, $\mu_{\text{tot}}(E)$, to calculations of the free atom contributions to $\mu_{\text{tot}}(E)$. We find that IPFY spectra, corrected for the energy dependence of their pre-factors, are in excellent agreement with the calculations outside the XANES region.[35, 56]

at SGM and should not be considered a fundamental limitation to IPFY as a form of spectroscopy. The experimental limitations giving rise to this difficulty and some future plans to overcome them will be discussed in section 4.4.

4.2.2.3 The XANES region of $NdGaO_3$: charging and saturation effects

$NdGaO_3$ is a strongly insulating material and the sample we measured was thick (5×10^6 Å) relative to the x-ray penetration depth ($\sim$ 5000 Å at 950 eV) and the electron escape depth (a few hundred Å – not known precisely). Consequently, the TEY spectra we measured in the XANES region of the Nd $M_{5,4}$ edges were strongly affected by charging effects.[46, 47, 48, 49] This manifested itself in our TEY measurements as an unusual *negative* edge step as shown by the red line in Fig. 4.10. The negative edge steps are highly irregular features and not usually seen in conductive samples. Suspecting that sample charging was occurring, a scan was performed with energy being swept from high photon energy down to low photon energy (blue line). Typically, scans performed in different scanning directions result in overlapping (within experimental noise) spectra, but in this case, there is a substantial difference.

While the precise mechanism leading to the observed discrepancy is not known at this

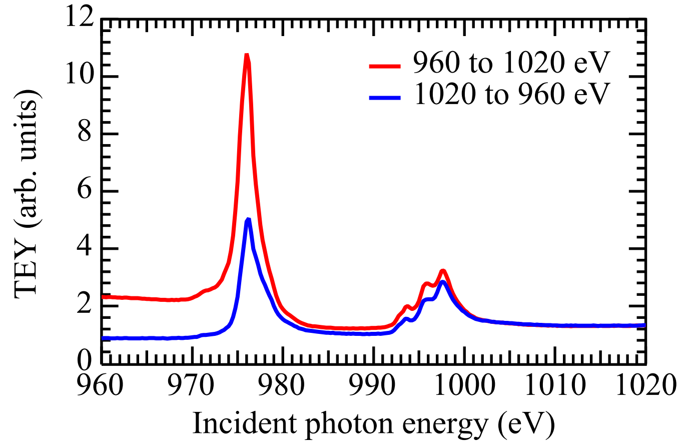

Figure 4.10: TEY spectra of $NdGaO_3$ across the Nd $M_{5,4}$ edges illustrating observed non-equilibrium surface charging effects. The red line corresponds to a scan measured by increasing the photon energy and the blue line by decreasing the photon energy.

time, the origin of charging effects in general can be understood by consideration of the electronic properties of insulators:

1. Insulators undergoing photoemission due to x-ray absorption develop significant positive charge distributions as a function of depth into the sample. The strong electric fields created at the surface and the regions of positive charge have a significant impact on the x-ray photoemission process.[46]

2. λ_e is typically on the order of hundreds of Å in insulators because they experience ineffective electron-electron scattering at low kinetic energy.[45] This means that insulators are more likely than metals and semiconductors to be subject to electron yield saturation effects (recall, the condition for no saturation is $\lambda_x \gg \lambda_e$).

3. The charge distribution varies with $\lambda_x(E)$ since photoemission occurs along the path of the absorbed x-rays.

4. Insulators have resistance and can develop a capacitance due to the x-ray induced photoemission. The positive charge-up is nearly instantaneous as electrons escape from the sample quickly. However, the discharge resulting from a drain current into the sample from ground can be limited by an effective time constant ($\tau \sim RC$). Moreover, since the charge distribution can vary with $\lambda_x(E)$, the effective

time constant can also vary with photon energy. This is especially problematic in the measurement of TEY by the drain current method, as the drain current can lag behind the true TEY.

5. Secondary electrons carry less kinetic energy than primary photoelectrons and Auger electrons, so they are more likely to be trapped in the sample by the positive charge distribution. Consequently, the assumption that the TEY is largely described by the secondary electron yield is not necessarily valid for insulators.

These factors lead to a non-trivial combination of time and energy dependent processes that distort TEY spectra measured on insulators. The negative edge steps observed in our thick, strongly insulating sample of $NdGaO_3$ demonstrate that charging effects (previously considered mainly in the context of XPS) can also have a considerable impact on TEY-based XAS. Unfortunately, it is difficult to confidently determine the underlying mechanism based on the available data. It is likely that many, if not all, of the aforementioned factors would have to be considered for a complete description of the charging effect.

At the moment, the fact remains that these poorly understood charging effects distort electron yield measurements of thick, insulating materials. The only existing alternative measurement techniques are resonant Nd M PFY, TFY and IPFY from the non-resonant O K emission. We will now look at the Nd M PFY and IPFY in $NdGaO_3$.

In Fig. 4.11(a), the resonant Nd M PFY at two sets of angles is shown. As expected for resonant PFY of an element in high concentration, we observe strong saturation effects that distort the spectra. In contrast, the IPFY, shown in Fig. 4.11(b), is in excellent agreement with a TEY measurement of pure Nd.[59] This is a reasonable comparison to make, as the Nd atoms in the distorted perovskite lattice of $NdGaO_3$ are Nd^{3+} in character and the pure Nd XANES structure is well described by an atomic multiplet calculation of Nd^{3+}.[60, 59]

In $NdGaO_3$ and other insulators, the combination of EY charging effects and PFY saturation effects make XAS studies difficult to interpret. Calculated models based on data that appears saturated or exhibits unusually large absorption peaks with negative (or flat) edge steps are likely to suffer from considerable systematic errors. This applies to the determination of atomic scattering form factors, modelling of electronic structure in the XANES region and for analysis of EXAFS data. IPFY spectroscopy, as shown above, allows for an accurate measure of $\mu(E)$ in precisely these cases and should allow for this experimental impasse to be overcome.

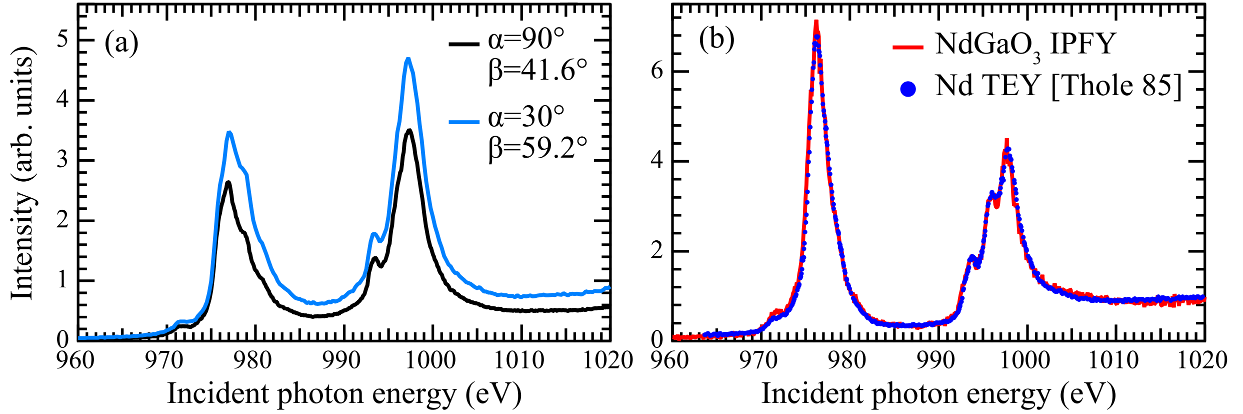

Figure 4.11: (a) PFY and (b) IPFY of $NdGaO_3$ at the Nd $M_{5,4}$ edge. The PFY exhibits strong saturation effects, while the IPFY agrees very well with TEY data from Ref. [59] on pure Nd, which has Nd $^{3+}$ like Nd in $NdGaO_3$. The spectra in (b) were scaled and offset to match in the pre- and post-edge regions.

4.3 Determining sample stoichiometry

The methods described theoretically in section 3.2.2 and demonstrated experimentally in section 4.2.2.2 illustrate that IPFY spectra can be used to determine $\mu(E_i)/\mu(E_f)$. If the sample stoichiometry is known, the scaling to $\mu(E_f)$ can be a straightforward way to check the sample's composition. However, there are cases when stoichiometry is not known and this scaling cannot be done directly. Nevertheless, $\mu(E_i)/\mu(E_f)$ is intimately related to material composition and can be used to work backwards from experimental data to determine $\mu_{\text{tot}}(E)$. Here we will illustrate how to accomplish this in principle and practically using the above $NdGaO_3$ IPFY data.

4.3.1 Principles

The total absorption coefficient of a material is given by

$$\mu_{\text{tot}}(E_i) = \sum_X \rho_X \mu_X^m(E), \tag{4.6}$$

where the ρ_X is the atomic density of element X in the material and $\mu_X^m(E)$ is the mass absorption coefficient of element X. The units of $\mu_X^m(E)$ are typically cm^2/g. If one has a

measure of $\frac{\mu(E_i)}{\mu(E_f)}$ instead of simply $\mu(E_i)$, then one can write

$$\frac{\mu_{\rm tot}(E_i)}{\mu_{\rm tot}(E_f)} = \frac{\sum\limits_X \rho_X \mu_X^m(E_i)}{\sum\limits_X \rho_X \mu_X^m(E_f)} = \frac{\sum\limits_X \frac{N_X m_X}{V} \mu_X^m(E_i)}{\sum\limits_X \frac{N_X m_X}{V} \mu_X^m(E_f)} = \frac{\sum\limits_X N_X m_X \mu_X^m(E_i)}{\sum\limits_X N_X m_X \mu_X^m(E_f)}, \tag{4.7}$$

where N_X is the number of atoms X per unit cell, m_X is the atomic mass of atom X and V is the volume of the unit cell. The unit cell volume is a common term and cancels out.

The only unknowns in Eq. (4.7) are the N_X, since the atomic masses are known and the mass absorption coefficients far from the XANES can be assumed to follow the atomic absorption due to excitations into the continuum. If there are n elemental species, then this problem can be reduced to an $n-1$ nonlinear fitting problem. This is accomplished by division of N_{X_1} in the numerator and denominator, and by defining the fractional number densities $R_j = N_{X_j}/N_{X_1}$. Since $R_1 = 1$, the model reduces to Eq. (4.8) with $n-1$ fit coefficients $(R_2, R_3, \cdots, R_n)$.

$$\begin{aligned}\frac{\mu_{\rm tot}(E_i)}{\mu_{\rm tot}(E_f)} &= \frac{\sum\limits_{j=1}^{n} R_j m_{X_j} \mu_{X_j}^m(E_i)}{\sum\limits_{j=1}^{n} R_j m_{X_j} \mu_{X_j}^m(E_f)} \\ &= \frac{m_{X_1}\mu_{X_1}^m(E_i) + R_2 m_{X_2}\mu_{X_2}^m(E_i) + \cdots + R_n m_{X_n}\mu_{X_n}^m(E_i)}{m_{X_1}\mu_{X_1}^m(E_f) + R_2 m_{X_2}\mu_{X_2}^m(E_f) + \cdots + R_n m_{X_n}\mu_{X_n}^m(E_f)}\end{aligned} \tag{4.8}$$

4.3.2 Demonstration with $NdGaO_3$ IPFY data

In the case of $NdGaO_3$, Eq. (4.8) becomes

$$\frac{\mu_{\rm tot}(E_i)}{\mu_{\rm tot}(E_f)} = \frac{m_{\rm Nd}\mu_{\rm Nd}^m(E_i) + R_2 m_{\rm Ga}\mu_{\rm Ga}^m(E_i) + R_3 m_{\rm O}\mu_{\rm O}^m(E_i)}{m_{\rm Nd}\mu_{\rm Nd}^m(E_f) + R_2 m_{\rm Ga}\mu_{\rm Ga}^m(E_f) + R_3 m_{\rm O}\mu_{\rm O}^m(E_f)}, \tag{4.9}$$

with nominal values of $R_2 = 1$ and $R_3 = 3$ for stoichiometric $NdGaO_3$. We obtain the mass absorption coefficients of Nd, Ga and O from calculations in Ref. [35] which are conveniently available online (Ref. [56]). These are shown in the soft x-ray region in Fig. 4.12(a).

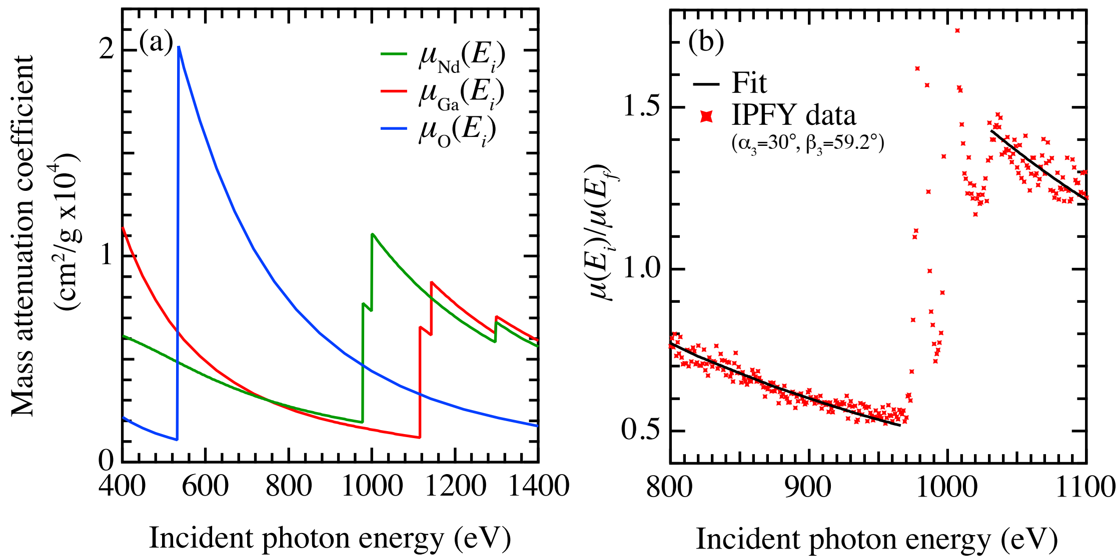

Figure 4.12: (a) The mass absorption coefficients for Nd, Ga and O.[35, 56] (b) The result of a fit based on Eq. (4.9) and the mass absorption coefficients in (a). The fit captures both the edge step and the energy dependence of the IPFY data (excluding the XANES).

A least-squares fit of the form presented in Eq. (4.9) was performed using these coefficients as inputs to $\mu(E_i)/\mu(E_f)$ as determined by the analysis procedure described in section 4.2.2.2. The XANES region of the experimental data was excluded from the fit. The result of this fit is shown in Fig. 4.12(b). The relative concentrations determined by the fit are given by $R_2 = 1.07 \pm 0.01$ and $R_3 = 3.03 \pm 0.04$. The uncertainties here are representative of $\pm\sigma$ (one standard deviation) and come from the statistical uncertainty in the IPFY data alone. Based purely on fitting statistics, our results are outside of the $\pm 1\sigma$ range for R_2 and within it for R_3.

To verify that the accuracy of the fit was not limited by artificial fitting errors, a simulated absorption spectrum was made by adding up the atomic mass absorption coefficients with randomly selected coefficients (not shown). In this scenario the least-squares fit converged very precisely to the randomly selected coefficients with relative errors on the order of 10^{-14}. It should also be mentioned that this fitting approach used linear interpolations of the tabulated data in Ref. [35] to evaluate the absorption coefficient at energies that were not tabulated. The data in Ref. [35] is tabulated such that the variation between any two points can be treated as approximately linear, so this should not be a major source

of error. As such, it is reasonable to conclude that the fitting code itself is not a major source of uncertainty in the determination of R_2 and R_3 and that other factors are more important.

One such factor is the division by $S_{j,k}(E_i)$. Even small differences in how one fits $S_{j,k}(E_i)$ can result in changes to the energy dependence of the derived $\mu(E_i)/\mu(E_f)$ that are not well captured by the statistical errors of the fit parameters. This sensitivity is difficult to quantify and can be considered as a systematic analysis error. Using different fits (linear, polynomial, etc.) to $S_{j,k}(E_i)$ results in variations of R_2 and R_3 on the order of 15%, which is larger than the uncertainty due to statistics alone.

Another source of error is in the tabulated mass absorption coefficients. Between 500 and 1000 eV, these tables are estimated to have uncertainties ranging between 3% far from absorption edges up to 20% near absorption edges.[36, 35] Since we have excluded the near edge regions from the fit, a more realistic estimate for the uncertainty is 3% to 10%. These errors *should* factor into the overall determination of confidence levels for the fit. However, this is difficult to do in practice as the errors are not sufficiently detailed and there is no clear avenue for adding uncertainty to the functional forms of the μ_X^m without over-parametrizing the model and losing considerable accuracy in the process.[10]

Hence, it is reasonable to conclude that the discrepancy observed between the fitted R_2 and R_3 and their nominal values is largely due to both the sensitivity of fitting $S_{j,k}(E_i)$ and the uncertainty in the tables of mass absorption coefficients. Based on the errors in both of these parameters, a moderate estimate of the uncertainties for R_2 and R_3 is $\sim 15\%$, giving $R_2 = 1.1 \pm 0.2$ and $R_3 = 3.0 \pm 0.5$, indicating that the material is most likely $NdGaO_3$.

A large part of this uncertainty stems from the experimental noise of the $NdGaO_3$ data and should not be considered a *fundamental* limitation of the technique. Reducing the noise level would significantly enhance the determination of $S_{j,k}(E_i)$ and would reduce all statistical fitting uncertainties. Motivated by this problem, we will discuss the current experimental limitations leading to these high noise levels and our plans to address these. Once noise levels are improved, the uncertainty of the tabulated data should become the limiting factor in the accuracy of this method. If efforts are made to avoid high uncertainty regions of the tabulated mass absorption data, the ultimate accuracy of the technique should be able to reach the $\sim 3\%$ error level, which should be adequate for the determination of sample stoichiometry in a wide range of materials.

[10] Instead of $n-1$ coefficients, there are $2n-1$ coefficients if each of the μ_X^m are allowed to vary by a small amount. Furthermore, the coefficients are in competition with one another and constraints must be used. Consequently, the fit will tend to reach multiple constraint boundaries and be a poor representation of the true absorption.

4.4 Current experimental limitations

In the previous sections, we have discussed how experimental noise is the limiting factor in the accuracy of determining $\mu(E_i)/\mu(E_f)$ and the sample stoichiometry. This is not a fundamental limitation of IPFY spectroscopy and is instead related to limitations with the currently installed detection scheme. Ultimately, the limitation is that the detected count rate loses its proportionality to the input count rate above 20000 counts/sec (cps) with the available Princeton Gamma-Tech Sahara SDD. Moreover, the available deadtime correction scheme is inaccurate and cannot be relied on. Hence, when making these measurements, we were forced to operate with a maximal count rate of 20000 cps, even though considerably more photon flux was available. To understand where this limitation comes from and how we can overcome it, we will briefly review how SDDs operate.

Silicon drift detectors are semiconductor devices designed to measure electrons produced within a small volume by the absorption of x-rays. In modern SDDs, this volume is typically made of high-resistivity n-type silicon and is depleted by concentric rings of reverse biased p^+ junction arranged around a small area n^+ anode.[61] The electric field created by this topological arrangement of p^+ junctions drives electrons created by absorption of photons within the depleted volume towards the n^+ anode. This anode is typically connected to a field-effect transistor used to amplify the signal. With pulse-discriminating digital signal processing, the produced pulses are assigned an energy and placed in the appropriate energy bin of a multi-channel analyzer. One key parameter in this signal processing is the shaping time associated with the pulse shaping. Longer shaping times provide better energy resolution while shorter shaping times reduce energy resolution. The trade-off is the maximum count rate. Shorter shaping times trade energy resolution for higher count rates.

The shortest available shaping time on the available SDD is 0.5 μs, providing an energy resolution of $\sim$ 130 eV. Unfortunately, with this shaping time, the detection throughput does not track the input rate linearly above about 20000 cps. This is because the probability that an electron will reach the anode before the 0.5 μs shaping time has elapsed increases with input photon flux. This is typically referred to as pile-up and leads to electronic dead time. A few different schemes exist to account for dead time and correct for it, but we found it preferable to operate in the linear counting regime to avoid unnecessary (and potentially suspect) modification of the raw XRF data to account for dead time.

Consequently, the XRF data was collected such that the maximal count rate stayed below $\sim$ 20000 cps for all incident photon energies E_i. Because IPFY is a measure of the fluorescence contribution of a non-resonant emission line, when the absorption increases

strongly due to a resonant absorption process, the number of non-resonant counts decreases. Since most of the counts are then contained within the resonant emission line, the statistical noise of the IPFY becomes worse. This is visible in the data — above the absorption edges (where the resonant emission dominates) the statistical noise is larger in the IPFY.

We can also understand this from photon counting statistics which follow the Poisson distribution. The signal to noise ratio (SNR) in photon counting is given by SNR $= N/\sqrt{N} = \sqrt{N}$, where N is the mean number of counts. We find that the IPFY, given simply by IPFY $= 1/(N \pm \sqrt{N})$, has the same SNR

$$\frac{\text{IPFY}}{\sigma_{\text{IPFY}}} = \frac{1/N}{\sqrt{\left(\frac{\partial}{\partial N}\left(\frac{1}{N}\right)\sqrt{N}\right)^2}} = \sqrt{N}. \tag{4.10}$$

To model the effect of shifting counts from a non-resonant FY channel to a resonant FY channel, we define a as the fraction of counts in the resonant channel. The fraction of the total counts in the non-resonant channel is then $1 - a$. Including this fraction for the SNR ratios, we find $\text{SNR}_{\text{res}} = \sqrt{aN}$ and $\text{SNR}_{\text{IPFY}} = \sqrt{(1-a)N}$. Below $a = 0.5$, the IPFY has a higher SNR and above it the resonant PFY has a higher SNR. Hence, the decrease in SNR observed in IPFY spectra above the absorption edge can be understood as a statistical phenomenon arising from shifting intensity from one channel to another.

Based on the data shown in Fig. 4.12, we can estimate that the standard error would have to be reduced by a factor of 3 to 4 in order to bring the statistical noise to within 1-2% of the fit line. This represents increasing the count rate to somewhere between 90000 to 160000 cps, factors of 4.5 to 8 higher than the 20000 cps limit imposed by the SDD's non-linearity. This could simply be done at a count rate of 20000 cps with longer integration times, but the experiment would be prohibitively long to perform.

Ideally, a detector capable of handling a high count rate with fast pulse shaping electronics and an accurate dead time correction scheme would be used. With such a detector, we could reduce the sample-detector distance (ie. larger solid angle) and increase the flux coming from the beamline at the expense of energy resolution (by increasing the exit slit from 15 μm to 50 μm).

Two Amptek SDDs have already been ordered for this purpose. These detectors can handle pulse shaping times down to 0.1 μs, have very fast electronics and a powerful deadtime correction scheme that can allow one to maintain linearity and high energy resolution even with high input count rates and longer shaping times. Moreover, these detectors are more suitable for fine tuning at a beamline than the current SDD which does not provide much control over the operation of the pulse shaping electronics.

Additionally, a new endstation is currently being designed by Tom Regier, the SGM beamline scientist, that will be optimized for IPFY spectroscopy. The design features two SDD detectors in the chamber at different angles. As such, it will be possible to determine $S_{j,k}(E_i)$ from data contained within a single scan, which reduces the number of scans needed for the analysis and reduces the number of factors that could increase experimental uncertainty (eg. motorization problems or beamline instabilities). The design will also feature more rotational degrees of freedom than the current endstation and a precisely defined geometry, such that the errors in α and β should be reduced considerably. It is also designed to be modular so that additional detectors could easily be installed in the future. An array of SDD detectors would further drive down the experimental uncertainties and could potentially make IPFY spectroscopy a powerful and reliable method to non-destructively determine sample stoichiometry and $\mu_{\text{tot}}(E)$ with relative simplicity.

4.5 IPFY of $La_{1.475}Nd_{0.4}Sr_{0.125}CuO_4$

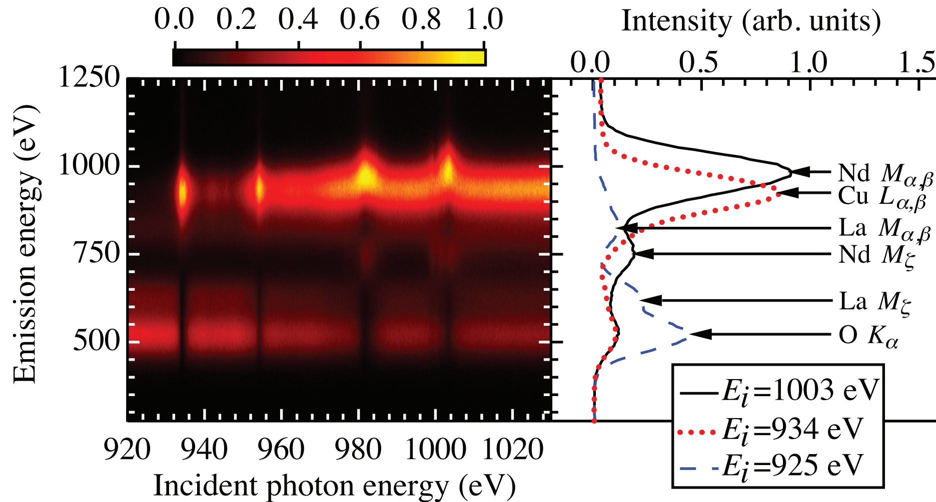

Figure 4.13: X-ray fluorescence spectrum of $La_{1.475}Nd_{0.4}Sr_{0.125}CuO_4$ across the Cu $L_{3,2}$ and Nd $M_{5,4}$ absorption edges. Emission lines from Nd, Cu, La, and O are observed, as indicated in the right panel.

To further demonstrate the general applicability of IPFY to materials of interest in a wide range of fields, we present IPFY measurements on the superconducting cuprate

$La_{1.475}Nd_{0.4}Sr_{0.125}CuO_4$(LNSCO). This material is of general interest to condensed matter physicists as the doping of Nd atoms for La atoms in $La_{2-x}Sr_xCuO_4$ stabilizes a low temperature tetragonal phase which gives rise to static charge and spin density wave order.[62, 63, 64, 65, 66] Coincidentally, our first comprehensive series of IPFY measurements were performed on LNSCO and our first paper describing IPFY was based on these measurements.[38] However, our subsequent measurements on NiO and $NdGaO_3$ demonstrate the angle dependence of IPFY and the implications of this relationship more clearly, so we have opted to present those first in this thesis.[11]

One advantage of measuring IPFY on LNSCO is that it cleaves nicely along the *ab* plane so that TEY measurements could be reliably used as a basis for comparison with IPFY. The sample was oriented with the *c* axis in the beam direction and cleaved along the *ab* plane at a pressure of $5 \cdot 10^{-8}$ Torr. The polarization was linear horizontal and perpendicular to the *c* axis.

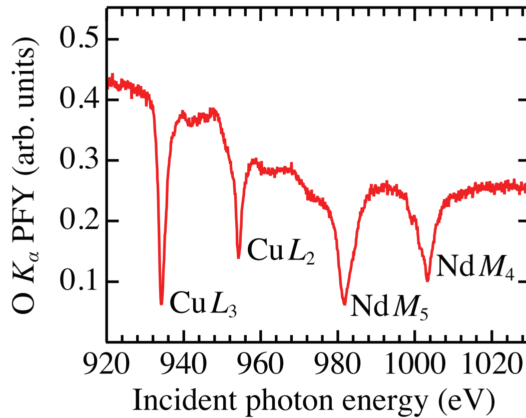

Figure 4.14: O K PFY of $La_{1.475}Nd_{0.4}Sr_{0.125}CuO_4$ across the Cu $L_{3,2}$ and Nd $M_{5,4}$ absorption edges. Dips corresponding to the peaks in the Cu and Nd absorption edges are observed.

XAS measurements across the Cu $L_{3,2}$ and Nd $M_{5,4}$ edges of LNSCO were made. Figure 4.13 shows the XRF spectrum in the left panel and the emissions lines in the right panel. The O K emission is in close proximity to the La M_ζ emission, but it is nonetheless possible to extract the O K emission independently of the La M_ζ emission.[12] Moreover, it is apparent from Fig 4.13 that the non-resonant La M_ζ emission bears the signature "dips"

[11] A manuscript based on the NiO and $NdGaO_3$ measurements is currently under review.[58]

[12] Two approaches to verifying this were taken: 1) Using narrow extraction windows at lower energies.

of non-resonant PFY spectra and could also be used for IPFY. However, the O K emission is stronger and provides a better SNR.

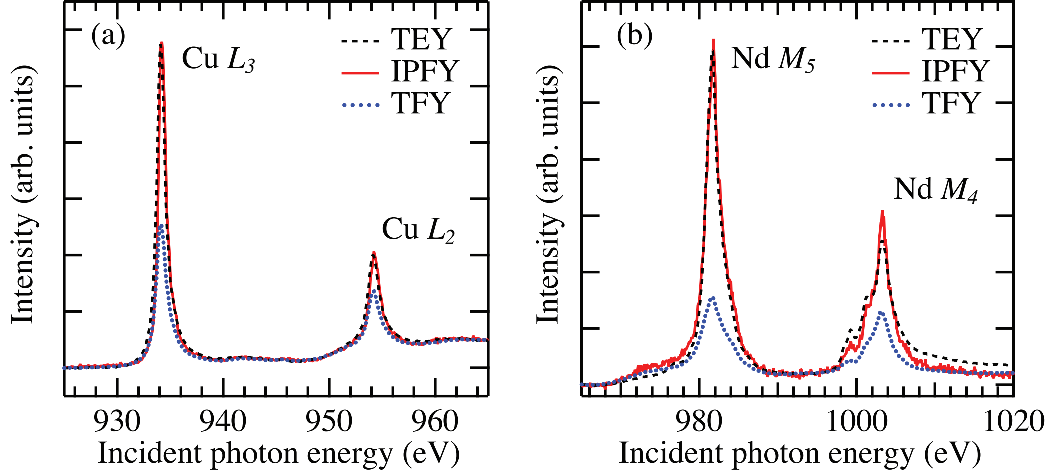

Figure 4.15: IPFY of $La_{1.475}Nd_{0.4}Sr_{0.125}CuO_4$ across the (a) Cu $L_{3,2}$ and (b) Nd $M_{5,4}$ absorption edges, as compared to TEY and TFY measurements. The IPFY is in excellent agreement with the TEY whereas the TFY is strongly distorted by saturation effects.

Figure 4.14 shows the non-resonant O K PFY extracted from the XRF spectrum in Fig. 4.13. The dips occur at photon energies that corresponding to the absorption peaks related to the Cu $L_{3,2}$ and Nd $M_{5,4}$ edges of LNSCO. The IPFY is determined by inverting this spectrum. Figure 4.15 compares the TEY and TFY measured simultaneously to the IPFY. We see that the TEY and IPFY are in excellent agreement, whereas the TFY is strongly distorted by saturation effects. Moreover, the energy dependence of the Cu $L_{3,2}$ and Nd $M_{5,4}$ absorption edges measured by IPFY agrees with our expectation for LNSCO.

For instance, the XAS at the Cu $L_{3,2}$ edges is in good agreement with prior work by Chen *et al.* on $La_{1.85}Sr_{0.15}CuO_4$ (LSCO) for a measurement $\boldsymbol{\epsilon} \perp c$.[67] Chen *et al.* showed that the strong Cu $L_{3,2}$ absorption in this geometry corresponds to transitions between the $2p_{3/2}$ and $2p_{1/2}$ core electrons to Cu $3d_{x^2-y^2}$ holes. With $\boldsymbol{\epsilon} \parallel c$, where the Cu $L_{3,2}$ absorption edge corresponds to transitions into $3d_{3z^2-r^2}$ holes, Chen *et al.* observed much weaker absorption. Their work demonstrated that holes in the CuO_2 plane of LSCO have

2) Using gaussian fits to the La M_ζ emission to subtract this emission line from the XRF spectrum and then extract the O K emission. In both cases, the extracted PFY and IPFY were in close agreement.

predominantly $3d_{x^2-y^2}$ character and placed strong constraints on theories requiring out-of-plane orbital character for the Cu atoms in the CuO_2 plane.

Furthermore, the x-ray absorption features seen at the Nd $M_{5,4}$ edges, corresponding to $3d^{10}4f^3 \rightarrow 3d^9 4f^4$ transitions, seem to be reasonably well described by atomic multiplet calculations of Nd^{3+} and XAS on pure Nd.[59] The reason one might expect some agreement between the Nd $M_{5,4}$ edges in LNSCO and atomic multiplet calculations for Nd^{3+} is that rare-earth elements such as Nd have strongly localized $4f$ electrons, meaning that interactions of the $4f$ orbitals with orbitals of nearest neighbour atoms are often not important.[13]

Our measurements on $La_{1.475}Nd_{0.4}Sr_{0.125}CuO_4$ illustrate the appropriateness of IPFY spectroscopy as a bulk sensitive measure of XAS in complex materials as well as the simpler NiO and $NdGaO_3$ systems. It should be noted that this comparison between TEY, TFY and IPFY relies on the fact that the range of photon energies is narrow (across the Cu $L_{3,2}$ and Nd $M_{5,4}$ edges, respectively). In other words, this is a demonstration of the utility of the approximate form of the IPFY expression [Eq. (3.6)], which we showed to be a reasonable approximation over a narrow energy range in section 4.2.1.4.

4.6 IPFY of stainless steel for $E > 6.5$ keV

In the previous sections we have presented experimental evidence to support the validity of IPFY at soft x-ray energies with measurements on single crystals of NiO, $NdGaO_3$ and $La_{1.475}Nd_{0.4}Sr_{0.125}CuO_4$ at the SGM beamline. In the interest of verifying the general validity of IPFY, we also performed measurements using higher energy x-rays at the CLS's SXRMB beamline. Here we will present IPFY measurements of a stainless steel sample that reinforce the notion that the key to IPFY spectroscopy is the use of a non-resonant emission line.

4.6.1 Measurement details

The Soft X-ray Microcharacterization Beamline (SXRMB) is a medium energy beamline with an energy range of 1.7 keV to 10 keV. The source of light at this beamline is from bending magnet radiation which, unlike the undulator at SGM, produces a broad energy spectrum. The energy is monochromated by x-ray diffraction using either an InSb(111)

[13] The same argument can be made about the Nd $M_{5,4}$ edges of $NdGaO_3$.

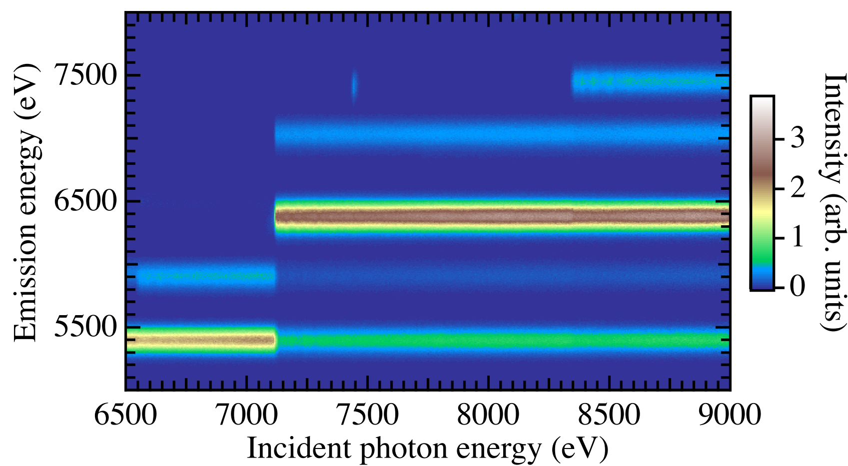

Figure 4.16: X-ray fluorescence spectrum of SS304 across the Fe K and Ni K absorption edges. Emission lines from Cr, Mn, Fe and Ni are observed (see Table 4.3 for details).

crystal or a Si(111) crystal. The beamline was still under commissioning when we performed the experiments, so some issues with the beam spot size existed. The beam spot was much wider than the design specification for the beamline, due to some difficulties with the optics. We used motorized slits to narrow the beam in the horizontal direction to avoid an ill-defined geometry.

The XAFS endstation was equipped with a motorized rotation stage. Like at SGM, the TEY, TFY and PFY were measured using the drain current, a MCP and a SDD, respectively. The SDD detector at SXRMB was the same model as equipped at SGM and subject to the same maximal input count rate of ∼20000 cps.

4.6.2 Results and discussion

We measured a sample of stainless steel 304 (SS304). The primary elements in SS304 are Fe, Ni, Cr, Mn and C. The Fe K and Ni K absorption edges are at 7.112 keV and 8.332 keV, respectively. Cr has a strong K_α emission line at 5414.7 eV. Hence, the premise of this experiment was to see if IPFY from the non-resonant Cr K_α emission could produce a reliable measure of the Fe K and Ni K absorption edges. Figure 4.16 shows the XRF spectrum for SS304 across the Fe K and Ni K absorption edges. The observed emission lines are summarized in Table 4.3.

Table 4.3: Observed characteristic x-ray emission lines for SS304.[15]

Emission line	Energy (eV)	Transition
Cr K_{α_1}	5414.72	$L_3 \to K$
Mn K_{α_2}	5887.65	$L_2 \to K$
Mn K_{α_1}	5898.75	$L_3 \to K$
Cr K_{β_5}	5986.9	$M_{4,5} \to K$
Fe K_{α_2}	6390.84	$L_2 \to K$
Fe K_{α_1}	6403.84	$L_3 \to K$
Fe $K_{\beta_{1,3}}$	7057.98	$M_{2,3} \to K$
Ni K_{α_2}	7460.89	$L_2 \to K$
Ni K_{α_1}	7478.15	$L_3 \to K$

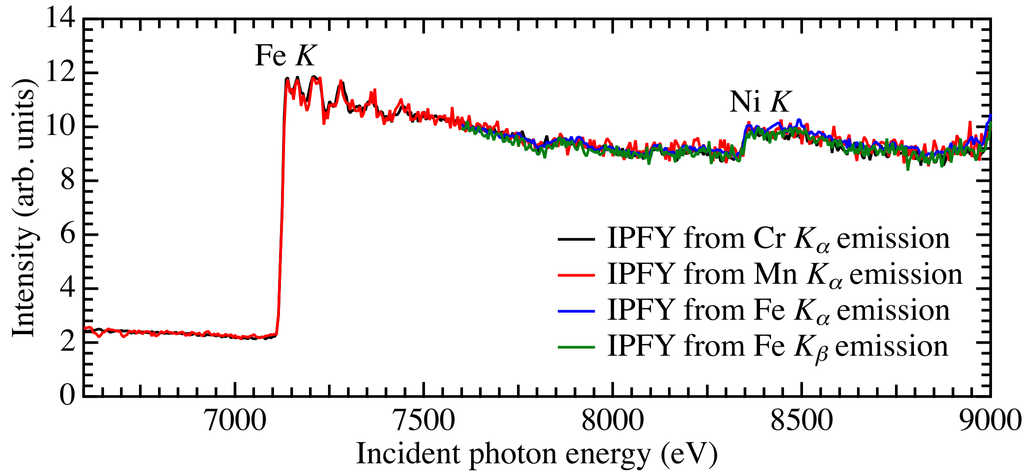

Figure 4.17: IPFY spectra derived from the XRF data in Fig. 4.16. The IPFY from the Cr K_α and Mn K_α both capture the Fe K edge and its associated EXAFS features, as well as the Ni K edge. The IPFY derived from the Fe K_α and Fe K_β can also be used to measure the Ni K edge and these spectra agree well with the IPFY derived from the Cr K_α and Mn K_α emissions.

The dip observed in the Cr K_α line at the onset of the Fe K absorption edge suggests that the inverse relationship between non-resonant emission and the total x-ray absorption coefficient still exists at high energy and is not a phenomenon limited to low energy excitation processes. We also observe a similar dip in the Mn K_α emission at the onset of the Fe K edge. This is not unexpected, as this emission line also represents a non-resonant process and should, according to the principles laid out in chapter 3, also be inversely related to $\mu_{\text{tot}}(E)$. Hence, we have two different non-resonant emission lines that can be used to study the IPFY for the Fe K edge. At the Ni K edge, it is possible to measure the IPFY using the four non-resonant emission lines: Cr K_α, Mn K_α and Fe $K_{\alpha,\beta}$.

There is one curious feature that the reader may have observed in Fig. 4.16 — a spot at $E_i = E_f = 7435$ eV. In fact, if one looks at this XRF data over a wider energy range, a number of such spots appear on a line with $E_i = E_f$.[14] The origin of these spots is hinted at by nature of this line – $E_i = E_f$ is the condition for elastic scattering. This is strong evidence that these spots are x-ray diffraction peaks satisfying the Bragg condition that unintentionally impinged the surface of the SDD. The likelihood of unintentionally observing Bragg peaks on a detector is increased dramatically with a polycrystalline substance such as SS304 – a large number of randomly oriented crystallites exist in polycrystalline materials. Hence, this should not be treated as a glitch or anomaly of the measurement, but a real phenomenon whose origin is reasonably well understood. Note that because IPFY relies on a measurement where E_f is well separated from E_i, scattering peaks should never interfere with the measurement of IPFY. In contrast, such scattering can unintentionally contribute to TFY or resonant PFY measurements.

Figure 4.17 shows the IPFY extracted from the XRF data in Fig. 4.16 for the Cr K_α, Mn K_α and Fe $K_{\alpha,\beta}$ emission lines. These were extracted in 150 eV windows centered at the emission line energies. The IPFY spectra were scaled and offset so they could be directly compared. For the Fe K IPFY, the data is only shown starting at 7600 eV, which is just above the Fe K EXAFS and about 700 eV above the Fe K edge.[15] Comparing the IPFY from the Cr K_α and Mn K_α emission lines (black and red) we see that they agree very well below the Fe K edge, in the Fe K EXAFS region and up to the Ni K edge and beyond (within experimental noise).[16] Moreover, the IPFY determined from the Fe $K_{\alpha,\beta}$ emission lines are in good agreement across the Ni K edge. It should be noted that the

[14]A total of 6 Bragg peaks can be clearly distinguished.

[15]Note that below the Fe K edge, the IPFY is not well defined as the transition probability is zero and the IPFY goes to infinity.

[16]It should be mentioned that the Mn K_α emission and Cr K_{β_5} lines are very nearby. Consequently, the PFY from Mn K_α emission included a contribution from the Cr K_{β_5} line. This could not be avoided as the lines become nearly indistinguishable above the Fe K edge.

noise levels in the IPFY here are related to the same difficulty experienced at SGM — the flux had to be reduced to keep the count rate on the SDD below $\sim$ 20000 cps. As discussed in section 4.4, this is an instrumental limitation rather than a fundamental limitation of the technique.

These results demonstrate that IPFY is a viable measure of XAS not only at soft x-ray energies, but also at intermediate x-ray energies (5 to 10 keV). Furthermore, the finding that multiple non-resonant emission lines provide IPFY spectra in agreement with one another confirms that IPFY is not limited to cases where an O K_α emission line is available. Such a notion may have been unintentionally implied by its repeated use for the soft x-ray measurements of NiO, $NdGaO_3$ and LNSCO.[17] Although experiments have not yet been performed to prove it, the same principles should hold in the hard x-ray regime (above 10 keV). Many hard x-ray beamlines are already equipped with energy discriminating detectors, so the barrier to attempting such experiments is low. It is expected that proof-of-concept experiments will be conducted in the near future, if not at the CLS then at one of the many synchrotrons worldwide.

[17] O K_α emission was used so often because it conveniently provides a low energy emission line that is still accessible on the SDD ($E_f > 200$ eV) and because it is a common element in many materials.

Chapter 5

Special Cases

The IPFY expressions derived in chapter 3 assumed that the measurement was made on a thick, homogeneous sample. There are, however, many instances in which XAS is studied on thin film, multilayer or powder specimens. In such cases, it would be useful to quantify the appropriateness of IPFY. In this chapter, these effects will be discussed. Where it is possible, simple models describing the phenomena are presented. Where no simple solutions exist, a general outline of how to approach the problem will be presented.

5.1 Multilayers

The general theory of x-ray fluorescence from multilayer samples with various elements in each layer can quickly become overwhelmingly complex.[37] This problem is exacerbated if one begins to consider secondary and tertiary fluorescence contributions. These contributions occur when the decay of an excited atom emits a photon which is then re-absorbed. The second absorption process has a finite probability of emitting a photon and this photon may escape from the sample and contribute to the XRF spectrum or be re-absorbed. The expressions governing such contributions from multilayer samples are very cumbersome.

Fortunately, in many cases the fluorescence probability is quite low. For instance, the fluorescence probability for L and M shells of atoms with atomic number $Z < 60$ is less than 10%.[29] Hence, the joint probability of secondary fluorescence is typically less than 1% for the L and M shells. For high-Z K shells, the fluorescence probability is considerably higher and secondary contributions may be significant. However, K shell fluorescence for high Z elements occurs primarily in the hard x-ray regime, so this consideration is less significant

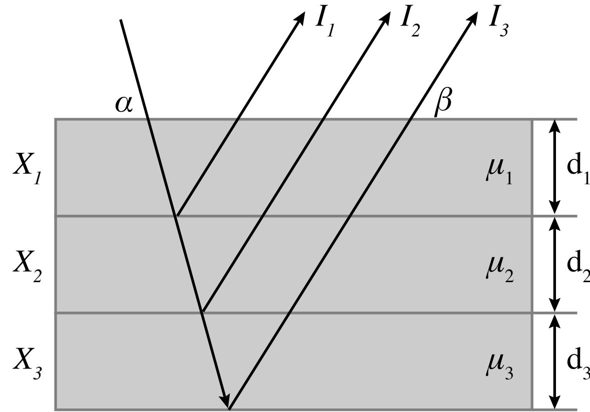

Figure 5.1: The multilayer geometry considered for the derivation of the fluorescence intensity.

with soft x-ray emission lines, such as the O K_α line. Consequently, for the purposes of soft x-ray XAS, we are justified in neglecting secondary and tertiary contributions.

A further simplification we will make is to only consider a case of 3 layers, as this will cover all the special cases we are presently interested in. The theory outlined here should generalize to more layers, as needed. Figure 5.1 illustrates the geometry for the 3 layer case. The different layers contain the sets of atoms X_1, X_2 and X_3, the thicknesses of the layers are d_1, d_2 and d_3, and the total x-ray absorption coefficients of the layer are given by μ_1, μ_2 and μ_3, respectively. The angles of incidence and detection are α and β.

We can consider the intensity arising from the absorption of x-rays in each of the layers separately and label these contributions I_1, I_2 and I_3, as indicated. For notational convenience we have dropped division by I_0 and the explicit dependence of the intensity on E_i and E_f. Let us first consider intensity arising from the first layer. This follows directly from the development of the TFY expression in section 2.2. We find that

$$I_1 = \eta(E_f)\frac{\Omega}{4\pi}\sum_{X_1}\frac{\omega_{X_1}(E_i,E_f)\mu_{X_1}(E_i)}{\mu_1(E_i)+\mu_1(E_f)\frac{\sin\alpha}{\sin\beta}}\left[1-e^{-\left(\frac{\mu_1(E_i)}{\sin\alpha}+\frac{\mu_1(E_f)}{\sin\beta}\right)d_1}\right]. \tag{5.1}$$

The intensity coming from buried layers follows a very similar development.[37] An integral over the depth of the buried layer will provide the same general expression as Eq. (5.1). However, the attenuation of the x-rays as they traverse the top layer(s) must be accounted for as the x-rays enter and exit the sample. For the second layer this leads to

an additional exponential attenuation term over the distance d_1 and for the third layer, two additional exponential term over the distances d_1 and d_2. The expressions for I_2 and I_3 can thus be written as

$$\begin{aligned} I_2 = \quad & \eta(E_f)\frac{\Omega}{4\pi}\sum_{X_2} \quad \frac{\omega_{X_2}(E_i,E_f)\mu_{X_2}(E_i)}{\mu_2(E_i)+\mu_2(E_f)\frac{\sin\alpha}{\sin\beta}}\left[1-e^{-\left(\frac{\mu_2(E_i)}{\sin\alpha}+\frac{\mu_2(E_f)}{\sin\beta}\right)d_2}\right] \\ & \times e^{-\left(\frac{\mu_1(E_i)}{\sin\alpha}+\frac{\mu_1(E_f)}{\sin\beta}\right)d_1} \quad (5.2) \\ I_3 = \quad & \eta(E_f)\frac{\Omega}{4\pi}\sum_{X_3} \quad \frac{\omega_{X_3}(E_i,E_f)\mu_{X_3}(E_i)}{\mu_3(E_i)+\mu_3(E_f)\frac{\sin\alpha}{\sin\beta}}\left[1-e^{-\left(\frac{\mu_3(E_i)}{\sin\alpha}+\frac{\mu_3(E_f)}{\sin\beta}\right)d_3}\right] \\ & \times e^{-\left(\frac{\mu_1(E_i)}{\sin\alpha}+\frac{\mu_1(E_f)}{\sin\beta}\right)d_1} e^{-\left(\frac{\mu_2(E_i)}{\sin\alpha}+\frac{\mu_2(E_f)}{\sin\beta}\right)d_2} \quad (5.3) \end{aligned}$$

The total detected intensity will then be $I = I_1 + I_2 + I_3$ if no energy discrimination is possible. With energy discrimination, the question then becomes case specific. If the layers are composed of unique elements with well-separated emission lines, then considerable simplification of the expression will be possible. Moreover, if certain layers can be treated as very thin or very thick relative to their x-ray penetration depths, then the simplification can proceed even further. We will now consider some of these cases.

5.1.1 The two layer problem

The two layer problem is interesting because it covers a few common scenarios in XAS studies. Firstly, it is often the case that a thin film is grown on top of a substrate. The question that is asked is then for what thicknesses of thin film are the previously described IPFY techniques appropriate. Secondly, it may be useful to know whether a thin contamination layer would substantially modify the IPFY spectra and at what thickness such considerations become non-negligible. The general expressions for the intensities of the first and second layers are given by I_1 and I_2 in Eqs. (5.1) and (5.2).

For the case of a thin layer on top of a thick layer, the second layer can be treated as infinitely thick relative to the x-ray penetration depth. The expressions for the FY

intensities of the two layers are thus

$$\begin{aligned} I_1 = &\quad \eta(E_f)\tfrac{\Omega}{4\pi}\sum_{X_1} \quad \frac{\omega_{X_1}(E_i,E_f)\mu_{X_1}(E_i)}{\mu_1(E_i)+\mu_1(E_f)\frac{\sin\alpha}{\sin\beta}}\left[1-e^{-\left(\frac{\mu_1(E_i)}{\sin\alpha}+\frac{\mu_1(E_f)}{\sin\beta}\right)d_1}\right] \\ I_2 = &\quad \eta(E_f)\tfrac{\Omega}{4\pi}\sum_{X_2} \quad \frac{\omega_{X_2}(E_i,E_f)\mu_{X_2}(E_i)}{\mu_2(E_i)+\mu_2(E_f)\frac{\sin\alpha}{\sin\beta}}e^{-\left(\frac{\mu_1(E_i)}{\sin\alpha}+\frac{\mu_1(E_f)}{\sin\beta}\right)d_1}. \end{aligned} \tag{5.4}$$

There are two limits that simplify Eq. (5.4) substantially:

$$\text{Limit 1:} \quad \left(\frac{\mu_1(E_i)}{\sin\alpha}+\frac{\mu_1(E_f)}{\sin\beta}\right)d_1 \ll 1 \tag{5.5}$$

$$\text{Limit 2:} \quad \left(\frac{\mu_1(E_i)}{\sin\alpha}+\frac{\mu_1(E_f)}{\sin\beta}\right)d_1 \gg 1. \tag{5.6}$$

5.1.1.1 Limit 1: thin top layer

This limit specifies that the top layer is thin relative to the x-ray penetration depth. In this case, the contribution from layer 1 becomes negligible and the contribution from layer 2 dominates. We can see this by inspection of the exponential terms in I_1 and I_2. In I_1, the term in square brackets goes to 0, while in I_2 the exponential term goes to 1.

$$\begin{aligned} I_1 &\approx 0 \\ I_2 &\approx \eta(E_f)\frac{\Omega}{4\pi}\sum_{X_2}\frac{\omega_{X_2}(E_i,E_f)\mu_{X_2}(E_i)}{\mu_2(E_i)+\mu_2(E_f)\frac{\sin\alpha}{\sin\beta}}. \end{aligned} \tag{5.7}$$

Hence, if there is only a thin layer of surface contamination, the main contribution to the detected intensity will come from the second layer. I_2 is precisely of the form we began with in chapter 3, so it is clear that we will be able to recover the IPFY expression in this case. This enforces our view that IPFY is a bulk-sensitive measure of XAS, since it is not affected by thin contamination layers at the surface.

Nevertheless, it is important to keep the full condition in mind when planning IPFY experiments. The x-ray penetration length can vary substantially as a function of photon energy and have an impact on whether Limit 1 is valid. Moreover, changes in the experimental geometry can also alter the condition a great deal – for example, measuring at grazing incidence means that the the incident beam will traverse through a longer path in the contamination layer, which is seen as a divergence of the $\mu_1(E_i)/\sin\alpha$ term in our validity condition. These considerations lead us to use the terminology "thick/thin relative to the x-ray penetration length" as the determination of "thick" and "thin" depends on the geometry and the absorption of the material.

5.1.1.2 Limit 2: Thick top layer

This limit represents a top layer which is thick relative to the x-ray penetration length. Note that this can still be a thin film that is thick relative to the x-ray penetration length. In this case the contribution from layer 1 dominates and the contribution from layer 2 is negligible, since the term in brackets in I_1 goes to 1 and the exponential term in I_2 goes to 0.

$$\begin{aligned} I_1 &\approx \eta(E_f)\frac{\Omega}{4\pi}\sum_{X_1}\frac{\omega_{X_1}(E_i,E_f)\mu_{X_1}(E_i)}{\mu_1(E_i)+\mu_1(E_f)\frac{\sin\alpha}{\sin\beta}} \\ I_2 &\approx 0. \end{aligned} \tag{5.8}$$

The expression for I_1 is now of the form compatible with inverse and defining IPFY. This demonstrates that IPFY can be used to study films on top of substrates, so long as Limit 2 is valid at all photon energies and for all experimental geometries of interest. The exact evaluation of this condition is specific to the material and film thickness, but in many cases should enable the study of thin films deposited on substrates. This can be achieved either by growing the film to sufficient thickness or by selecting α and β so that the information depth is confined to the available sample thickness at all photon energies.

5.1.1.3 Top layer of intermediate thickness

Unfortunately, neither of these limits addresses the question of whether IPFY is valid for a top layer of intermediate thickness (ie. neither thin nor thick relative to the x-ray penetration length) on top of a thick buried layer. First, we must ask whether we are interested in studying the top layer or the buried layer.

If we are interested in the buried layer, then we can proceed by making a few assumptions about the materials. Assuming that the top layer does not contain the same elements as the buried layer, nor any absorption edges in the region of interest, the PFY intensity from a level of interest Y_2 in the buried layer is

$$I_2 = \eta(E_f)\frac{\Omega}{4\pi}\frac{\omega_{Y_2}(E_i,E_f)\mu_{Y_2}(E_i)}{\mu_2(E_i)+\mu_2(E_f)\frac{\sin\alpha}{\sin\beta}}e^{-\left(\frac{\mu_1(E_i)}{\sin\alpha}+\frac{\mu_1(E_f)}{\sin\beta}\right)d_1}. \tag{5.9}$$

In this case, since the buried buried layer is thick, Eq. (5.2) simplifies by letting the term in square brackets go to 1 (d_2 is thick relative to the x-ray penetration length) and by dropping the sum over the atomic levels X_2 in layer 2. Note that $I_1 \neq 0$ in this case,

but I_2 can simply be measured separately from I_1 by means of an energy-discriminating detector if the emission lines are well-separated.

Now, if we assume that the variation of $\exp\left[-\left(\frac{\mu_1(E_i)}{\sin\alpha}+\frac{\mu_1(E_f)}{\sin\beta}\right)d_1\right]$ with E_i is small, then we recover a functional form that once again simplifies such that the IPFY can be well-defined. This assumption is reasonable if $\mu_1(E_i)$ does not vary significantly over the energy range of interest, since all other terms are effectively constants. One downside of this scenario is that the absorption by the top layer reduces the overall intensity from the buried layer of interest, so the signal to noise ratio will be worse than for a system with no top layer. Nevertheless, the IPFY signal will still be linearly proportional to $\mu_{\mathrm{tot}}(E)$ over a narrow energy range and a reliable measure of the XAS of the buried layer should be possible given high enough incident flux and adequate detection electronics.

If we are instead interested in the top layer of intermediate thickness and we make the same assumption that the top layer does not contain the same elements as the buried layer nor any absorption edges in the region of interest, then the PFY from a level of interest Y_1 in the top layer is

$$I_1 = \eta(E_f)\tfrac{\Omega}{4\pi}\frac{\omega_{Y_1}(E_i,E_f)\mu_{Y_1}(E_i)}{\mu_1(E_i)+\mu_1(E_f)\frac{\sin\alpha}{\sin\beta}}\left[1-e^{-\left(\frac{\mu_1(E_i)}{\sin\alpha}+\frac{\mu_1(E_f)}{\sin\beta}\right)d_1}\right] \tag{5.10}$$

As before, we note that $I_2 \neq 0$, but we can simply measure I_1 separately from I_2 by means of an energy-discriminating detector. We would like to solve for $\mu_1(E_i)/\mu_1(E_f)$, but there is unfortunately no simple way to do this analytically. The further simplification of this PFY expression depends on the specific material composition and the thickness of the film. Generally, the effect of the term in square brackets will be to reduce the overall PFY intensity in an energy-dependent way.

In the pre- and post-edge regions, the penetration length of x-rays can be considerably higher than it is at an absorption peak in the XANES region. As a result, the reduction in PFY intensity will be higher in the pre- and post-edge than at an absorption peak. The inverse of such a spectrum, the "IPFY", will then appear to have increased background levels relative to an effectively unchanged absorption peak. Moreover, the magnitude of this effect will change with the experimental geometry.

As a result, it can generally be said that studying films of intermediate thickness is not ideal for IPFY. Intermediate thicknesses lead to a scenario where the PFY from the film is complicated, the IPFY cannot be defined in a straightforward manner and thickness-induced distortions are expected to occur. It should be noted that these thickness-induced distortion effects would also be present in resonant PFY and TFY, so this problem is not

exclusive to IPFY. In resonant PFY and TFY, this would result in lower than usual pre- and post-edge levels, and hence artificially enhanced peak magnitudes. In IPFY, we would expect the opposite – artificially enhanced pre- and post-edge levels relative to a reasonable peak intensity. Nevertheless, if the material of interest is a thick layer buried below a film of intermediate thickness, the IPFY from the buried layer is well-defined so long as the energy range is restricted and the top layer does not contain absorption edges in the region of interest.

5.1.1.4 Extending the two layer problem to more layers

As shown in Eqs. (5.2) and (5.3), the addition of more layers means that buried layers gain additional exponential terms related to the thickness and absorption path lengths of the top layers. Hence, with each additional layer, more conditions need to be evaluated if the goal is to isolate a particular emission line from a given layer. The following general guidelines then come from our understanding of the two layer problem:

1. The contribution to the total intensity of any thin layer, where thin refers to the condition that the x-ray path lengths are small relative to the attenuation length of the material, will be negligible so long as grazing incidence and detection are avoided.
2. A thick layer can absorb a large enough fraction of the incident radiation that layers buried below this thick layer do not contribute to the total intensity.
3. If layers of intermediate thickness exist, only the full FY expressions [Eqs. (5.1), (5.2) and (5.3)] are valid. One then has to consider the particulars of the multilayer (ie. the densities of elements in each layer and the precise layer thicknesses) in order to make progress on the problem. Given a restricted set of parameters, it should be possible to make reasonable simplifications by neglecting terms over specific energy ranges or by expanding the exponential terms in series and only keeping the highest order terms.

5.2 Powder specimens

There are often scenarios when bulk single crystals or homogeneous films are not available for XAS studies and powder specimens are studied instead. In practice, the powder specimens may be loosely applied to carbon tape, mechanically pressed or sintered. These

samples, although prepared differently, share common features such as an irregular surface and a degree of bulk porosity. The effect of surface roughness and bulk porosity has not been explicitly worked out for a general x-ray fluorescence yield measurement, to my knowledge. However, there have been efforts to treat the problem in specific scenarios.

Suortti [68] studied the effects of both surface roughness and porosity using a combination of experimental and theoretical models, but limited the analysis to a scenario where $\alpha = \beta$. Hermann and Ermich [69] extended the theoretical aspect into a more powerful language, but still only considered the case where $\alpha = \beta$ for simplicity. Ebel and Poehn [70] treated the problem of surface roughness for a general geometry by means of Monte Carlo simulation to study the effect of varying surface roughness, but did not include porosity effects. Kuhn and Andermann [71] also developed a model for surface roughness alone by approximating the surface as a square wave with surface roughnesses ranging from 10 Å to 10000 Å (ie. the soft and ultra-soft x-ray regimes).

One commonality between all these approaches is that calculating the relative drop in intensity associated with roughness and/or porosity effects requires fixing certain variables. For instance, the incident angle, photon energy, and/or material are often fixed. Without this step, the effective path lengths of the incident and emitted photons cannot be determined and the model cannot be evaluated. Moreover, since roughness and porosity are statistically random phenomena, the results are specific to the chosen model and not necessarily universally true.[1]

The only clear conclusion that can be drawn from a literature review of the subject is that including the effects of surface roughness and porosity into a fluorescence model is a rather complicated problem. The variables are numerous: photon energy, absorption coefficients, surface root mean square roughness, packing fraction, effective path lengths and the measurement geometry. Even the simple square wave surface model of Kuhn and Andermann [71] required at times computing up to one million separate integrals. While I consider this problem generally interesting, it seems to be beyond the scope of the present investigations into the applicability of IPFY for powder specimens.

Instead of trying to develop a model that quantitatively determines the impact of surface roughness and porosity on IPFY of powder specimens, we will attempt to gain a qualitative understanding of these effects by drawing together conclusions from the works mentioned above. With this approach, it should be possible to at least crudely understand the limitations of measuring powder specimens with any of the fluorescence techniques (ie. PFY, IPFY or TFY).

[1] We are excluding from this discussion the possibility of textured materials, where a dominant orientation is present in a powder specimen.

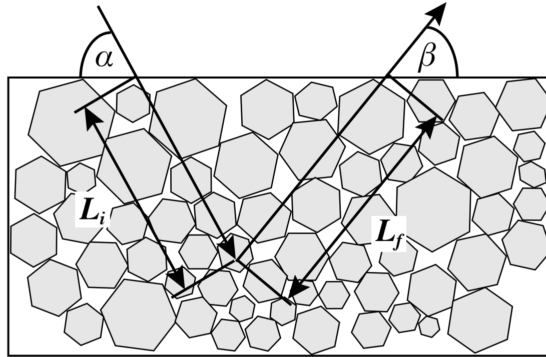

Figure 5.2: The fluorescence geometry for powder specimens. The porosity of the bulk and surface roughness means that the true incident and fluorescence path lengths are smaller than the nominal path lengths L_i and L_f.

Fig. 5.2 illustrates the general problem. Powder particulates are shown as hexagons of varying size and random orientation. The L_i and L_f indicate the nominal paths for a homogeneous sample. Inspection of these paths reveals that the incident and fluorescence path lengths for powder specimens are reduced from the nominal lengths since gaps exist between particulates. Consequently, the path lengths are no longer simple functions of the depth into the sample – they now depend on the particular arrangement of particulates within the powder specimen. A general approach to treating the problem consists of a few steps:

1. Model the effective path lengths and surface roughness according to some distribution of geometrical components. At this stage, the photon energy and experimental geometry is usually fixed so that the path length can be evaluated as a function of depth into the sample. A material must also be selected to determine μ.

2. Within this model, compute the fluorescence yield integral. Depending on the choice of model, this integral can be analytical or numerical and will typically involve averaging over spatial dimensions.

3. Compare the intensity obtained with this model to the result for a bulk, homogeneous sample.

4. Repeat steps 1-3 at different photon energies, for different experimental geometries and for different materials.

This general outline illustrates the complexity of the problem. Many of the parameters are dependent upon one another, necessitating that one fix a few parameters. Even with a sophisticated computer program, mapping out a significant range of the available parameter space would be a challenge. Since to my knowledge this has not been done in a truly systematic manner, it could form the basis of an interesting project for a researcher with an inclination towards geometry, mathematics and programming.

An interesting starting point for such a project would be the approach of Hermann and Ermich.[69] They chose a Boolean model of Poisson polyhedra to estimate the mean path length by determining the average chord length for the particulates. In their model, the mean chord length depends on the volume packing fraction and the mean width of particulates, and is calculated with a correlation function for a random distribution of Poisson polyhedra. Furthermore, they used this geometrical arrangement to model the surface roughness – the mean deviation from the $z = 0$ position depends linearly on the bulk packing fraction and exponentially on the root mean square roughness.

Unfortunately, the problem gets more complicated than this. The path lengths also depend on photon energy and the spatial positioning of the beam. As the photon energy is modified, the path length changes because of the energy-dependent absorption coefficient of the material. If the beam has finite width, the path lengths of parallel photons can differ. The latter consideration can be accounted for by a second integral across the sample surface – averaging out the effect of finite beam width. However, the energy dependence leads to a complication that we can expect to alter the fluorescence spectra in a non-uniform way. We will illustrate this with a hypothetical example of absorption across an absorption edge of a powder specimen.

Keeping the surface roughness, the bulk packing fraction and the experimental geometry fixed, we can qualitatively consider the effects we expect to see in IPFY of powder specimens as a function of photon energy. The photon penetration length is largest in the pre-edge region of a XANES spectrum, since the absorption coefficient is least there. For the present example, we will assume that the penetration length at the pre-edge is significantly larger than the surface roughness and that the mean path length is close to the ideal path length (high packing fraction). In this case, the effect of the surface roughness and porosity is small. This is understood qualitatively because the x-ray penetration length is assumed to be much larger than the roughness and porosity features.[68, 69, 70, 71]

Increasing photon energy to an absorption peak reduces the penetration length by a large amount. Hence, at an absorption peak it is possible for the penetration length of the x-rays to approach the size of the surface roughness and for the effective path length to be considerably smaller than the nominal path length. At the absorption peak, the overall

fluorescence intensity would then be reduced.[68, 69, 70, 71] This is important because it is theoretically possible for roughness and porosity effects to have no influence at energies below the absorption edge yet also have a strong influence at the absorption peak.

In the post-edge, the penetration length is shorter than in the pre-edge, but substantially lower than at the absorption peak. Hence, the reduction of intensity should be somewhere between negligible and strong — a true estimation would depend on choosing a material, an edge, and a roughness/porosity model. This example suggests a few things about IPFY spectra of rough/porous samples:

1. The absorption peak is most sensitive to surface roughness and sample porosity. The combined effect of surface roughness and porosity is an overall reduction in the detected intensity of the FY at the peak. Since this reduction will always be greater at the peak than in the pre- and post-edge, the inverse of a non-resonant PFY (the IPFY) will have an artificially enhanced peak intensity for a sufficiently rough/porous sample.

2. The post-edge will experience a larger reduction in intensity than the pre-edge. In IPFY, this could manifest itself as an enhancement of the post-edge intensity relative to the pre-edge.

Based on these considerations and the advice presented in literature studies of surface roughness and porosity, we can develop some crude criteria for utilizing IPFY on rough/porous specimens in the XANES region:

1. Ensure the material's surface roughness is smaller than the minimal x-ray penetration length of the material. This minimum occurs at the maximum of the x-ray absorption coefficient. A good rule of thumb is that the roughness should be at most 10% of the x-ray penetration length. The surface roughness of a pressed powder can typically be reduced by polishing techniques down to about 0.03 μm.

2. Ensure the powder is pressed to a high packing fraction. This can be accomplished with high pressure mechanical pressing or sintering.

3. Avoid grazing incidence or grazing detection angles, as these amplify the effects of surface roughness.

To study the absorption away from the XANES region, say in wide-energy range measurements to determine sample stoichiometry, the criteria are modified slightly. The minimum penetration length is likely to occur just above an absorption edge, so the 10%

criterion for the surface roughness can be evaluated based on the penetration length estimated in the post-edge. .

It should be noted that these considerations are especially important in the soft x-ray regime. Attenuation lengths for photons in the soft x-ray regime typically range between 0.1 μm to 1 μm in the 400 eV to 2000 eV energy range. Above 2000 eV, attenuation lengths can grow up to hundreds of microns, while below 400 eV they can approach 0.01 μm. Hence, additional work aimed at identifying the impact of surface roughness and porosity in x-ray fluorescence measurements of powder specimens is needed, especially in the soft x-ray regime. Unfortunately, the problem is generally quite complicated. Ideally, a computer program would be written to handle this task. Such a program would hypothetically be capable of handling various geometrical models, simulating the effect of changing α and β, varying the photon energy, and accepting inputs to specify the material's composition.

Chapter 6

Conclusions

X-ray absorption spectroscopy is a powerful tool in investigations of matter in its many forms. The energy dependence of x-ray absorption and emission processes make XAS an element-specific probe of local atomic bonding, coordination, material structure and composition. The advent of synchrotron sources of radiation has propelled the field at an incredible rate over the past few decades. Researchers across many disciplines make use of XAS to study a wide range of materials. The transmission, electron yield and fluorescence yield experimental techniques are the primary ways in which XAS spectra are collected. Unfortunately, transmission suffers from thickness effects, electron yield from saturation and surface effects, and fluorescence yield (in the resonant PFY and TFY modes) is also subject to saturation effects.

The size of these effects can, in some appropriate limits, be small enough that the techniques become viable. For instance, transmission through an ultrathin film can be a very reliable measure of the absorption coefficient, so long as the sample dimensions are known precisely. For thin, conductive samples measured at normal incidence and whose surface is not contaminated, EY can also a good measure of XAS. Additionally, FY in the resonant PFY modes can be a reasonable measure of XAS in the limit of normal incidence and grazing detection or for dilute concentrations of the element of interest.

Unfortunately, these conditions cannot always be met. Ultrathin films are difficult to prepare or simply not available in many cases – ruling out transmission experiments for many materials. Preparing thin films with uncontaminated surfaces for EY requires special care or the availability of a cleavage plane so that the film may be cleaved in vacuum. In the case of thick, insulating samples, EY can exhibit strong charging effects which distort the spectra in a way that is not understood very well. Moreover, saturation effects are

often present in EY spectra and these can severely reduce peak amplitudes when the x-ray penetration length is reduced such that it is comparable to the electron escape depth. For FY in the resonant PFY mode, saturation effects are nearly always present in concentrated samples. These effects depend on experimental geometry and the relative concentrations of elements. They are also generally not easy to account for.

These limitations have made it difficult to apply XAS to insulating materials and the absorption edges of elements in high concentrations. In these cases, a new experimental approach to measuring XAS is needed. Inverse partial fluorescence yield is a newly developed technique that applies in these cases and is generally applicable to a wide range of cases. The theory of IPFY extends directly from the conventional FY theory. Experimentally, this technique requires an energy discriminating photon detector and the existence of a non-resonant emission line that can be used to probe the absorption edge of higher energy core levels present in the material. Here, we summarize the theoretical developments and experimental demonstrations of IPFY presented in this thesis.

6.1 Summary of results

6.1.1 Theoretical results

The theory of IPFY is a simple extension of existing FY theory. The general expression for the IPFY was shown to be given by Eq. (3.5)

$$\mathrm{IPFY} = \frac{I_0(E_i)}{I(E_i, E_f)} = \frac{1}{\eta(E_f)\frac{\Omega}{4\pi}\omega_Y(E_i, E_f)\mu_Y(E_i)}\left(\mu(E_i) + \mu(E_f)\frac{\sin\alpha}{\sin\beta}\right).$$

This expression is the inverse of the PFY arising from a *non-resonant* emission line in a material. Measuring $\mu_{\mathrm{tot}}(E)$ using a non-resonant emission process is a significantly different approach to FY spectroscopy than the resonant PFY and TFY approaches used in the past.

Over a narrow energy range, on can make the approximation that the effect of the energy-dependent pre-factors will be negligible (see section 3.2.1). This can be used to determine the ratio $\mu(E_i)/\mu(E_f)$ as shown in Eq. (4.2).

$$\frac{\mathrm{IPFY}_j}{b} - \frac{\sin\alpha_j}{\sin\beta_j} \approx \frac{a}{b} \approx \frac{\mu(E_i)}{\mu(E_f)}.$$

Over a wider energy range, this approximation is not valid and one must account for the energy dependence of the pre-factors. By making use of the fact that $\frac{\sin\alpha}{\sin\beta}$ is the only variable that changes between experiments with different α and β, we can express $\mu(E_i)/\mu(E_f)$ as shown in Eq. (3.12)

$$\frac{\mu(E_i)}{\mu(E_f)} = \frac{\text{IPFY}}{S_{j,k}(E_i)} - \frac{\sin\alpha}{\sin\beta}.$$

Note that anisotropy effects will typically impact only the XANES and EXAFS regions of absorption spectra, so this approach is valid if we exclude these regions from the analysis when determining $S_{j,k}(E_i)$.

We also showed how it is possible to utilize $\mu(E_i)/\mu(E_f)$ away from the XANES and EXAFS resonances to determine the composition of a sample in section 4.3. We found generally that $\mu(E_i)/\mu(E_f)$ is related to the fractional number densities $R_j = N_{X_j}/N_{X_1}$ of the elements in the material according to Eq. (4.8)

$$\frac{\mu(E_i)}{\mu(E_f)} = \frac{\sum_{j=1}^{n} R_j m_{X_j} \mu^m_{X_j}(E_i)}{\sum_{j=1}^{n} R_j m_{X_j} \mu^m_{X_j}(E_f)}.$$

We also considered the effects of multilayer and powder specimens in chapter 5. Although work in these areas is ongoing, we have considered some limits of the general theory to determine the applicability of IPFY in these cases.

For multilayers, we found that IPFY would apply to thick materials covered either with thin contamination layers or buried below top layers of intermediate thicknesses. The latter required that the top layer not contain any absorption edges in the region of interest and that the region be limited in size. We also found that a type of distortion effect may be present if the layer of interest is of intermediate thickness. The resonant PFY pre- and post-edge regions are expected to have lose more intensity than the high absorption peak regions, so peaks are amplified. IPFY spectra would exhibit the opposite effect – the pre- and post-edge regions would be amplified relative to the peaks and therefore the peaks would appear saturated.

For powder specimens, the key parameters dictating the loss of intensity were found to be surface roughness and bulk porosity. Optimization of these parameters generally reduces the loss of fluorescence intensity, so it was determined that mechanically pressed or sintered powders, polished to the best available surface roughness, should be used when powder specimens are the only option.

6.1.2 Experimental demonstrations

The angle dependent XAS of a polished single crystal of NiO was measured in the XANES region of the Ni L_3 and L_2 absorption edges. This demonstrated the linear relationship between the IPFY intensity and $\frac{\sin\alpha}{\sin\beta}$. The agreement we found was within the limits of the experimental noise. The IPFY also agreed well with TEY measurements from literature on NiO. In contrast, the resonant Ni L PFY was strongly distorted by saturation effects.

We used the approximate IPFY expression (valid over a narrow energy range) to correct the NiO IPFY spectra for the differences in $\frac{\sin\alpha}{\sin\beta}$ and found that the spectra collapsed to a single curve. The magnitude of the edge step compared favourably with tabulated absorption coefficients from calculations and experimental work. Moreover, we estimated the validity of the approximations in this model and found them to be accurate to within 3-5%.

The angle dependent XAS of a single crystal of $NdGaO_3$ was measured over a wide energy range to intentionally invalidate the approximations of the narrow energy range expressions. A sloping background resulting from the energy dependence of $\mu_Y(E_i)$ and $\nu_{\text{Grid}}(E_i)$ was observed. By using the IPFY spectra at different angles, we were able to account for this sloping background and ultimately to correct the spectra such that they were a measure of $\mu(E_i)/\mu(E_f)$. Scaling to $\mu(E_f)$ for $NdGaO_3$, we found that the energy dependence and magnitude of the edge step were in excellent agreement with theoretical calculations for absorption processes that involve final states in the atomic continuum.

We also measured the XANES region of $NdGaO_3$ to compare it directly to TEY and PFY measurements. The PFY was distorted by saturation effects. The TEY, on the other hand, exhibited peculiar negative edge steps and an unusually peaky Nd M_5 absorption peak. This was considered to be a sample charging effect unique to TEY measurements of insulating materials. Ultimately, neither conventional TEY nor resonant PFY techniques were able to correctly measure the XAS of $NdGaO_3$ at its Nd $M_{5,4}$ edges, which has largely Nd^{3+} character. The IPFY measurement, on the other hand, was found to agree very well with a TEY measurement on pure Nd which was shown to be well described by multiplet calculations of Nd^{3+}.

The composition of the $NdGaO_3$ crystal was determined using a fitting approach and the general theory outlined in section 4.3. A purely statistical estimate of the sample composition was found to be $R_2 = 1.07 \pm 0.01$ and $R_3 = 3.03 \pm 0.04$, with nominal values for stoichiometric $NdGaO_3$ of $R_2 = 1$ and $R_3 = 3$. Taking additional sources of error into account, we found that a more realistic estimate was $R_2 = 1.1 \pm 0.2$ and $R_3 = 3.0 \pm 0.5$. These additional sources of error were primarily related to experimental noise which translated into a sensitivity to how one modelled the term $S_{j,k}(E_i)$.

Measurements of IPFY on a single crystal of $La_{1.475}Nd_{0.4}Sr_{0.125}CuO_4$ were also presented. This represents a case where it is possible to obtain a reliable TEY measurement by cleaving of the sample in vacuum. The agreement between the TEY and IPFY in that case was excellent, highlighting the applicability of IPFY to materials which are of genuine scientific interest in a wide range of fields (in this case condensed matter physics).

Finally, a wide energy XRF spectrum for stainless steel 304 was measured between 6.5 keV and 9.0 keV at the CLS's SXRMB beamline. This measurement spanned the Fe K and Ni K absorption edges of SS304. Two non-resonant emission lines were available at the Fe K edge and four non-resonant emission lines were available at the Ni K edge. This was an interesting proof-of-concept, as the IPFY from any available non-resonant emission line should be inversely related to $\mu_{\mathrm{tot}}(E)$. When we compared the IPFY determined from the different emission lines, we found that they were in excellent agreement, which helped to validate the principles governing IPFY spectroscopy. Moreover, this experiment helped to demonstrate that IPFY is not a phenomenon that can only be utilized at soft x-ray energies or at a particular beamline — rather, IPFY has general applicability across a wide range of energies and materials and potentially at all experimental XAS beamlines worldwide.

6.2 Future work

There is still development work to be done on the theoretical and experimental sides to further explore the capabilities and limitations of IPFY spectroscopy.

- Improvements to the detection scheme allowing higher count rates are needed. Such improvements should greatly improve the accuracy of the IPFY analysis. An array of detectors set up at different angles would also greatly reduce the barrier to performing accurate IPFY spectroscopy.
- A proper theoretical treatment of the effects of surface roughness and bulk porosity is needed. As outlined in section 5.2, this problem is generally quite complicated.
- Experiments could be performed with samples prepared to different surface roughnesses to test some of the hypotheses presented in section 5.2 and any theoretical predictions that can be made if progress is made on that front.
- Studies at hard x-ray energies could be used to further validate the principle that IPFY spectroscopy is generally valid for a wide range of materials and absorption edges.

- It should be possible to study XAS in a pure element using the non-resonant L or M emission lines to study K edge absorption in the same element, so long as the transitions are not occurring in or out of the same core states. For example, Mo has a K edge at $\sim$ 20 keV and numerous emission lines between 2 and 3 keV corresponding to transitions between M and N levels to L levels. The L emissions should, in principle, be a probe of the K edge absorption of pure Mo. However, such an experiment may be difficult to perform as it requires a hard x-ray beamline capable of detecting soft x-rays.

- Once noise levels are improved, IPFY experiments could be performed to accurately determine the stoichiometry of samples with different compositions (eg. CuO, Cu_2O, FeO, Fe_2O_3, and Fe_3O_4). Establishing this approach experimentally would be an important demonstration of the principles conveyed in section 4.3.1 and could potentially persuade researchers to record IPFY spectra at multiple angles simultaneously in the future.

APPENDICES

Appendix A

Derivation of α, β and $\frac{\sin\alpha}{\sin\beta}$

Our goal is to derive a general expressions for α, β and $\frac{\sin\alpha}{\sin\beta}$, as these are needed for a proper analysis of IPFY with different experimental geometries.

A.1 Derivation

The rotation matrices about the x, y, and z axes are generally defined as

$$R_x(\theta) = \begin{bmatrix} 1 & 0 & 0 \\ 0 & \cos\theta & -\sin\theta \\ 0 & \sin\theta & \cos\theta \end{bmatrix} \tag{A.1}$$

$$R_y(\theta) = \begin{bmatrix} \cos\theta & 0 & \sin\theta \\ 0 & 1 & 0 \\ -\sin\theta & 0 & \cos\theta \end{bmatrix} \tag{A.2}$$

$$R_z(\theta) = \begin{bmatrix} \cos\theta & -\sin\theta & 0 \\ \sin\theta & \cos\theta & 0 \\ 0 & 0 & 1 \end{bmatrix} \tag{A.3}$$

The experimental geometry is illustrated in Fig. A.1. The origin is defined as the center

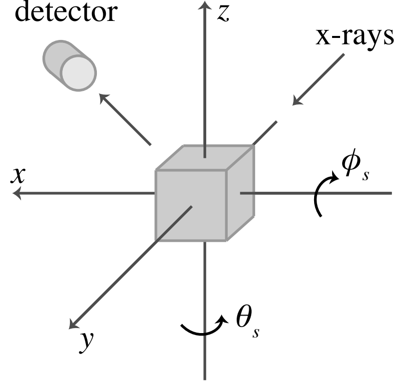

Figure A.1: The experimental geometry used in the derivation of α, β and $\frac{\sin\alpha}{\sin\beta}$.

of the sample. We define a vector $\vec{b}$ from the origin pointing in the beam direction as

$$\begin{aligned} \vec{b} &= -\hat{y} \\ &= \begin{bmatrix} 0 \\ -1 \\ 0 \end{bmatrix}. \end{aligned} \tag{A.4}$$

The norm of the sample with no rotations is also in the beam direction. After applying rotations about the z axis of θ_s and about the x axis of ϕ_s, the norm of the sample is given by

$$\begin{aligned} \vec{n} &= R_z(\theta_s) \cdot R_x(\phi_s) \cdot -\hat{y} \\ &= \begin{bmatrix} \sin(\theta_s)\cos(\phi_s) \\ -\cos(\theta_s)\cos(\phi_s) \\ -\sin(\phi_s) \end{bmatrix}. \end{aligned} \tag{A.5}$$

We also define a vector indicating the detector direction by

$$\begin{aligned} \vec{d} &= R_z(\theta_d) \cdot R_x(\phi_d) \cdot -\hat{y} \\ &= \begin{bmatrix} \sin(\theta_d)\cos(\phi_d) \\ -\cos(\theta_d)\cos(\phi_s) \\ -\sin(\phi_d) \end{bmatrix}. \end{aligned} \tag{A.6}$$

We can now use the dot product relation $\vec{v}_1 \cdot \vec{v}_2 = |\vec{v}_1||\vec{v}_2| \cos\theta_{\vec{v}_1,\vec{v}_2}$ to solve for the angle between two vectors $\vec{v}_1$ and $\vec{v}_2$, $\theta_{\vec{v}_1,\vec{v}_2}$. In order to proceed algebraically, it is useful to define

the allowed ranges of $\alpha, \beta, \theta_s, \phi_s, \theta_d, \phi_d$ to be

$$\begin{aligned}
0 \leq & \quad \alpha & \leq \pi/2 \\
0 \leq & \quad \beta & \leq \pi/2 \\
-\pi/2 \leq & \quad \theta_s & \leq \pi/2 \\
-\pi/2 \leq & \quad \phi_s & \leq \pi/2 \\
-\pi \leq & \quad \theta_d & \leq \pi \\
-\pi/2 \leq & \quad \phi_d & \leq \pi/2.
\end{aligned} \tag{A.7}$$

Under these geometrical constraints, we can solve for α' and β', which define the angles relative to the norm of the sample surface

$$\begin{aligned}
\cos\alpha' &= \frac{\vec{n}\cdot\vec{b}}{|\vec{n}||\vec{b}|} \\
&= \cos(\phi_s)\cos(\theta_s)
\end{aligned} \tag{A.8}$$

$$\begin{aligned}
\cos\beta' &= \frac{\vec{n}\cdot\vec{d}}{|\vec{n}||\vec{d}|} \\
&= \cos(\phi_d)\cos(\phi_s)\cos(\theta_d-\theta_s)+\sin(\phi_d)\sin(\phi_s).
\end{aligned} \tag{A.9}$$

Throughout this thesis, α and β have been defined as measured from the sample surface. Hence $\alpha = \pi/2 - \alpha'$ and $\beta = \pi/2 - \beta'$. Solving for α and β, we obtain

$$\alpha = \sin^{-1}\left(\cos(\phi_s)\cos(\theta_s)\right) \tag{A.10}$$

$$\beta = \sin^{-1}\left(\cos(\phi_d)\cos(\phi_s)\cos(\theta_d-\theta_s)+\sin(\phi_d)\sin(\phi_s)\right). \tag{A.11}$$

Thus, the geometrical factor $\frac{\sin\alpha}{\sin\beta}$ can be calculated generally as

$$\frac{\sin\alpha}{\sin\beta} = \frac{\cos\theta_s}{\cos(\phi_d)\cos(\theta_d-\theta_s)+\sin(\phi_d)\tan(\phi_s)}. \tag{A.12}$$

Experiments are often performed with $\phi_s = 0$, in which case $\frac{\sin\alpha}{\sin\beta}$ is given by

$$\frac{\sin\alpha}{\sin\beta} = \frac{\cos\theta_s}{\cos(\phi_d)\cos(\theta_d-\theta_s)}. \tag{A.13}$$

A.2 Uncertainties

It may be necessary to estimate the uncertainties in α, β or $\frac{\sin\alpha}{\sin\beta}$. Here we develop the expressions for these uncertainties. The uncertainty of a general multivariate function $f(x_1, x_2, ..., x_n)$ with uncorrelated, normally distributed errors is given by [72]

$$\sigma_{f(x_1,x_2,...,x_n)} = \sqrt{\sum_{i=1}^{n}\left(\frac{\partial f}{\partial x_i}\sigma_{x_i}\right)^2}. \tag{A.14}$$

Based on Eq. (A.14), we can calculate σ_α, σ_β and $\sigma_{\frac{\sin\alpha}{\sin\beta}}$ for errors in the experimental angles $\sigma_{\theta_s}, \sigma_{\phi_s}, \sigma_{\theta_d}$ and σ_{ϕ_d}. After some algebraic simplification, we find

$$\sigma_\alpha = \sqrt{\frac{\sigma_{\theta_s}^2\cos^2(\phi_s)\sin^2(\theta_s) + \sigma_{\phi_s}^2\sin^2(\phi_s)\cos^2(\theta_s)}{1-\cos^2(\phi_s)\cos^2(\theta_s)}} \tag{A.15}$$

$$\begin{aligned}\sigma_\beta = \Bigg(&\Big[{\sigma_{\theta_s}}^2\cos^2(\phi_d)\cos^2(\phi_s)\sin^2(\theta_d-\theta_s)\\ &+ {\sigma_{\theta_d}}^2\cos^2(\phi_d)\cos^2(\phi_s)\sin^2(\theta_d-\theta_s)\\ &+ {\sigma_{\phi_d}}^2\big(\cos(\phi_d)\sin(\phi_s)-\sin(\phi_d)\cos(\phi_s)\cos(\theta_d-\theta_s)\big)^2\\ &+ {\sigma_{\phi_s}}^2\big(\sin(\phi_d)\cos(\phi_s)-\cos(\phi_d)\sin(\phi_s)\cos(\theta_d-\theta_s)\big)^2\Big]\\ &\times\Big[1-(\cos(\phi_d)\cos(\phi_s)\cos(\theta_d-\theta_s)+\sin(\phi_d)\sin(\phi_s))^2\Big]^{-1}\Bigg)^{1/2}\end{aligned} \tag{A.16}$$

$$\begin{aligned}\sigma_{\frac{\sin\alpha}{\sin\beta}} = \Bigg(&\Big[\sigma_{\theta_s}^2\big(\sin(\phi_d)\tan(\phi_s)\sin(\theta_s)+\cos(\phi_d)\sin(\theta_d)\big)^2\\ &+ \sigma_{\theta_d}^2\cos(\phi_d)^2\cos(\theta_s)^2\sin(\theta_d-\theta_s)^2\\ &+ \sigma_{\phi_d}^2\cos(\theta_s)^2\big(\sin(\phi_d)\cos(\theta_d-\theta_s)-\cos(\phi_d)\tan(\phi_s)\big)^2\\ &+ \sigma_{\phi_s}^2\sin(\phi_d)^2\sec(\phi_s)^4\cos(\theta_s)^2\Big]\\ &\times\Big[\sin(\phi_d)\tan(\phi_s)+\cos(\phi_d)\cos(\theta_d-\theta_s)\Big]^{-4}\Bigg)^{1/2}.\end{aligned} \tag{A.17}$$

These expressions are only appropriate if the uncertainties in the angles are uncorrelated and random. If systematic errors are expected, then the effect of the systematic error should be simulated by recalculation of α, β and $\frac{\sin\alpha}{\sin\beta}$ with the systematic offset varied.

References

[1] Röntgen, W. K. On a new kind of rays. *Nature*, **53**, pp. 274–276, 1896.

[2] Barkla, C. G. LXXV. Secondary radiation from gases subject to X-rays. *Philosophical Magazine Series 6*, **5**, 30, pp. 685–698, 1903.

[3] Bragg, W. H. and Bragg, W. L. The reflection of X-rays by crystals. *Proc. R. Roc. Lond. A*, **88**, pp. 428–438, 1913.

[4] Moseley, H. G. J. The high-frequency spectra of the elements. *Philosophical Magazine*, **26**, 156, pp. 1024–1034, 1913.

[5] von Laue, M. Concerning the detection of X-ray interferences, 1915. Nobel lecture.

[6] Thompson, A., Attwood, D., Gullikson, E., Howells, M., Kim, K.-J., Kirz, J., Kortright, J., Lindau, I., Liu, Y., Pianetta, P., Robinson, A., Scofield, J., Underwood, J., Williams, G., and Winick, H. X-Ray Data Booklet. Lawrence Berkeley National Laboratory, CA, 2009.

[7] Bohr, N. On the constitution of atoms and molecules. *Philosophical Magazine*, **26**, 155, pp. 857–875, 1913.

[8] Bohr, N. The structure of the atom, 1922. Nobel lecture.

[9] Hüfner, S. *Photoelectron Spectroscopy*, volume 82 of *Springer Series in Solid-State Sciences* (Springer, Berlin, 1995).

[10] Warren, B. E. *X-ray Diffraction* (Addison-Wesley, Reading, MA, 1969).

[11] de Broglie, M. Sur une nouveau procédé permettant d'obtenir la photographie des spectres de raies des rayons Röntgen. *Comptes Rendus*, **157**, pp. 924–926, 1913.

[12] Als-Nielson, J. and McMorrow, D. *Elements of Modern X-Ray Physics* (John Wiley & Sons Ltd., Reading, MA, 2001).

[13] Stöhr, J. and Seigmann, H. *Magnetism: From Fundamentals to Nanoscale Dynamics.* (Springer-Verlag, Berlin-Heidelberg, 2006).

[14] de Groot, F. and Kotani, A. *Core Level Spectroscopy of Solids* (CRC Press, Boca Raton, FL, 2008).

[15] Bearden, J. X-ray wavelengths. *Reviews of Modern Physics*, **39**, 1, pp. 78–124, 1967.

[16] Deslattes, R., Jr, E. K., Indelicato, P., de Billy, L., Lindroth, E., and Anton, J. X-ray transition energies: new approach to a comprehensive evaluation. *Reviews of Modern Physics*, 2003.

[17] Stöhr, J. *NEXAFS Spectroscopy*, volume 25 of *Springer Series in Surface Sciences* (Springer, Berlin, 1996).

[18] Sayers, D. E., Stern, E. A., and Lytle, F. W. New technique for investigating noncrystalline structures: Fourier analysis of the Extended X-Ray—Absorption Fine Structure. *Phys. Rev. Lett.*, **27**, 18, pp. 1204–1207, 1971.

[19] Lee, P., Citrin, P., Eisenberger, P., and Kincaid, B. Extended X-ray absorption fine structure—its strengths and limitations as a structural tool. *Reviews of Modern Physics*, 1981.

[20] Rehr, J. and Albers, R. Theoretical approaches to x-ray absorption fine structure. *Reviews of Modern Physics*, 2000.

[21] Cullity, B. D. *Elements of X-ray Diffraction* (Addison-Wesley, Reading, MA, 1956).

[22] Jaklevic, J., Kirby, J. A., Klein, M. P., Robertson, A. S., Brown, G. S., and Eisenberger, P. Fluorescence detection of EXAFS: Sensitivity enhancement for dilute species and thin films. *Solid State Commun.*, **23**, 9, pp. 679–682, 1977.

[23] Fraser, G. The characterisation of soft X-ray photocathodes in the wavelength band 1-300 : I. Lead glass, lithium fluoride and magnesium fluoride. *Nuclear Instruments and Methods in Physics Research*, **206**, 1-2, pp. 251–263, 1983.

[24] Parratt, L. G., Hempstead, C. F., and Jossem, E. L. Thickness effect in absorption spectra near absorption edges. *Phys. Rev*, **105**, pp. 1228–1232, 1957.

[25] Stern, E. A. and Kim, K. Thickness effect on the extended-x-ray-absorption-fine-structure amplitude. *Physical Review B*, **23**, 8, p. 3781, 1981.

[26] Goulon, J., Goulon-Ginet, C., Cortes, R., and Dubois, J. M. On experimental attenuation factors of the amplitude of the EXAFS oscillations in absorption, reflectivity and luminescence measurements. *Journal de Physique*, **43**, 3, pp. 539–548, 1982.

[27] Fink, R., Jopson, R., Mark, H., and Swift, C. Atomic fluorescence yields. *Reviews of Modern Physics*, 1966.

[28] Bambynek, W., Crasemann, B., Fink, R., and Freund, H. X-ray fluorescence yields, Auger, and Coster-Kronig transition probabilities. *Reviews of Modern Physics*, 1972.

[29] Hubbell, J., Trehan, P., Singh, N., Chand, B., Mehta, D., Garg, M., Garg, R., Singh, S., and Puri, S. A review, bibliography, and tabulation of K, L and higher atomic shell x-ray fluorescence yields. *J. Phys. Chem. Ref. Data*, **23**, 2, pp. 339–364, 1994.

[30] Wiza, J. L. Microchannel plate detectors. *Nuclear Instruments and Methods*, **162**, 1-3, pp. 587–601, 1979.

[31] Tröger, L., Arvanitis, D., Baberschke, K., Michaelis, H., Grimm, U., and Zschech, E. Full correction of the self-absorption in soft-fluorescence extended x-ray-absorption fine structure. *Phys. Rev. B*, **46**, 6, pp. 3283–3289, 1992.

[32] Eisebitt, S., Böske, T., Rubensson, J.-E., and Eberhardt, W. Determination of absorption coefficients for concentrated samples by fluorescence detection. *Phys. Rev. B*, **47**, 21, pp. 14103–14109, 1993.

[33] Wende, H. Recent advances in x-ray absorption spectroscopy. *Rep. Prog. Phys.*, **67**, 12, pp. 2105–2181, 2004.

[34] Stöhr, J., Padmore, H., Anders, S., Stammler, T., and Scheinfein, M. Principles of x-ray magnetic dichroism spectromicroscopy. *Surf. Rev. Lett.*, **5**, 6, pp. 1297–1308, 1998.

[35] Chantler, C. Detailed tabulation of atomic form factors, photoelectric absorption and scattering cross section, and mass attenuation coefficients in the vicinity of absorption edges in the soft x-ray(Z=30-36, Z=60-89, E=0.1 keV-10 keV), addressing convergence issues of earlier work. *J. Phys. Chem. Ref. Data*, **29**, 4, pp. 597–1048, 2000.

[36] Chantler, C. Theoretical form factor, attenuation, and scattering tabulation for Z=1-92 from E=1-10 eV to E=0.4-1.0 MeV. *J. Phys. Chem. Ref. Data*, **24**, 1, pp. 71–643, 1995.

[37] de Boer, D. K. G. Calculation of x-ray fluorescence intensities from bulk and multilayer samples. *X-Ray Spectrometry*, **19**, pp. 145–154, 1990.

[38] Achkar, A. J., Regier, T. Z., Wadati, H., Kim, Y.-J., Zhang, H., and Hawthorn, D. G. Bulk sensitive x-ray absorption spectroscopy free of self-absorption effects. *Phys. Rev. B*, **83**, 8, p. 081106, 2011.

[39] Owens, A., Bayliss, S. C., Fraser, G. W., and Gurman, S. J. On the relationship between total electron photoyield and X-ray absorption coefficient. *Nuclear Instruments and Methods in Physics Research Section A: Accelerators, Spectrometers, Detectors and Associated Equipment*, **385**, 3, pp. 556–558, 1997.

[40] Bundaleski, N., Shaw, B. J., Silva, A. G., Moutinho, A. M. C., and Teodoro, O. M. N. D. Novel approach to the semi-empirical universal theory for secondary electron yield. *Scanning*, pp. 1–4, 2011.

[41] Nakajima, R., Stöhr, J., and Idzerda, Y. U. Electron-yield saturation effects in L-edge x-ray magnetic circular dichroism spectra of Fe, Co, and Ni. *Phys. Rev. B*, **59**, 9, pp. 6421–6429, 1999.

[42] Kotani, A. and Shin, S. Resonant inelastic x-ray scattering spectra for electrons in solids. *Rev. Mod. Phys.*, **73**, 1, pp. 203–246, 2001.

[43] Yeh, J. and Lindau, I. Atomic subshell photoionization cross sections and asymmetry parameters: $1 \leq Z \leq 103$. *At. Data Nucl. Data Tables*, **32**, 1, pp. 1–155, 1985.

[44] Gudat, W. and Kunz, C. Close similarity between photoelectric yield and photoabsorption spectra in the soft-x-ray range. *Phys. Rev. Lett.*, **29**, 3, pp. 169–172, 1972.

[45] Stohr, J. EXAFS and surface-EXAFS studies in the soft x-ray region using electron yield spectroscopy. *Journal of Vacuum Science and Technology*, **16**, 1, pp. 37–41, 1979.

[46] Salaneck, W. R. and Zallen, R. Surface charging effects on valence band spectra in x-ray photoemission: crystalline and amorphous As_2S_3. *Solid State Communications*, **20**, 8, pp. 793–797, 1976.

[47] Gilbert, B., Andres, R., Perfetti, P., Margaritondo, G., Rempfer, G., and Stasio, G. D. Charging phenomena in PEEM imaging and spectroscopy. *Ultramicroscopy*, **83**, 1-2, pp. 129–139, 2000.

[48] Vlachos, D., Craven, A. J., and McComb, D. W. Specimen charging in X-ray absorption spectroscopy: Correction of total electron yield data from stabilized zirconia in the energy range 250-915 eV. *Journal of Synchrotron Radiation*, **12**, 2, pp. 224–233, 2005.

[49] Santo, G. D., Coluzza, C., Flammini, R., Zanoni, R., and Decker, F. Spatial, energy, and time-dependent study of surface charging using spectroscopy and microscopy techniques. *J. Appl. Phys.*, **102**, 11, p. 114505, 2007.

[50] Henke, B., Liesegang, J., and Smith, S. Soft-x-ray-induced secondary-electron emission from semiconductors and insulators: Models and measurements. *Physical Review B*, **19**, 6, pp. 3004–3021, 1979.

[51] http://exshare.lightsource.ca/sgm/Pages/Beamline.aspx.

[52] Abbate, M., de Groot, F. M. F., Fuggle, J. C., Fujimori, A., Tokura, Y., Fujishima, Y., Strebel, O., Domke, M., Kaindl, G., van Elp, J., Thole, B. T., Sawatzky, G. A., Sacchi, M., and Tsuda, N. Soft-x-ray-absorption studies of the location of extra charges induced by substitution in controlled-valence materials. *Phys. Rev. B*, **44**, 11, pp. 5419–5422, 1991.

[53] van der Laan, G., Zaanen, J., Sawatzky, G. A., and Karnatak, R. Comparison of x-ray absorption with x-ray photoemission of nickel dihalides and NiO. *Phys. Rev. B*, **33**, 6, pp. 4253–4263, 1986.

[54] Rao, K. V. and Smakula, A. Dielectric properties of cobalt oxide, nickel oxide, and their mixed crystals. *Journal of Applied Physics*, **36**, 6, pp. 2031–2038, 1965.

[55] Henke, B., Gullikson, E., and Davis, J. X-ray interactions: photoabsorption, scattering, transmission, and reflection at E=50-30000 eV, Z=1-92. *Atomic Data and Nuclear Data Tables*, **54**, 2, pp. 181–342, 1993.

[56] http://www.nist.gov/pml/data/ffast/index.cfm.

[57] http://henke.lbl.gov/optical_constants/.

[58] Achkar, A. J., Regier, T. Z., Monkman, E. J., Shen, K. M., and Hawthorn, D. G. Determination of total x-ray absorption coefficient using non-resonant x-ray emission, 2011. `arXiv:1104.0259 [cond-mat.str-el]`.

[59] Thole, B. T., van der Laan, G., Fuggle, J. C., Sawatzky, G. A., Karnatak, R. C., and Esteva, J.-M. $3d$ x-ray-absorption lines and the $3d^9 4f^{n+1}$ multiplets of the lanthanides. *Phys. Rev. B*, **32**, 8, pp. 5107–5118, 1985.

[60] Podlesnyak, A., Rosenkranz, S., Fauth, F., Marti, W., Furrer, A., Mirmelstein, A., and Scheel, H. Crystal-field and magnetic properties of the distorted perovskite $NdGaO_3$. *J. Phys.: Condens. Matter*, **5**, 48, pp. 8973–8982, 1993.

[61] Lechner, P., Fiorini, C., Longoni, A., Lutz, G., Pahlke, A., Soltau, H., and Struder, L. Silicon drift detectors for high resolution, high count rate X-ray spectroscopy at room temperature. *Advances in X-ray Analysis*, **47**, pp. 53–58, 2004.

[62] Crawford, M. K., Harlow, R. L., Farneth, E. M. M. W. E., Axe, J. D., Chou, H., and Huang, Q. Lattice instabilities and the effect of copper-oxygen-sheet distortions on superconductivity in doped La_2CuO_4. *Phys. Rev. B*, 1991.

[63] Tranquada, J., Sternlieb, B., Axe, J., Nakamura, Y., and Uchida, S. Evidence for stripe correlations of spins and holes in copper oxide superconductors. *Nature*, 1995.

[64] Ichikawa, N., Uchida, S., Tranquada, J., Niemöller, T., Gehring, P., Lee, S., and Schneider, J. Local magnetic order vs superconductivity in a layered cuprate. *Physical review letters*, **85**, 8, pp. 1738–1741, 2000.

[65] Christensen, N., Rønnow, H., Mesot, J., Ewings, R., Momono, N., Oda, M., Ido, M., Enderle, M., Mcmorrow, D., and Boothroyd, A. Nature of the Magnetic Order in the Charge-Ordered Cuprate La1.48Nd0.4Sr0.12CuO4. *Phys. Rev. Lett.*, **98**, 19, p. 197003, 2007.

[66] Vojta, M. Lattice symmetry breaking in cuprate superconductors: stripes, nematics, and superconductivity. *Adv. in Phys.*, **58**, 6, pp. 699–820, 2009.

[67] Chen, C., Tjeng, L., Kwo, J., Kao, H., Rudolf, P., Sette, F., and Fleming, R. Out-of-plane orbital characters of intrinsic and doped holes in $La_{2-x}Sr_xCuO_4$. *Phys. Rev. Lett.*, **68**, 16, pp. 2543–2546, 1992.

[68] Suortti, P. Effects of porosity and surface roughness on the X-ray intensity reflected from a powder specimen. *Journal of Applied Crystallography*, **5**, 5, pp. 325–331, 1972.

[69] Hermann, H. and Ermrich, M. Microabsorption of X-ray intensity in randomly packed powder specimens. *Acta Crystallographica Section A*, **43**, 3, pp. 401–405, 1987.

[70] Ebel, H. and Poehn, C. Quantitative X-ray fluorescence analysis of specimens with rough surfaces: Monte Carlo approach. *X-Ray Spectrometry*, **18**, 3, pp. 101–104, 1989.

[71] Kuhn, W. K. and Andermann, G. Effects of surface roughness on surface analysis via soft and ultrasoft X-ray fluorescence spectroscopy. *Applied Surface Science*, **185**, 1-2, pp. 84–91, 2001.

[72] Taylor, J. R. *An Introduction to Error Analysis: The Study of Uncertainties in Physical Measurements* (University Science Books, Sausalito, CA, 1997), 2nd edition.